LITHIUM NIOBATE RF-MEMS OSCILLATORS FOR IOT, 5G AND BEYOND

BY

ALI ESSAM ALI KOURANI

DISSERTATION

Submitted in partial fulfillment of the requirements
for the degree of Doctoral of Philosophy in Electrical and Computer Engineering
in the Graduate College of the
University of Illinois Urbana-Champaign, 2021

Urbana, Illinois

Doctoral Committee:

Associate Professor Songbin Gong, Chair
Professor Brian T. Cunningham
Professor José E Schutt-Ainé
Assistant Professor Jin Zhou

ABSTRACT

This dissertation focuses on the design and implementation of lithium niobate ($LiNbO_3$) radiofrequency microelectromechanical (RF-MEMS) oscillators for internet-of-things (IoT), 5G and beyond. The dissertation focuses on solving two main problems found nowadays in most of the published works: the narrow tuning range and the low operating frequency (sub 3 GHz) acoustic oscillators currently deliver. The work introduced here enables wideband voltage-controlled MEMS oscillators (VCMOs) needed for emerging applications in IoT. Moreover, it enables multi-GHz (above 8 GHz) RF-MEMS oscillators through harnessing overmode resonances for 5G and beyond. $LiNbO_3$ resonators characterized by high quality factor (Q), high electromechanical coupling (k_t^2), and high figure-of-merit ($FoM_{RES}= Q\ k_t^2$) are crucial for building the envisioned high-performance oscillators. Those oscillators can be enabled with lower power consumption, wider tuning ranges, and a higher frequency of oscillation when compared to other state-of-the-art (SoA) RF-MEMS oscillators.

Tackling the tuning range issue, the first VCMO based on the heterogeneous integration of a high Q $LiNbO_3$ RF-MEMS resonator and complementary metal oxide semiconductor (CMOS) is demonstrated in this dissertation. A $LiNbO_3$ resonator array with a series resonance of 171.1 MHz, a Q of 410, and a k_t^2 of 12.7% is adopted, while the TSMC 65 nm RF LP CMOS technology is used to implement the active circuitry with an active area of $220\times70\ \mu m^2$. Frequency tuning of the VCMO is achieved by programming a binary-weighted digital capacitor bank and a varactor that are both connected in series to the resonator. The measured best phase noise performances of the VCMO are -72 and -153 dBc/Hz at

1 kHz and 10 MHz offsets from 178.23 and 175.83 MHz carriers, respectively. The VCMO consumes a direct current (DC) of 60 μA from a 1.2 V supply while realizing a tuning range of 2.4 MHz (~ 1.4% tuning range). Such VCMOs can be applied to enable ultralow-power, low phase noise, and wideband RF synthesis for emerging applications in IoT. Moreover, the first VCMO based on $LiNbO_3$ lateral overtone bulk acoustic resonator (LOBAR) is demonstrated in this dissertation. The LOBAR excites over 30 resonant modes in the range of 100 to 800 MHz with a frequency spacing of 20 MHz. The VCMO consists of a LOBAR in a closed-loop with two amplification stages and a varactor-embedded tunable LC tank. By the bias voltage applied to the varactor, the tank can be tuned to change the closed-loop gain and phase responses of the oscillator so that the Barkhausen's conditions are satisfied for the targeted resonant mode. The tank is designed to allow the proposed VCMO to lock to any of the ten overtones ranging from 300 to 500 MHz. These ten tones are characterized by average *Q*s of 2100, k_t^2 of 1.5%, FoM_{RES} of 31.5 enabling low phase noise, and low-power oscillators crucial for IoT. Owing to the high *Q*s of the $LiNbO_3$ LOBAR, the measured VCMO shows a close-in phase noise of -100 dBc/Hz at 1 kHz offset from a 300 MHz carrier and a noise floor of -153 dBc/Hz while consuming 9 mW. With further optimization, this VCMO can lead to direct RF synthesis for ultra-low-power transceivers in multi-mode IoT nodes.

Tackling the multi-GHz operation problem, the first *Ku*-band RF-MEMS oscillator utilizing a third antisymmetric overtone (A_3) in a $LiNbO_3$ resonator is presented in the dissertation. Quarter-wave resonators are used to satisfy the Barkhausen's oscillation conditions for the 3rd overtone while suppressing the fundamental and higher-order resonances. The oscillator achieves measured phase noise of -70 and -111 dBc/Hz at 1 kHz and 100 kHz offsets from a 12.9 GHz carrier while consuming 20 mW of dc power. The oscillator achieves a FoM_{OSC} of 200 dB at 100 kHz offset. The achieved oscillation frequency is the highest reported to date for a MEMS oscillator. In addition, this dissertation introduces the first *X*-band RF-MEMS oscillator built using CMOS technology. The oscillator consists of an acoustic resonator in a closed loop with cascaded RF tuned amplifiers (TAs) built on TSMC RF GP 65 nm CMOS. The TAs bandpass response, set by on-chip

inductors, satisfies Barkhausen's oscillation conditions for A_3 only. Two circuit variations are implemented. The first is an 8.6 GHz standalone oscillator with a source-follower buffer for direct 50 Ω-based measurements. The second is an oscillator-divider chain using an on-chip 3-stage divide-by-2 frequency divider for a ~1.1 GHz output. The standalone oscillator achieves measured phase noise of -56, -113, and -135 dBc/Hz at 1 kHz, 100 kHz, and 1 MHz offsets from an 8.6 GHz output while consuming 10.2 mW of dc power. The oscillator also attains a FoM_{OSC} of 201.6 dB at 100 kHz offset, surpassing the SoA electromagnetic (EM) and RF-MEMS based oscillators. The oscillator-divider chain produces a phase noise of -69.4 and -147 dBc/Hz at 1 kHz and 1 MHz offsets from a 1075 MHz output while consuming 12 mW of dc power. Its phase noise performance also surpasses the SoA *L*-band phase locked loops (PLLs). The demonstrated performance shows the strong potential of microwave acoustic oscillators for 5G frequency synthesis and beyond. This work will enable low-power 5G transceivers featuring high speed, high sensitivity, and high selectivity in small form factors.

To My Parents

ACKNOWLEDGMENTS

First, I would like to express my deepest gratitude to my PhD adviser, Prof. Songbin Gong, for giving me the opportunity to join the Illinois Integrated RF Microsystems Group (ILIRM) at UIUC. His constant motivation and inspiration made my research enjoyable. This dissertation could not have been completed without his full support. I am personally grateful for his advice, which has shaped me as a scholar and an engineer.

Second, I would like to express my appreciation to all ILIRM members: Dr. Tomas Manzaneque, Dr. Ruochen Lu, Dr. Yansong Yang, Dr. Michael Breen, Dr. Anming Gao, Ahmed Emad, Steffen Link, Sarah Shim, Liuqing Gao, Arunita Kar, Brandon Arakawa, Ali Lavasani, and Jack Krol. They have helped and supported me emotionally and technically throughout my PhD.

Third, I would like to thank my ECE friends who have made ECE-Illinois feel like home: Sakshi, and Ashwarya. ILL-INI SAKSHI!!

Fourth, I would like to thank the GOATs, the Arab Student Association, and the Egyptian and Arab communities for making my stay in Illinois so much fun. I will miss annoying Jebzy with my vid calls for no reason.

Fifth, no words can describe how much I owe my Sufi teacher and friends of Charleston, IL. Much love to all of you for your continuous support in my spiritual journey.

Last, all the love to my parents who supported me throughout my PhD with their endless prayers. All the love to my beautiful furry Layla.

TABLE OF CONTENTS

CHAPTER 1: INTRODUCTION

This chapter begins with an overview of the radiofrequency microelectromechanical systems (RF-MEMS) market, devices, and applications. The focus then shifts to the study of oscillators based on RF-MEMS resonators. The motivation behind this dissertation is then discussed, and some design specifications for oscillators in general are discussed with an eye towards their different wireless applications. The chapter then gives an overview of acoustic resonators, their specifications enabling high-performance RF-MEMS oscillators, and the state-of-the-art (SoA) RF-MEMS resonators for both single and overtone resonances. We later focus on a class of resonators known as lithium niobate ($LiNbO_3$) MEMS resonators which are the holy grail of all the oscillator designs presented here. Finally, the chapter concludes with an outline of the rest of the dissertation.

1.1 MEMS MARKET OVERVIEW

Diverse products are envisioned to satisfy consumer needs in many different sectors from telecom to automotive, healthcare, and industrial applications. The automotive industry is always searching for more safety measures, hence pressure sensors for tires and accelerometers are in continuous development. The healthcare

industry is always looking for more efficient modes of diagnosis and treatment, and hence implantable tiny devices for drug delivery, to-go medical tests, and other smart devices are under constant improvement. Nowadays, what is envisioned is far from just collecting data from our surroundings, but to efficiently process these data, take decisions and mass communicate them through billions of wirelessly powered devices. MEMS devices can help in achieving this goal, with their ability to sense and actuate different phenomena like temperature, pressure, chemicals, light, movement, etc.

Different varieties of MEMS sensors and their applications can be found in [1]-[3]. A smartphone nowadays includes essential MEMS devices like gyroscopes, accelerometers, pressure and humidity sensors, and compasses. From the pool of applications, this dissertation focuses on RF-MEMS devices and systems that serve the telecom industry. RF-MEMS devices can be divided to RF filters, resonators, varactors, and switches. Of particular interest are cellular applications such as 5G, and other low-power wirelessly powered applications like Internet-of-Things (IoT). A forecast for the MEMS industry till 2023 predicts a compounded annual growth rate (CAGR) of 21% in the RF-MEMS sector, surpassing the growth expectations for other MEMS sectors [1]. This is mainly due to the increase in demand for RF-MEMS as a solution to many existing issues in the telecommunications industry. RF-MEMS (filters, duplexers, switches, varactors) and oscillators (based on RF-MEMS resonators) are both boosting the MEMS market in CAGR and value.

1.2 MOTIVATION AND PROBLEM STATEMENT

RF synthesizers are the heartbeat of any wireless transceiver. Generating frequency-stable wideband RF carriers consumes a significant portion of the power budget for battery-powered devices [4]. Therefore, miniature, low-power, low phase noise, and wide tuning range RF synthesizers are becoming highly desirable for battery-powered transceivers.

To synthesize spectrally pure RF signals, one can adopt either indirect synthesis based on phase-locked loops (PLLs) [5], [6] or directly constructing signals digitally for the follow-on digital to analog conversion (DAC) [7], [8]. PLLs based on off-chip quartz oscillators (XOs) are the SoA for producing RF carriers with superior close-in phase noise. However, their large footprint, low frequency of operation, and limited frequency tunability hinder their adoption for IoT [9], [10]. On the other hand, direct digital synthesizers provide fast settling time, fine frequency resolution, and small area. Yet their high noise floor, large power consumption, and spurious nature are challenging for any battery powered IoT transceiver.

One practical method to reduce the size and power consumption of voltage-controlled oscillators (VCOs), while boosting the spectral purity of the synthesized signal, is to replace the conventional *LC* tanks with high quality factor (*Q)* MEMS or acoustic resonators that can be closely integrated with ICs, unfortunately forgoing the great tuning range that comes with silicon *LC* tanks (~ 20%). To this end, Chapter 2 focuses on building microwatts sub-GHz voltage-controlled MEMS oscillators (VCMOs) with wide tuning ranges. The chapter reports on the design of

a VCMO based on a $LiNbO_3$ RF-MEMS resonator that is integrated with a 65 nm CMOS chip [11]. The chapter serves to understand the limitations of the core block to build the more exotic systems discussed in Chapter 3.

As an alternative approach to both PLLs and digital methods of synthesizing carriers, direct RF synthesis based on piezoelectric acoustic/MEMS is emerging for multi-mode IoT systems due to its potential to deliver low-power, low phase noise, and ultrawide tuning range. Hence, Chapter 3 focuses on building a direct RF synthesizer based on wideband multi resonances VCMO. This wideband VCMO relies on a single acoustic resonator, hence enabling a free XO, and a free PLL synthesizer for IoT. The chapter reports on the design of a $LiNbO_3$ overtone VCMO exploiting multiple overtones in a single resonator, suited for multi-mode IoT nodes [12].

The above-mentioned projects focus on enabling wideband MEMS oscillators for sub-GHz frequencies and understanding where $LiNbO_3$ VCMOs fit within the SoA technologies. Currently, the sub-3 GHz frequency bands are too congested to meet the ever-increasing data rates and communication speeds demanded by many cellular users. The call for higher bandwidths and speeds has pushed the 5G radios toward mm-wave frequencies such as 26/28 GHz and 37-43.5 GHz. Apart from larger bandwidth, 5G wireless transceivers are expected to feature higher sensitivity and selectivity while producing longer battery life, all in small form factors. To achieve all the above seamlessly, the heartbeat of the transceiver—namely the frequency synthesizer—must be revolutionized on architecture, circuit, and device levels. Local oscillator (LO) noise directly adds to the transceiver noise

figure (NF) and worsens the sensitivity while any spurs on LO considerably exacerbate the selectivity. To relax the requirements on the sensitivity and selectivity of the RF front-end for 5G, the synthesizer phase noise has to be reduced via a non-conventional way. One key challenge in implementing high-performance chip-scale synthesizers for 5G beyond 6 GHz lies in the lack of high-performance miniature resonators that can enable signal generation with minimal phase noise and power consumption.

To this end, the second part of the dissertation focuses on implementing multi-GHz $LiNbO_3$ oscillators with frequencies of oscillation above 8 GHz. This can be achieved through harnessing overmode resonances in the $LiNbO_3$ thin-film, hence enabling high-performance RF synthesizers for 5G and beyond. Chapter 4 proposes the first *Ku*-band RF-MEMS oscillator [13], while Chapter 5 proposes the first *L*/*X* dual-band RF-MEMS synthesizer on a CMOS platform [14]. Both the *X* and *Ku* band oscillators excite the third antisymmetric overtone (A_3) in a $LiNbO_3$ resonator while suppressing the fundamental resonance. The reported performance shows the strong potential of acoustic microwave oscillators to revolutionize the 5G frequency synthesis. Their main strength lies in offering small form factor and long battery life solutions with competitive phase noise results compared to other EM oscillators.

The phenomenal performance of these oscillators owes to the groundbreaking figure-of-merit (FOM_{RES}) of the $LiNbO_3$ resonators, as will be discussed throughout the dissertation.

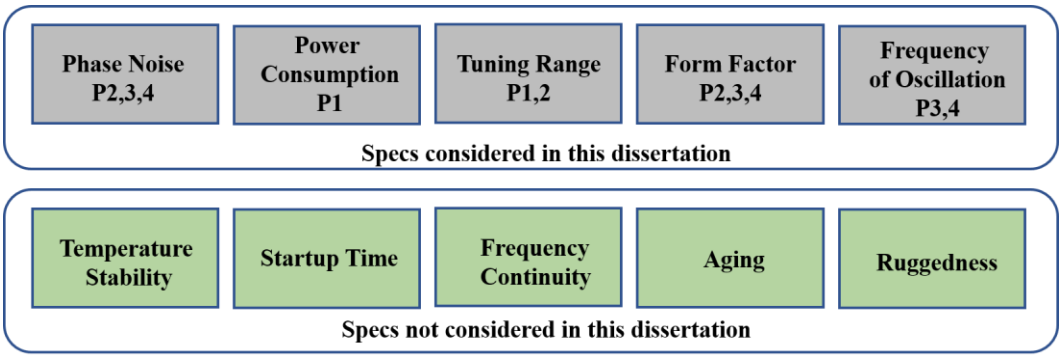

Fig. 1.1. Main VCMO specifications, P stands for project.

1.3 SPECIFICATIONS

1.3.1 VCMO Specifications

The main VCMO specifications for wireless communications [15] are shown in Fig. 1.1 and are described below. Power consumption, frequency of oscillation, tuning range, and phase noise are the main targeted specs in this dissertation. As shown in the figure, different projects included in different chapters target different specifications.

The first project (P1), described in Chapter 2, focuses mainly on power consumption, and on tuning range needed for ultralow-power IoT nodes. The second project (P2), described in Chapter 3, focuses on tuning range, form factor, and phase noise to enable free XO and free PLL synthesizers. The third and the fourth projects (P3,4), described in Chapters 4 and 5, focus on pushing the frequency of oscillation and exploring acoustic oscillators above 8 GHz.

1.3.1.1 Non-deterministic Frequency Stability: Phase Noise

Ideally, the frequency spectrum of a single resonance oscillator should contain just a single impulse frequency. In reality, the frequency of any oscillator shows short-term frequency fluctuation and hence a broadening of the frequency

spectrum, which is called phase noise. Phase noise is the ratio of the power in 1 Hz bandwidth, a frequency f_m away from the carrier, to the power in the carrier itself.

Phase noise negatively affects wireless communications. The close-to-carrier noise adds directly to the system noise figure by adding noise inside the system bandwidth, while the far-from-carrier noise weakens the ability of a receiver to attenuate undesired adjacent channel signals. Both should be reduced in a good oscillator design. The ratio of single-sideband phase noise density to carrier power can be modeled by the first-order linear time-invariant (LTI) classical model shown below [16]-[18].

$$L(f_m) = 10\log_{10}\left[\frac{KTF}{2P_o}\left(1+\frac{f_c}{f_m}\right)\left(1+\frac{1}{f_m^2}\left(\frac{f_o}{2Q_L}\right)^2\right)\right] \tag{1.1}$$

where K is Boltzmann's constant, T is the temperature, F is the oscillator noise factor, P_o is the oscillation power, f_c is the flicker noise corner frequency, f_m is the offset frequency, f_o is the oscillation frequency, and Q_l is the loaded quality factor of the resonator. Here, f_o is assumed to be equal to the resonant frequency f_s for a high Q resonance.

Fig. 1.2 shows the four major causes of noise: the up-converted $1/f$ noise (flicker FM noise with f_m^{-3} slope), the thermal FM noise (with f_m^{-2} slope), the flicker phase noise (with f_m^{-1} slope), and the thermal noise floor with constant power spectral density (PSD). For high Q oscillators such as RF-MEMS oscillators, $f_o/2Q$ is usually a lower frequency than f_c for most of the transistor technologies and MHz

carrier frequencies, resulting in masking the f_m^{-2} region in the phase noise profile [17].

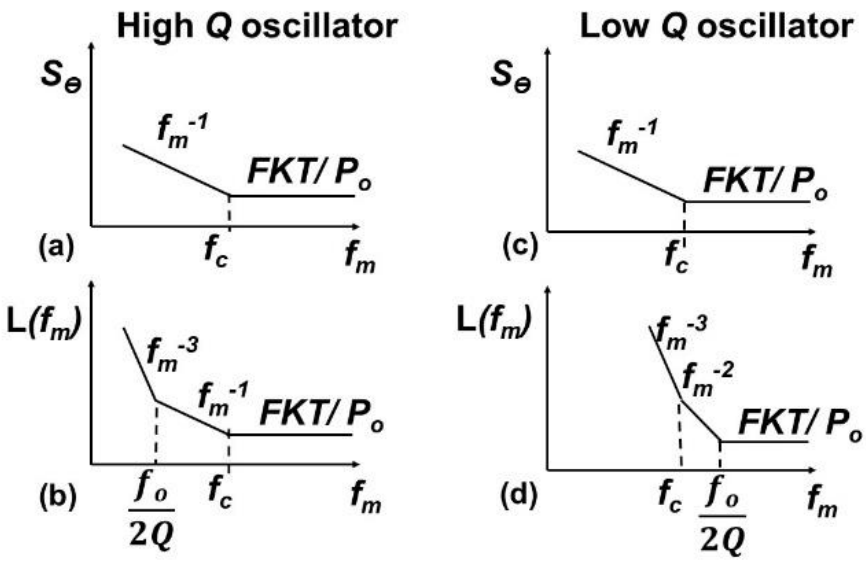

Fig. 1.2. Phase perturbation (S_Θ) and phase noise $L(f_m)$ profiles for high Q and low Q oscillators [11].

Each region of the phase noise curve brings different design challenges. For the noise floor, we want to dissipate as much power as possible in the resonator as long as it operates in the linear regime (larger P_o leads to lower far-out phase noise in contrast). Pumping more current in the resonator usually means higher dc power consumption of the oscillator. The oscillator core must be designed to remain in low-noise operation (low noise factor F) for the design point of the resonator. In the close-to-carrier region, the main factor in determining the phase noise of the oscillator is the loaded Q of the resonator Q_L. The phase noise in this region is mainly due to the up conversion of $1/f$ flicker noise of the amplifier. The oscillator core bias point, the bias circuit design, and the transistor flicker noise are all

significant contributors to the oscillator noise. Finally, the phase noise in the intermediate region is ruled by the up conversion of the thermal noise.

1.3.1.2 Power Dissipation

The application sets restrictions on power consumption. For example, IoT prefers an ultralow-power node with very long battery life. However, a certain amount of power consumption is required to generate enough gain inside the VCMO loop to sustain oscillations. Moreover, the signal power should be large enough to have a large SNR and hence low phase noise, leading to the well-known tradeoff between phase noise and power consumption.

1.3.1.3 Tuning Range

Tuning range is a very important metric for any frequency synthesizer. For many cellular standards, a range of continuous or discrete frequencies needs to be generated, rather than just a single carrier. Such tuning range supports multiple bands or multiple standards and different user channels.

1.3.1.4 Frequency Continuity: Spurious Modes

Intrinsic eigenmodes and mechanical stresses result in multiple spurious modes that approach and, in many cases, cross the fundamental frequency resulting in dropped packets, loss of GPS lock, and cellular signal errors.

1.3.1.5 Long-Term Frequency Stability

In the increasingly popular field of wireless communications, the available frequency spectrum is becoming very limited. Regulatory agencies have imposed

tight restrictions on bandwidth and frequency stability. These requirements vary throughout the spectrum following the intended applications. Factors affecting the frequency stability of an oscillator include variations in voltage, time, and temperature. Specifications for frequency stability are expressed as the amount of the divergence from the nominal operating frequency, usually in terms of a percentage or in parts per million (ppm). This spec will not be addressed in the dissertation. Other metrics may include startup time, aging, cost, and ruggedness.

1.3.1.6 Figure-of-Merit of an Oscillator

Two FoMs are defined for a fair comparison to the literature:

$$FoM_{OSC} = -L(\Delta f) + 20\,log\left(\frac{f_o}{f_m}\right) - 10\,log\left(\frac{P_{DC}}{1\,mW}\right) \tag{1.2}$$

$$FoM^T = FoM + 20\,log\left(\frac{FTR}{10}\right) \tag{1.3}$$

where FoM_{OSC} is the oscillator figure of merit, FoM^T is the tuning range-based figure of merit, P_{dc} is the oscillator dc power consumption, $L(\Delta f)$ is the phase noise measured at an offset f_m from a carrier f_o, and FTR is the fractional tuning range.

1.3.2 RF-MEMS Resonator Specifications

Fig. 1.3 shows the main VCMO targeted specifications (in blue) and the resonator specifications (in orange) needed to achieve the oscillator requirements. High Q is an important metric to achieve superior close-in phase noise and lower power consumption, while the electromechanical coupling (k_t^2, the ratio of the stored mechanical energy to the stored electrical energy in a resonator) is an important specification for wideband VCMOs. Multiplication of both metrics gives

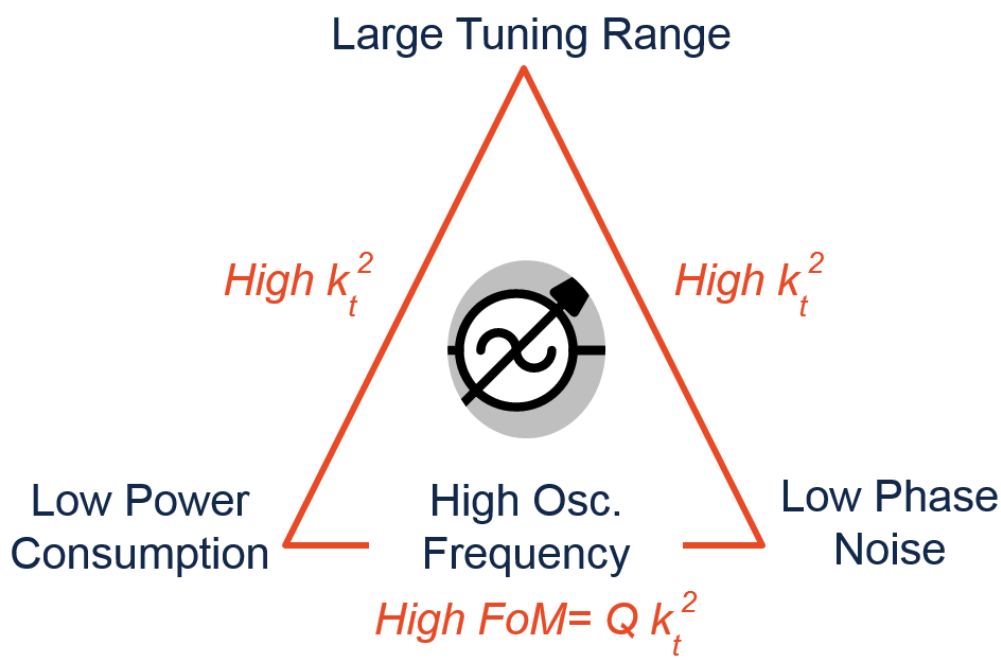

Fig. 1.3. RF-MEMS resonator requirements.

the FoM_{RES} ($Q\ k_t^2$). High FoM_{RES} is crucial for superior close-in and far-out phase noise, lower power consumption, and wide tuning ranges. Also, high FoM_{RES} is a key enabler for direct RF synthesis, as will be discussed in Chapter 3, and for enabling microwave/mm-wave oscillations, as will be shown in Chapters 4 and 5. Detailed analysis of these metrics and how to extract them from the performance of a resonator is given below. In summary, high FoM resonators enable the following topics addressed in this dissertation:

1. Microwatts sub-GHz VCMOs with wide tuning ranges
2. Direct RF synthesis based on wideband multi resonances VCMOs
3. *L/X* and *Ku*-bands low phase noise frequency synthesis

To represent the RF-MEMS or the acoustic resonator in VCMO circuitry and model its performance for a set of specifications, the acoustic device is modeled

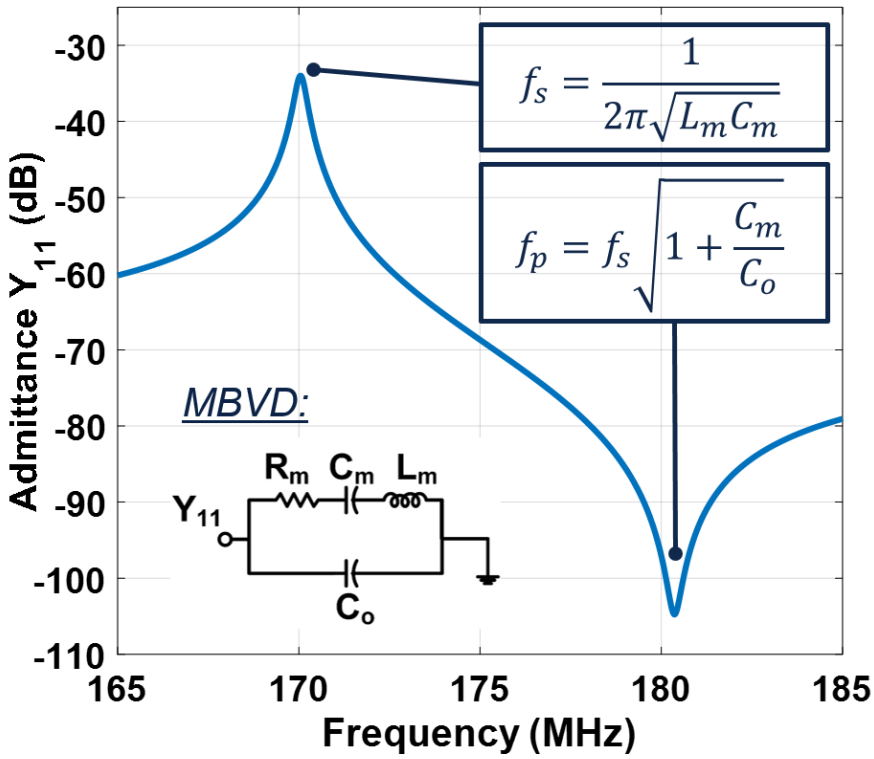

Fig. 1.4. Frequency response of an acoustic resonator with resonance around 170 MHz. MBVD model is shown in the inset.

using the modified Butterworth–Van Dyke (MBVD) model shown in Fig. 1.4, which is well known as the equivalent circuit for acoustic resonators in the electrical domain. The MBVD model consists of a motional arm and a static arm. The motional arm consists of a motional resistance (R_m), motional inductance (L_m), and motional capacitance (C_m). R_m represents the energy dissipation in a resonator while L_m and C_m represent the interchangeable mechanical energy storage in a resonator. These equivalent parameters can be expressed as [19]:

$$R_m = \frac{1}{10^{\frac{Y_{11}(f_s)}{20}}} = \frac{\pi^2}{8}\frac{1}{2\pi f_s C_o}\frac{1}{Qk_t^2} \tag{1.4}$$

$$L_m = \frac{\pi^2}{8}\frac{1}{(2\pi f_s)^2 C_o}\frac{1}{k_t^2} \tag{1.5}$$

$$C_m = \frac{8}{\pi^2} C_o k_t^2 \tag{1.6}$$

These three parameters in series form the motional arm with a motional impedance Z_m given as:

$$Z_m = R_m + j\omega L_m + \frac{1}{j\omega C_m} \tag{1.7}$$

which can also be expressed as a function of frequency pulling $p=(\omega-\omega_s)/\omega_s$ acted on the resonator by the circuit.

$$Z_m \approx R_m + j\frac{2p}{\omega C_m} \tag{1.8}$$

where p is the relative amount of frequency pulling that is above the series resonant angular frequency ω_s of the resonator [20]. The magnitude of the second term of (1.8) is called the effective inductive reactance (ωL_e). Solving for the resonance, where Z_m is real, the series resonance frequency f_s can be calculated as:

$$f_s = \frac{1}{2\pi\sqrt{L_m C_m}} \tag{1.9}$$

and the Q at f_s is defined as:

$$Q = \frac{1}{R_m}\sqrt{\frac{L_m}{C_m}} = \frac{\omega_m L_m}{R_m} \tag{1.10}$$

The electrical energy storage in a resonator is in the static capacitance (C_o) between the IDEs. Hence, the anti-resonance frequency f_p can be defined as:

$$f_p = f_s \sqrt{1 + \frac{C_m}{C_o}} \tag{1.11}$$

From (1.9) and (1.11), k_t^2 can be extracted as:

$$k_t^2 \approx \frac{\pi^2}{4}\left(\frac{f_p - f_s}{f_p}\right) \tag{1.12}$$

These equations are part of the quantitative basis for our earlier emphasis that high k_t^2, high Q, and high FoM are essential for achieving high tuning range, low phase noise, and low power consumption—all concurrently. The correlation between tuning range and k_t^2 will be explained in Chapter 2. Because a smaller R_m leads a smaller impedance at series resonance, less gain is required for loss compensation in the oscillator, leading to a lower noise floor. Hence, a resonator should be designed with a large $\mathrm{FoM_{RES}}$ and sufficient C_o at the design frequency. The latter requirement on C_o, along with achieving a spurious-free response over the targeted tuning range, will be also discussed in Chapter 2.

The FoM of a resonator is collectively determined by the piezoelectric and acoustic properties of the comprising materials, device design, and fabrication process. The material properties set the ultimate limits on the maximum k_t^2 and Q that can be achieved, while an optimized design and fabrication process allows the measured response to approach the limits as closely as possible.

1.4 STATE-OF-THE-ART MEMS RESONATORS/OSCILLATORS

1.4.1 Single Resonances

RF-MEMS resonators based on either electrostatic or piezoelectric transduction have been investigated in the last decade for the purpose of enabling high-performance oscillators. For instance, oscillators based on capacitive resonators have been reported with very high Q values (>40,000), which are the key for attaining a good close-in phase noise performance [21]-[25]. However, they exhibit a large motional resistance R_m in the range of several kΩ due to their limited k_t^2. This limited coupling negatively affects the phase noise floor and significantly reduces the oscillator maximum tuning range. Although recent work has shown a motional resistance R_m less than 1 kΩ [24] by enhancing k_t^2, high dc polarization voltages, vacuum operation, and ultra-small gap spacing between the electrodes are required, particularly for the very high frequency (VHF) and ultra-high frequency (UHF) ranges. More importantly, R_m close to kΩ in these works is still large for interfacing with the low-power RF circuitry. Only recently have researchers succeeded at reducing the R_m of capacitive resonators to 54 Ω at 60 MHz [25] via a complicated fabrication process. Nonetheless, the coupling factor reported is only 1.62%, which is not best suited to implement VCMOs with large frequency tuning ranges.

As an alternative, resonators based on piezoelectric transduction such as thin-film bulk acoustic wave resonators (FBARs) [26]-[33] and surface acoustic wave resonators (SAWs) [34], [35] have been studied for enabling wideband VCMOs [30]-[31]. SAW resonators are characterized by their high k_t^2 of 10%.

Nonetheless, they have moderate Q and limited scalability to higher frequencies (over 2 GHz) because of the energy leakage to the substrate and the comparatively low acoustic velocity, respectively. On the other hand, FBARs, which typically feature a k_t^2 of 6.5%, have been successfully employed to enable low phase noise VCMOs with wider tuning ranges. However, their thickness-mode vibrations make it challenging to integrate multi-frequency resonators on the same substrate. Consequently, it is difficult to attain an even wider tuning range via switching in different resonators [36].

To overcome the lack of on-wafer frequency diversity while attaining low R_m and high tuning range, the resonant MEMS research community has been focusing on developing devices with lithographically definable resonant frequencies via exploiting several high k_t^2 acoustic modes that are also sensitive to the lateral dimensions of the resonator. Different piezoelectric materials, including aluminum nitride (AlN) [36]-[38], AlN-on-Si [39]-[42], AlN-on-silica [43], gallium nitride [44], [45], lead zirconate titanate (PZT) [46], and zinc oxide-on-silicon (ZnO-on-Si) [47], have been investigated for a category of devices dubbed as contour mode resonators (CMRs) or laterally vibrating resonators (LVRs).

Among these materials, PZT features the highest k_t^2. However, the moderate Q and high loss tangent of PZT LVRs are nonideal for implementing low phase noise oscillators [48]. Alternatively, reactively sputtered AlN has been successfully used to build high Q CMRs. VCMOs based on AlN CMRs have been reported with power consumption of 47 μW [37] and 6.9 mW [38]. However, their small electromechanical coupling ($k_t^2 < 2\%$) limits their tuning ranges to 611 ppm and

1500 ppm at center frequencies of 204 and 1500 MHz, respectively. Fig. 1.5 summarizes the main SoA acoustic resonator technologies with their pros and cons.

Capacitive (Si)	Piezoelectric (AlN, ZnO, ScAlN, $LiNbO_3$)	
	AlN CMRs	AlN FBARs
✓ VERY high Qs at low freq.	✓ High Qs	✓ High Qs
✓ CMOS integration	✓ Monolithic multi-frequency	× Lack on-wafer freq. diversity
× Narrow-band (k_t^2 <0.1%)	× Narrow-band (k_t^2 < 2%)	✓ Moderate-band (k_t^2 ~6.5%)
× R_m in kΩ	✓ R_m ~ 100s Ω	✓ R_m ~ 50 Ω
× Typical -130 dBc/Hz floor	✓ Typical > -150 dBc/Hz floor	✓ Typical > -150 dBc/Hz floor
× Large dc voltages	✓ No dc voltages	✓ No dc voltages
× Vacuum package	✓ No vacuum package	✓ No vacuum package
× Very non linear	× Non linear > 0dBm	✓ Highly linear
× Resonance <1 GHz	✓ Fundamental Res. < 10 GHz	✓ Fundamental Res. < 10 GHz

Fig. 1.5. State-of-the-art RF-MEMS resonators.

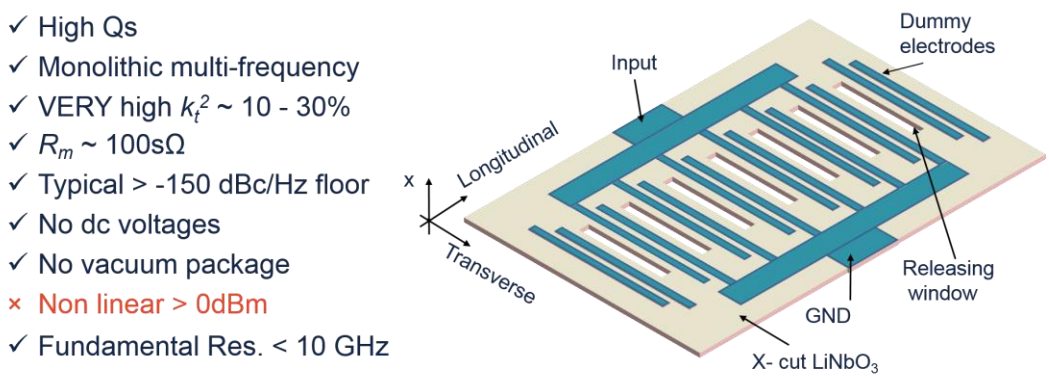

Fig. 1.6. Lithium niobate contour mode resonator.

To further advance LVRs with the simultaneously higher k_t^2 and Q desired by the next-generation radio frequency synthesizers and filters, $LiNbO_3$ LVRs were recently studied and have shown great potential for enabling low phase noise wideband VCMOs due to their unique capability to attain simultaneously high Q (>1000) and high k_t^2 (>20%) [49]-[60]. Their high Q can ensure low phase noise performance while their large k_t^2 permits wideband VCMOs. However, there has been no study on implementing high-performance VCMOs to harness the high FoM

of $LiNbO_3$ LVRs. Fig. 1.6 lists the several advantages of $LiNbO_3$ in enabling high-performance oscillators when compared to the other technologies shown in Fig. 1.5.

1.4.2 Multi Resonances

Unfortunately, LVRs to date are typically designed to produce a single resonance, thus limiting the tuning range of an oscillator to about 1.4% [60]. Although switching between many LVRs within an oscillator can extend the range [61]-[64], such an approach is prone to fabrication yield issues and higher costs. On the other hand, using a single resonator with multi resonances can help to reduce parallelism without sacrificing performance. For this reason, researchers have explored dual-mode MEMS resonators [65], [66] and, more recently, lateral overtone bulk acoustic resonators (LOBARs) leveraging the equally spaced harmonics in the $LiNbO_3$ thin-film cavity. In contrast to its predecessors—namely, high overtone bulk acoustic resonators (HBARs) [67]-[71] and LOBARs based on AlN [72]-[75]—$LiNbO_3$ LOBARs [76]-[78] have shown much higher FoMs for multiple equally-spaced resonances, surpassing the SoA. Hence, overmoding a $LiNbO_3$ LVR can give rise to a more advanced direct RF synthesis.

1.5 LITHIUM NIOBATE RF-MEMS RESONATORS

$LiNbO_3$ is a piezoelectric material that only recently became available in a thin-film form with single-crystal quality owing to crystal ion slicing technology [79], [80]. The access to $LiNbO_3$ thin films has created new possibilities for building high Q chip-scale acoustic resonators and filters needed in RF wireless transceivers. Apart from its piezoelectricity, $LiNbO_3$ is an anisotropic material that

supports the propagation of several acoustic modes with varying degrees of electromechanical coupling in the X, Y, and Z cut planes. Among these cuts, X-cut is normally chosen for building LVRs as it allows the propagation of the lateral S0 [49], [50], [55] and SH0 [51], [53] modes at RF with a large k_t^2. Apart from X-cut $LiNbO_3$, Z-cut $LiNbO_3$ has also attracted major interest as it offers large k_t^2 for A_1 modes at super-high frequencies (SHF) and promising *Qs* [56], [81]. Fig. 1.7 shows the different acoustic mode shapes discussed. $LiNbO_3$ resonators used in P1 and P2, described in Chapters 2 and 3 respectively, excite shear horizontal modes. Antisymmetric modes are excited in the resonators that are used in P3 and P4, described in Chapters 4 and 5, for multi-GHz operation.

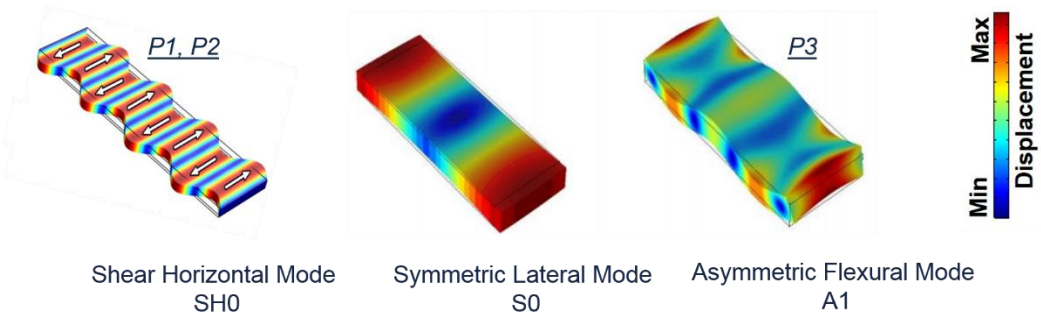

Fig. 1.7. Different acoustic modes. Courtesy of *Ruochen Lu*.

1.6 DISSERTATION ORGANIZATION

The dissertation is organized as follows: Chapter 2 discusses building a tunable low-power oscillator based on high *Q* $LiNbO_3$ RF MEMS resonators and 65 nm CMOS. Chapter 3 focuses on building a wideband oscillator exploiting multiple resonances in overtone $LiNbO_3$ RF-MEMS resonator. Chapter 4 focuses on building a *Ku*-band pierce oscillator utilizing the third antisymteric overtone in

a $LiNbO_3$ RF MEMS resonator. Chapter 5 discuses building a dual *L/X*-band RF-MEMS oscillator using 65 nm CMOS. Finally, Chapter 6 summarizes the work done and proposes some future work and directions for the dissertation.

PART I: WIDEBAND RF-MEMS OSCILLATORS

CHAPTER 2: A TUNABLE LOW-POWER OSCILLATOR BASED ON HIGH *Q* LITHIUM NIOBATE MEMS RESONATORS AND 65 nm CMOS

2.1 INTRODUCTION

This chapter focuses on our first project, microwatts sub-GHz VCMOs with wide tuning ranges. It reports on the design of a VCMO based on a $LiNbO_3$ resonator that is integrated with a 65 nm CMOS chip. The chapter presents a comprehensive guide to co-design piezoelectric RF-MEMS resonators and CMOS for enabling VCMOs that harness the best benefits out of both platforms. The analysis, focusing on understanding the different tradeoffs between tuning range, power consumption, gain and phase noise, is generic to any kind of piezoelectric resonator and specific for Colpitts VCMOs. As a result of this study, a VCMO based on the heterogeneous integration of a high *Q* $LiNbO_3$ resonator and CMOS has been demonstrated. A $LiNbO_3$ resonator array with a series resonance of 171.1 MHz, a *Q* of 410, and an electromechanically coupling factor of 12.7% is adopted, while the TSMC 65 nm RF LP CMOS technology is used to implement the feedback and tuning circuitry with an active area of $220\times70\ \mu m^2$. The frequency tuning of the VCMO is achieved by programming a binary-weighted digital

capacitor bank and a varactor that are both connected in series to the resonator. The measured best phase noise performances of the VCMO are -72 and -153 dBc/Hz at 1 kHz and 10 MHz offsets from 178.23 and 175.83 MHz carriers, respectively. The VCMO consumes a DC of 60 μA from a 1.2 V supply while realizing a tuning range of 2.4 MHz (~ 1.4% tuning range), thereby approaching the 3-3.5% tuning range required for accessing many allocated Industrial, Scientific and Medical (ISM) frequency bands [32]. Such VCMOs can be applied to enable ultralow-power, low phase noise, and wideband RF signal synthesis for emerging applications in IoT.

The rest of the chapter is organized as follows: Section 2.2 first discusses the design of a $LiNbO_3$ resonator in the context of using it later to implement a VCMO for IoT applications. Section 2.3 then focuses on the design and simulated performance of our VCMO. Section 2.4 reports on the measurement results. Finally, Section 2.5 summarizes the chapter.

2.2 LITHIUM NIOBATE RESONATORS FOR LOW-POWER IoT

2.2.1 SH0 $LiNbO_3$ Arrayed RF-MEMS Resonators

As discussed in Chapter 1, large k_t^2 is crucial for achieving a significant potential tuning range of frequency, while a high FoM is essential for low phase noise and low power consumption of VCMOs required in low-power wireless transceivers. Therefore, we focus on the SH0 mode resonators oriented −10° to −Y axis in X-cut $LiNbO_3$ in this chapter since they have been demonstrated with the largest k_t^2 and the highest FoM among all types of LVRs [52].

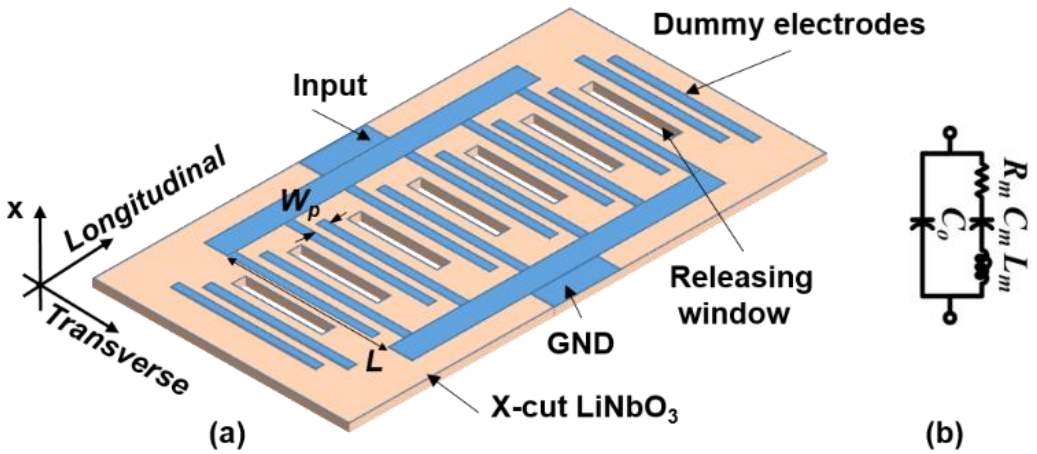

Fig. 2.1. (a) Schematic of an SH0 $LiNbO_3$ LVR array used in this study. (b) MBVD model for the resonator [11].

The schematic of the $LiNbO_3$ device used in this dissertation is shown in Fig. 2.1(a). Different from a conventional LVR, the device in Fig. 2.1(a) consists of a $LiNbO_3$ LVR array made of identical resonators. Each resonator in the array is formed by a pair of interdigitated electrodes (IDEs) on top of a suspended $LiNbO_3$ plate. Provided that the resonators in the array are truly identical, the array electrically behaves the same as a larger resonator that has the same resonant frequency as each comprising resonator [55]. The reasons for using an array, instead of a single LVR, will be explained in Section 2.2.3. For each LVR in the array, the pair of IDEs is alternatingly connected to signal and ground, prompting a time-varying E-field in the film. Through the high piezoelectric coupling coefficients of $LiNbO_3$, E-field launches SH0 mode acoustic waves along both the longitudinal and transverse directions, and forms standing waves at the resonances of various orders due to the reflections at the boundaries of the cavity. The intended series resonant frequency of the resonator, f_s, is set by the IDE pitch (W_p) and overall length of the resonator (L) as given in (2.1).

$$f_s = v\sqrt{\frac{1}{(2W_p)^2} + \frac{1}{(2L)^2}} \approx \frac{v}{2W_p} \tag{2.1}$$

where v is the acoustic wave phase velocity. Multiple resonant frequencies on the same substrate can be achieved by choosing various LVR pitches and lengths, thus enabling on-wafer frequency diversity.

To enable a VCMO with low power consumption, low phase noise, and high tuning range, the resonator is designed to aim for a FoM_{RES} more than 75 with Q larger than 500 and k_t^2 greater than 15%. To achieve an R_m of 50 Ω at f_s of 170 MHz, the C_o is set to 0.3 pF. These values will be used to analyze the tuning mechanism in the next subsection.

2.2.2 Frequency Tuning Mechanism

With access to a high FoM resonator, the next challenge in implementing a high-performance VCMO is to tune its frequency. To achieve a wide tuning range without punishing trade-offs is particularly difficult because there are no effective ways to significantly change the series and anti-resonances of a MEMS resonator. Several mechanisms have been explored, such as capacitive tuning [82] and thermal tuning [83]. However, these techniques either consume significant power or provide very limited tuning ranges. They are only beneficial for environmental corrections or frequency stabilization of a frequency reference oscillator.

Tuning a resonator via electric boundary reconfiguration [84] has been investigated for $LiNbO_3$ LVRs and showed a tuning range of 3%. However, the resonator Q drops greatly in tuning, which degrades the phase noise profile of the

envisioned VCMO. Instead of tuning a single resonator, another method to gain wide coverage of the RF spectrum could be done by networking a bank of monolithic fixed-frequency MEMS resonators in an electrically programmable matrix in which RF switches are used for frequency selection [61]-[63]. The major limitation of this system, in addition to not being continuous in frequency tuning, is the need for many resonators which inadvertently increases the form factor and the cost of the transceiver.

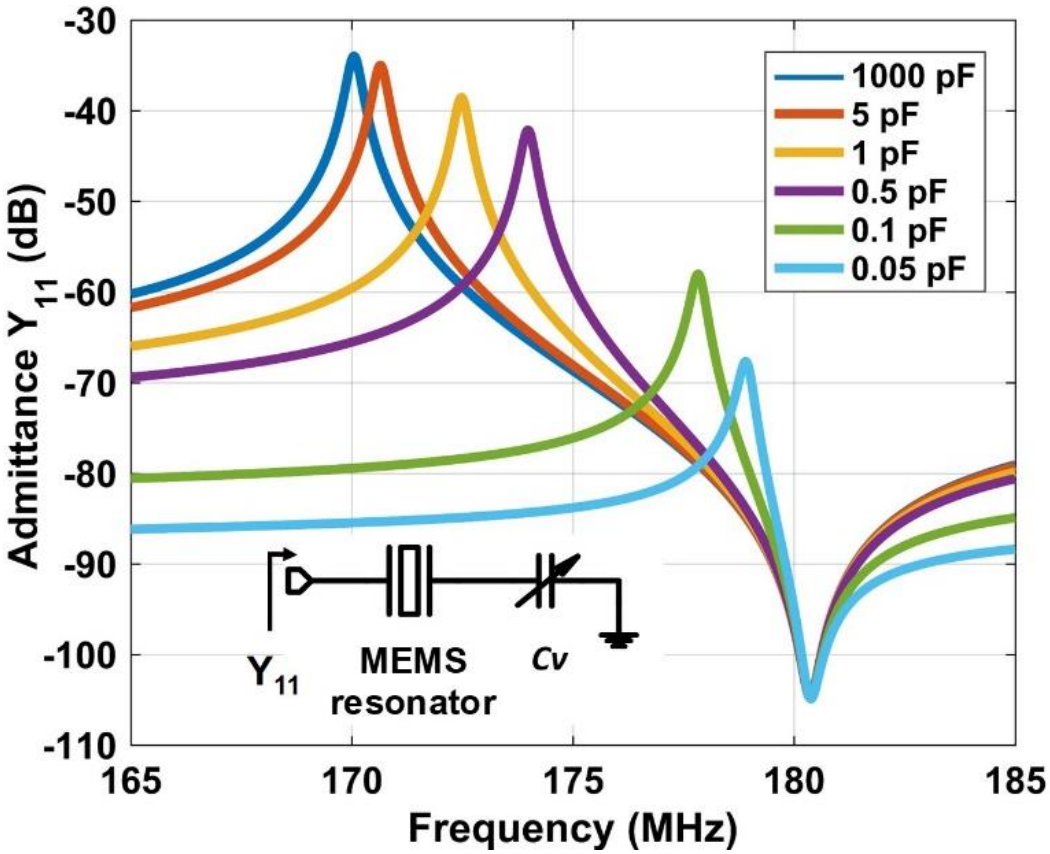

Fig. 2.2. Simulated resonance tuning using a series varactor C_v with decreasing capacitance values [11].

As shown in Fig. 2.2, the approach in this dissertation is to use a high k_t^2 $LiNbO_3$ resonator in combination with a high Q varactor. As the capacitance of the

varactor is tuned, the resonance of the tank is also tuned. The tank here refers to the combination of the resonator and the varactor. A series connection results in the tuning of the series resonance f_s of the tank, while a parallel connection leads to the tuning of the anti-resonance f_p of the tank. In both cases, the tuned resonance moves closer to the other resonance.

Series tuning changes the series-resonant frequency of the tank with minimal effect on the tank loaded quality factor (Q_T) [40], which is given as follows:

$$Q_T \approx \frac{Q_{res}}{1 + \frac{1}{\omega Q_v C_v R_m}} = \frac{R_m}{R_m + R_s} Q_{res} \tag{2.2}$$

where Q_v is the varactor quality factor, C_v is the varactor capacitance, R_s is the series resistance of the varactor, and Q_{res} is the unloaded Q of the resonator. The tuned tank series resonance is given by:

$$f_t = f_s \sqrt{\left(1 + \frac{C_m}{C_o + C_v}\right)} \tag{2.3}$$

The smaller the capacitance C_v added in series to the resonator, the higher the tank series resonance, f_t. Note that the anti-resonance of the tank remains unchanged in tuning. When $C_v = 0$, f_t is tuned to f_p as given in (1.11). On the other hand, when C_v is very large, f_t is tuned to f_s as given in (1.9). Hence, the maximum tuning range is limited to the bandwidth between the series and parallel resonances, which is ultimately set by k_t^2. The maximum fractional tuning bandwidth (FTBW) of the tank can thus be given as:

$$FTBW_{max} = \frac{f_p - f_s}{f_s} \approx \frac{C_m}{2C_o} = \frac{4}{\pi^2} k_t^2 \tag{2.4}$$

As the capacitance of the varactor decreases, the tank input resistance at the tank series resonance, R_t, also increases. Thus, a lower overall Q is expected in the process of tuning the tank frequency as shown in Fig. 2.2. This extra loss must be compensated by increasing the closed loop gain of the oscillator as the VCMO tunes. The gain compensation circuitry is used for this purpose and will be explained in detail in Section 2.3.2. The actual tank FTBW attained in implementation is a function of k_t^2, C_o, and C_v values, and is given as follows:

$$\begin{aligned} FTBW &= \sqrt{1 + \frac{8k_t^2/\pi^2}{1 + C_v^{min}/C_o}} - \sqrt{1 + \frac{8k_t^2/\pi^2}{1 + C_v^{max}/C_o}} \\ &\approx \frac{4k_t^2}{\pi^2} \frac{C_o(C_v^{max} - C_v^{min})}{(C_o + C_v^{min})(C_o + C_v^{max})} \end{aligned} \tag{2.5}$$

where C_v^{max} and C_v^{min} are the maximum and the minimum varactor capacitance, respectively.

Fig. 2.3 shows the effect of the varactor tuning range on the tank FTBW at different k_t^2 values. A larger k_t^2 and a larger varactor tuning range (difference between C_v^{max} and C_v^{min}) translate to a larger FTBW. Since the motional capacitance of the used LVR is quite small (C_m = 37.5 fF), any noticeable tuning would require a very small series varactor (<100 fF) as shown in Fig. 2.3. Note that the tank tuning range does not equate the oscillator tuning range, which is susceptible to other limiting factors that, in addition to the tank FTBW, include

circuit capacitive loading, and power consumption. This topic will be further discussed in Section 2.3.3.

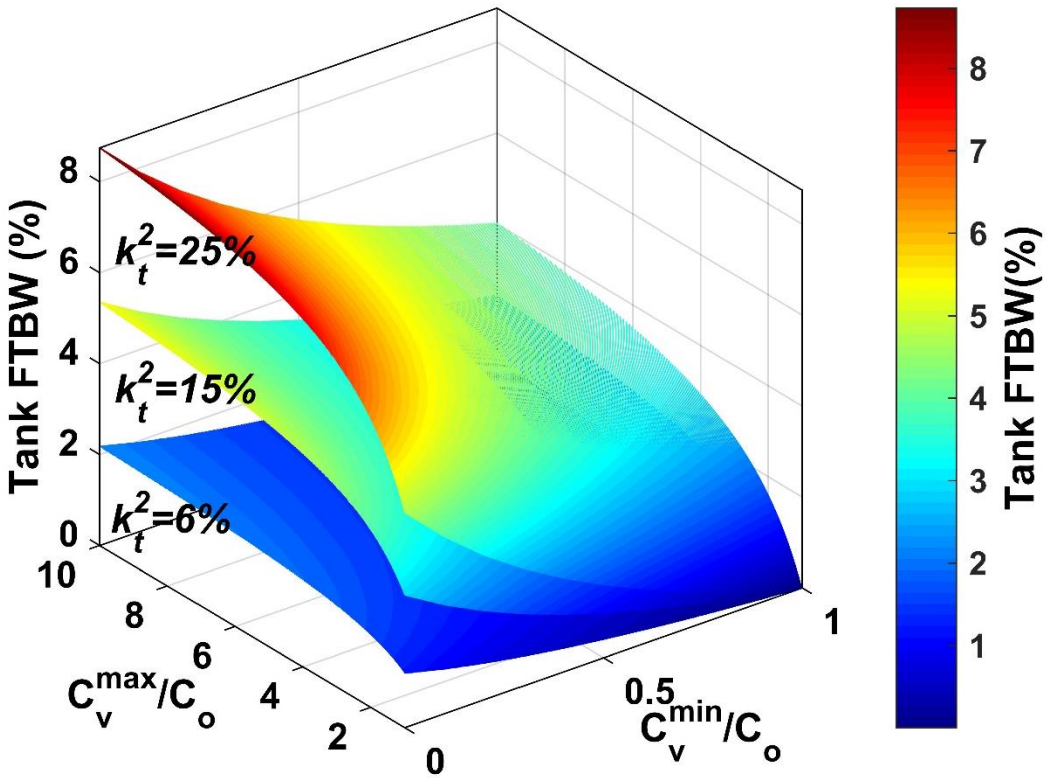

Fig. 2.3. Fractional tuning bandwidth of the tank [11].

2.2.3 Spurious-Free Response in the Tuning Range

Due to the large k_t^2, conventional $LiNbO_3$ LVRs are typically plagued with different kinds of spurious modes. These spurious modes severely degrade the performance of the oscillators as their presence in the frequency spectrum could be mixed with different RF signals in the subsequent stages of the transceiver. Moreover, as the oscillator tunes, it might lock to a spurious mode rather than the intended mode. As a result, an abrupt frequency shift might occur during the tuning of a VCMO. The spurious modes in LVRs originate from several sources, such as

higher-order symmetric overtones [50], asymmetric wave propagation [85], acoustic wave interaction with bus lines and anchors [85], and transversely guided standing waves [86]. Several techniques for removing spurious modes in the AlN [85]-[88] and $LiNbO_3$ [51], [89]-[91] LVRs have been studied and have shown favorable results. However, demonstrating a wideband (>5%) spurious-free LVR is still challenging.

A resonator with a minimum number of interdigitated electrodes (N=2) would attenuate higher-order transverse modes and hence create a larger spurious-free tuning range for wideband oscillators and RF filters [92], [93]. However, using a two-electrode design to suppress spurious modes would reduce the static capacitance (C_o) for a given device length. C_o is determined by the width, overlapping length, and pitch of the IDEs. It is one of the vital factors for achieving a low motional resistance (R_m) as mentioned earlier. To compensate for the loss of the static capacitance from a reduced N, an array of parallel-connected two-electrode resonators can be employed.

Assuming all two-electrode resonators in the array have the same resonance, the response of the array should feature the same resonance as an individual resonator in the array but with a higher static capacitance C_o. Dummy electrodes were employed in the resonators on the edges to ensure structure symmetry and identical resonances for all parallel resonators. It is expected that arraying multiple resonators to mitigate spurious modes should have a minor impact on the k_t^2 attained for the intended mode.

In addition to mitigating transverse modes, arraying can help in reducing the susceptibility of the tuning range to parasitics. The feedthrough capacitance (C_f) between the signal probing pads and the ground lines is typically measured using an on-chip test structure with probing pads and grounding lines identical to the fabricated resonators except for the absence of the metal IDEs [49]. It is important to point out that the MEMS resonator performance is typically reported with the effect of C_f de-embedded [50], [51]. A large C_f reduces the spectral spacing between the series and anti-resonances enabled by the large k_t^2 [59]. According to (2.6), a larger C_o/C_f ratio in this chapter [60], [11], enabled by arraying 11 identical resonators [94], ensures a large tuning range that is less susceptible to parasitics (pads, pad routings, etc.) induced in the integration. Smaller pads and larger separation between the resonator and the pads are crucial for attaining a wide bandwidth.

$$k_t^2 = \frac{C_o + C_f}{C_o} k_{t-measured}^2 \tag{2.6}$$

2.2.4 Standalone Resonator Measurements

The fabrication process of the SH0 $LiNbO_3$ array is similar to the one reported in [95]. The SEM images and measured admittances of the fabricated resonators are shown in Figs. 2.4 and 2.5, with their MBVD model. The extracted component values are listed in the captions. Once we have obtained the input admittance spectra as a function of frequency, the series f_s and parallel f_p resonances are approximately identified as the frequencies at which the magnitudes of the impedance are a minimum and a maximum, respectively. The Q factor is extracted

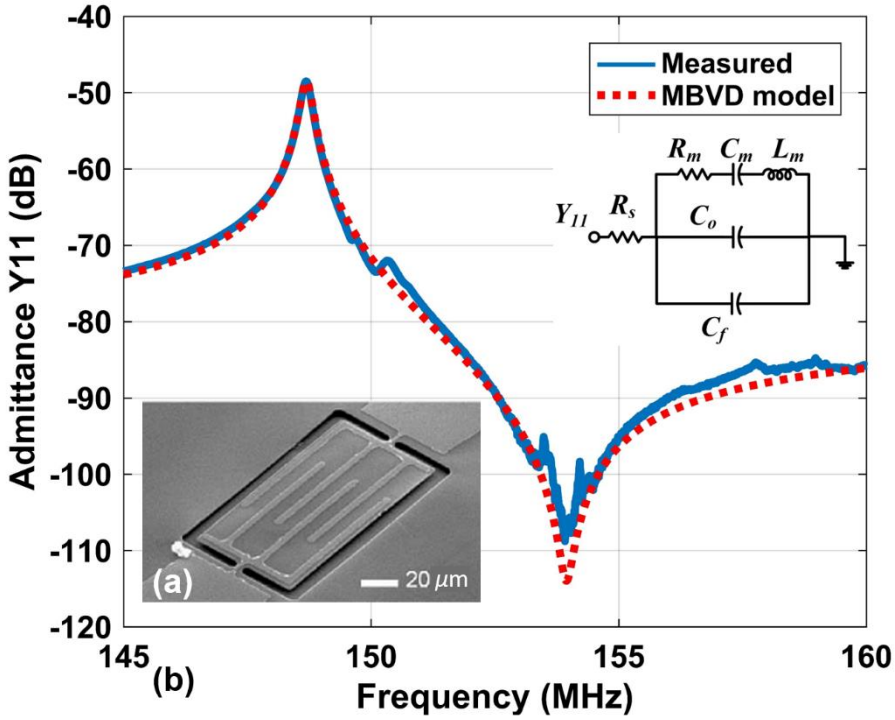

Fig. 2.4. (a) SEM of the conventional $LiNbO_3$ LVR used in [59]. (b) Measured Y_{11}, with MBVD lumped model. (R_m =262 Ω, C_m =6.5 fF, L_m =176 μH, C_o =25.5 fF, C_f =65 fF, R_s =6 Ω, Q =650, and k_t^2=8.7% factoring parasitics) [11].

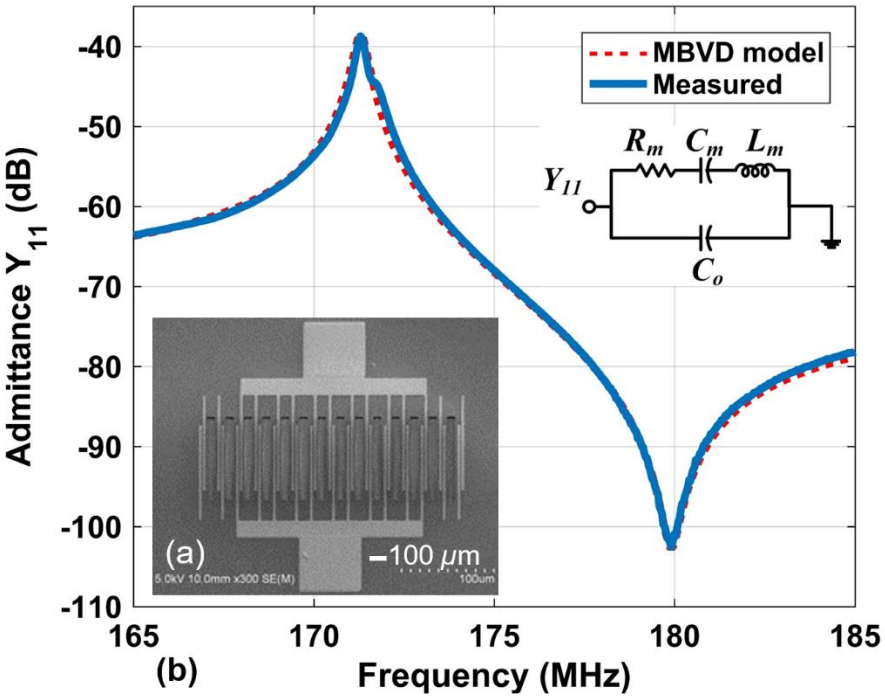

Fig. 2.5. (a) SEM of the $LiNbO_3$ LVR used in [60]. (b) Measured Y_{11}, with the MBVD lumped model result (R_m =85 Ω, C_m =26.765 fF, L_m =32.252 μH, C_o =0.26 pF (including C_f), Q =410, and k_t^2=12.7% factoring parasitics) [11].

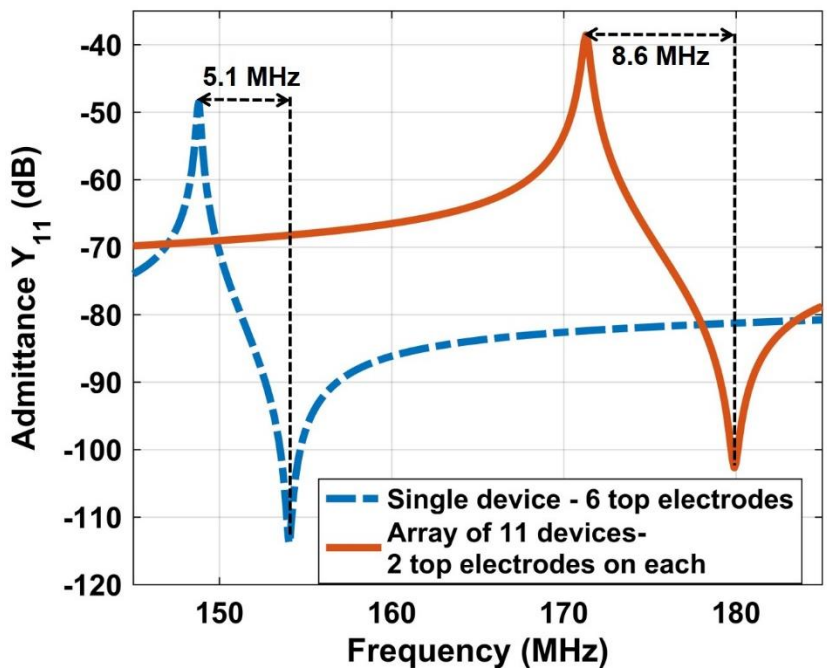

Fig. 2.6. MBVD model fitted response of the conventional resonator [59] and the array resonator [60] with their bandwidth marked [11].

using the 3-dB bandwidth of the resonance (f_s/f_{3db}), while k_t^2 is derived as:

$$k_t^2 = \frac{\pi}{2}\frac{f_s}{f_p}\left(\frac{1}{\tan\left(\frac{\pi}{2}\frac{f_s}{f_p}\right)}\right) \tag{2.7}$$

As shown, the conventional resonator used in [59] consists of six electrodes on the top of a single device, while the device used in [60] is an array of 11 identical resonators that all have two electrodes [11] for the abovementioned benefits. Unlike the conventional resonator with spurious modes near the anti-resonant frequency f_p, the arrayed resonator showed none in the response. Fig. 2.6 shows the MBVD modeled admittance for both resonators with their bandwidth noted. The maximum tuning range allowed by the arrayed device is 8.6 MHz, larger than the 5.1 MHz reported in [59], therefore permitting wider bandwidth VCMOs.

2.3 LOW-POWER VCMO DESIGN

Three types of simple three-point oscillators—Pierce, Colpitts, and Santos [96]—can be used to integrate a MEMS resonator. The only physical difference between the three implementations is which transistor node (drain, source, gate) is AC grounded. Colpitts is chosen in this study to implement the VCMO for its low power consumption in comparison to others. Thanks to the high FoM of $LiNbO_3$ resonators, dc power consumption can be further reduced in contrast to other MEMS-embedded oscillators, as will be shown using the Colpitts small-signal model in Section 2.3.1. Different resonator S-parameters, including Q, C_o, and k_t^2, will be studied in Section 2.3.2 to understand their effects on the power consumption of a Colpitts oscillator. As it will be seen, the insights from the analysis also echo our early design choices for an optimal resonator to interface with the oscillator circuit.

In addition to low power consumption, large tuning range is also a key design goal for this work as a wide tuning range is essential for many IoT applications. Fortunately, the high k_t^2 offered by the $LiNbO_3$ resonator makes a wide tuning range easier to achieve, provided that the oscillator design can properly harness the maximum tuning range permitted by the resonator. To this end, a tunable gain compensation circuitry is used to dynamically overcome the extra losses in the process of tuning so that Barkhausen's conditions can be satisfied over a frequency range that approaches the FTBW highlighted in Section 2.2.2. The use of gain compensation to maintain a wide tuning range implies an inherent tradeoff between tuning range and power consumption, which will be studied in Section

2.3.3. Fundamentally, the tradeoff limits the capacity of oscillator design to leverage the high-performance resonator and consequently bounds the oscillator performance. The frequency and gain tuning circuitry implementation are discussed in Section 2.3.4.

The third metric that we emphasize in this study is phase noise. $LiNbO_3$ resonators with their high Q and FoM_{RES} can be advantageous for low phase noise oscillators. On the circuit side, Colpitts oscillators are enabled to achieve low phase noise performance by turning on the transistor only for a reasonably short fraction during a cycle of oscillation. Because the transistor is off most of the time, it does not significantly contribute to the phase noise of the oscillator. Additionally, due to their simplicity, Colpitts oscillators have been a favored topology in the RF regime [16]. Detailed analysis of the phase noise can be found in Section 2.3.5.

2.3.1 Small-Signal Analysis

The goal of this section is to introduce the Colpitts oscillator schematics and its small-signal analysis. This analysis is important to solve for the Barkhausen's stability criteria of oscillation. Fig. 2.7 shows the Colpitts VCMO schematic used in this study. The circuit is designed with the flexibility to work with different MEMS resonators of different resonant frequencies, f_s, various Q, and a wide range of k_t^2.

In our design, a varactor C_v, formed by a parallel combination of an 8 binary-weighted capacitor bank and a varactor C_{var}, is connected in series with the MEMS resonator to provide coarse and fine frequency tuning, respectively.

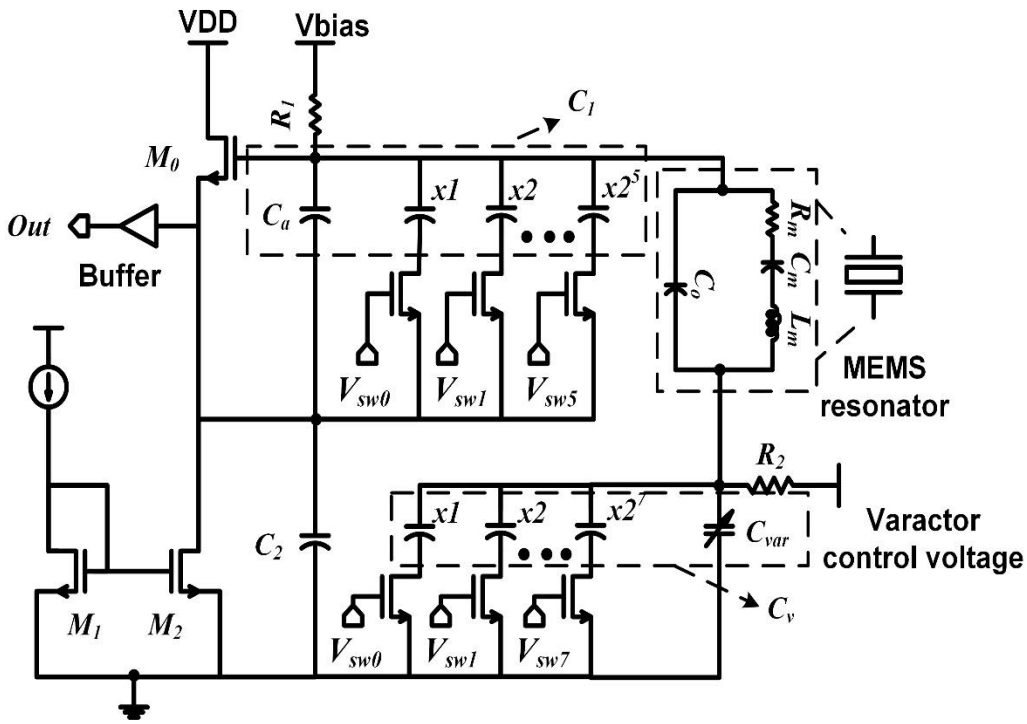

Fig. 2.7. Schematic of the VCMO [11].

The transistor M_0, in combination with the feedback capacitors C_1 and C_2, provides the needed negative resistance R_N to compensate for the losses in the resonator as shown in Fig. 2.8 (a). C_1 consists of a 6 binary-weighted capacitor bank in our implementation, while C_2 is a simple MIM capacitor. C_1 can be dynamically tuned to adjust the closed loop gain to overcome the extra losses while frequency tuning.

The active branch of the Colpitts can be simplified to a negative resistance R_N in series with a load capacitance C_L as shown in Fig. 2.8 (b). They are given as:

$$R_N = \frac{-g_m}{\omega^2 C_1 C_2}, \quad C_L = \frac{C_1 C_2}{C_1 + C_2} \tag{2.8}$$

where ω is the operating angular frequency, and g_m is the small-signal transconductance of M_0. For oscillations to take place, $|real(Z_{in})|$ must be larger than

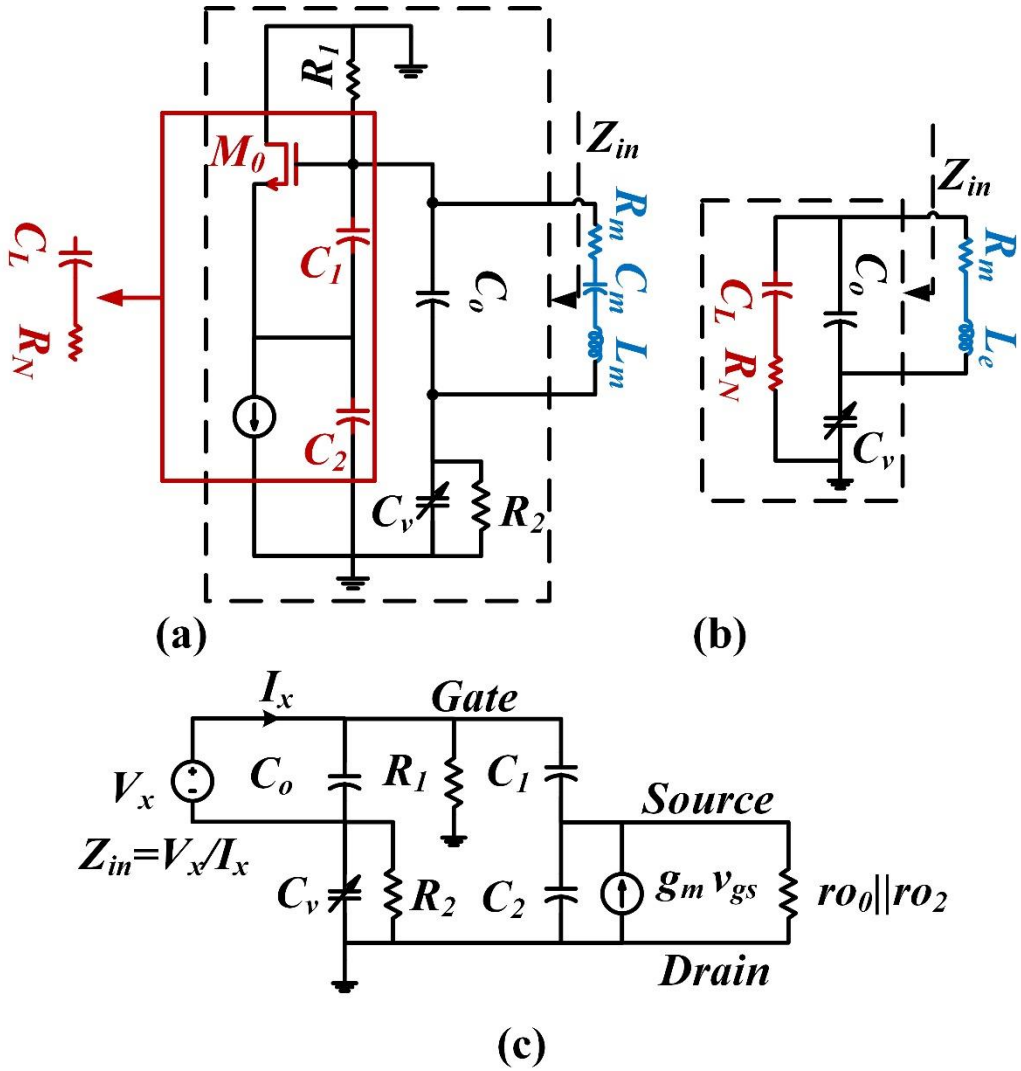

Fig. 2.8. (a) Simplified schematic of the Colpitts oscillator. (b) Simplified schematic for calculating the negative resistance needed for oscillation startup assuming a lossless circuit. (c) Small-signal model of the oscillator including resistive loading [11].

R_m [97]. The impedance seen by the motional branch of the resonator $Z_{in}^{lossless}$ as shown in Fig. 2.8 (b) is given by:

$$Z_{in}^{lossless} = (R_N + \frac{1}{j\omega C_v} + \frac{1}{j\omega C_L}) || \frac{1}{j\omega C_o} \tag{2.9}$$

The real and imaginary parts of Z_{in} can be expressed respectively as:

$$real\left(Z_{in}^{lossless}\right) = \frac{R_N {C_T}^2}{(\omega R_N C_T C_o)^2 + (C_T + C_o)^2} \tag{2.10}$$

$$imag\left(Z_{in}^{lossless}\right) = -\frac{\frac{C_T + C_o}{\omega} + \omega {R_N}^2 {C_T}^2 C_o}{(\omega R_N C_T C_o)^2 + (C_T + C_o)^2} \tag{2.11}$$

where C_v is the varactor capacitance, C_T is the series combination of C_v and C_L, and is given as $(C_L\ C_v) / (C_L + C_v)$.

Equations (2.8) – (2.11) are simplified as the output resistances of M_0 and M_2, as well as biasing resistors R_1 and R_2, are neglected. They still provide good insights for designing a low-power VCMO. More accurate equations that consider all the losses are given below:

$$Y_n = G_n + j\omega C_n \tag{2.12}$$

$$Z_{in} = \left((Z_1 + Z_2 + g_m Z_1 Z_2) || R_1 + Z_{cv}\right) || \frac{1}{j\omega C_o} \tag{2.13}$$

where Y_n is the admittance at a certain node, $Z_n = 1/Y_n$ is the impedance at a certain node, and n is the index denoting the node. G_n is the conductance part of the admittance, and C_n is the capacitive part of an admittance. For example, $Y_1 = G_1 + j\omega C_1$, $Y_2 = G_2 + j\omega C_2$, and $Y_{cv} = G_{cv} + j\omega C_v$.

A comparison between SpectreRF simulations, and lossless and lossy equations, is shown in Fig. 2.9. The result from (2.10) does not match the simulations at low frequencies. Equation (2.10) predicts more gain out of the circuit because it assumes a lossless circuit and hence considers no resistive loading to the

resonator. Moreover, the equation predicts a negative impedance at dc, which is not the real case. However, it remains intuitive for the initial design phase. Equation (2.13), on the other hand, takes all the losses into account and matches well with the simulations. This equation can be formalized analytically with the help of the small-signal model shown in Fig. 2.8(c). Yet when simplified to have a closed form equation in terms of different circuit parameters, it becomes cumbersome without offering any design intuition.

Now, after analyzing the Colpitts' small-signal model, we introduce the Barkhausen oscillation criteria. They are given below:

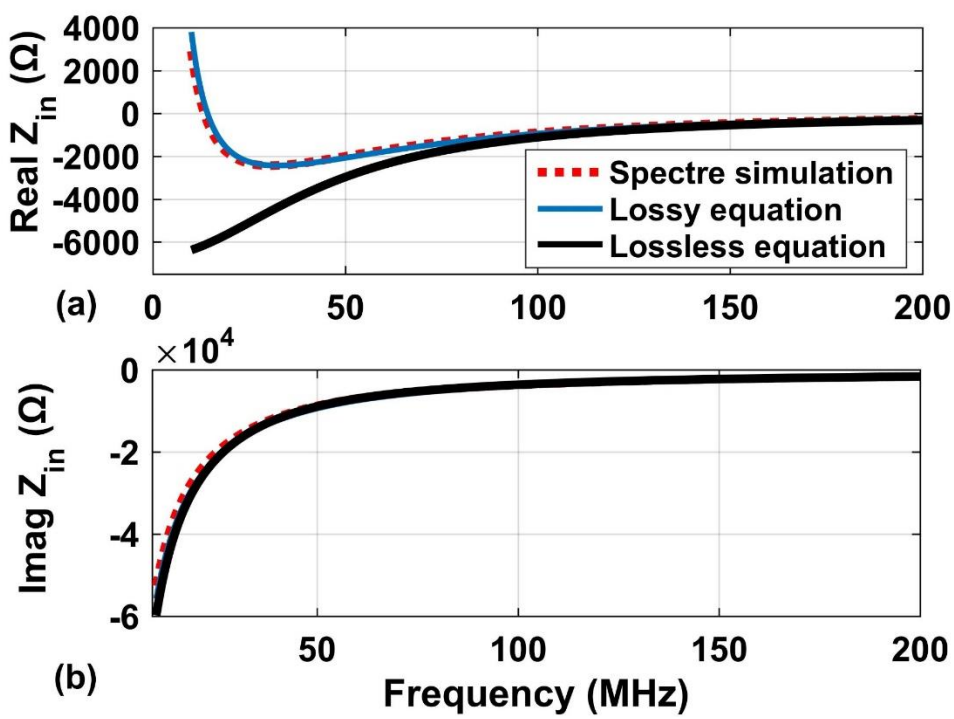

Fig. 2.9. Comparison of (a) real and (b) imaginary parts of Z_{in} versus frequency, attained via analytical equations and SpectreRF simulations. The component values used in this simulation are as follows: C_1=0.65 pF, C_2 =0.5 pF, C_o= 0.26 pF, g_m=680 μS, C_v=2.56 pF, R_1= R_2=400 kΩ, G_2=44.8 μS, where $G_2=1/(r_{o0}||r_{o2})$ and r_o is the output impedance of a transistor [11].

$$real\big(Z_{in}(\omega, g_{mc})\big) + R_m = 0 \tag{2.14}$$

$$imag\big(Z_m(\omega_o)\big) + imag\big(Z_{in}(\omega_o)\big) = 0 \tag{2.15}$$

By equating $real(Z_{in})$ with $-R_m$, the critical transconductance g_{mc}, as well as the minimal power consumption for starting oscillations, can be estimated. Moreover, the oscillation frequency f_o ($\omega_o = 2\pi f_o$) can be calculated by solving for (2.15). The following section uses (2.13) to analyze how Q, C_o, and k_t^2 of the resonator affect the power consumption of the Colpitts oscillator.

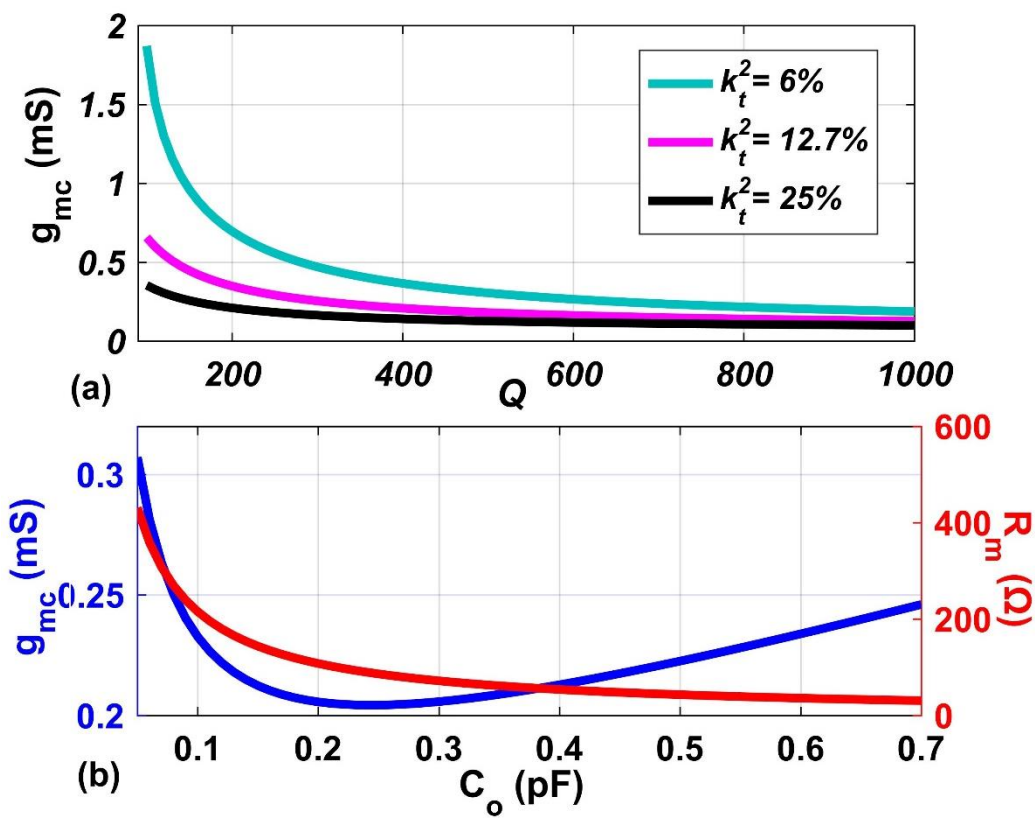

Fig. 2.10. (a) Critical transconductance g_{mc} versus Q for different k_t^2 values. C_o is 0.26 pF and R_m =85 Ω. (b) g_{mc} and R_m versus C_o with k_t^2= 12.7%, and Q of 410. The component values used in both simulations: C_1 =0.65 pF, C_2 =0.5 pF, C_v =2.56 pF, R_1 = R_2 =400 kΩ, G_2 =44.8 μS. Frequency of oscillation was set to 175 MHz by the motional impedance and the loading capacitors [11].

2.3.2 Resonator for Low-Power Tunable Oscillator

In our co-design of piezoelectric MEMS resonators and CMOS, Fig. 2.10 highlights what the optimal design specifications of a $LiNbO_3$ resonator are for a Colpitts oscillator. This study is agnostic and applicable to different circuit platforms found nowadays, ranging from CMOS with different technology nodes to MMICs, discrete, and others. As seen in Fig. 2.10, larger Q and k_t^2 help to reduce the power consumption of the system by lowering g_{mc}. A Q larger than 500, however, does not help much in reducing the power consumption, although better phase noise can be expected from a higher Q. A similar trend applies for k_t^2 in terms of lowering power consumption, despite that a higher k_t^2 should be pursued for a wider tuning range.

According to (1.4), a larger resonator (larger C_o) gives smaller R_m. Large resonators might be beneficial for low-power oscillators at very low frequencies. However, in the RF regime, there is a clear tradeoff between R_m and C_o that has to be considered in designing piezoelectric resonators for high-frequency and low-power VCMOs. Solving (2.14) for g_{mc}, one can find that g_{mc} has a parabolic relation with C_o with a minimum value set by C_o and R_m for a specific Colpitts design. Intuitively, a larger R_m resulted from smaller resonator size gives rise to a larger g_{mc}. Thus, it is natural that g_{mc} value drops as C_o increases. However, such reduction of g_{mc} is only up to a certain point where further increasing the resonator size would reduce the negative resistance ($|real\ (Z_{in})|$) to be less than R_m and start to require more gain in the loop to satisfy the Barkhausen condition. The local optimum of g_{mc} originates from the fact that $|real\ (Z_{in})|$ drops more aggressively than R_m as C_o

increases. This tradeoff is shown in Fig. 2.10 for a specific Colpitts oscillator design. For our design, the optimal C_o for achieving low power consumption falls between 200 and 300 fF.

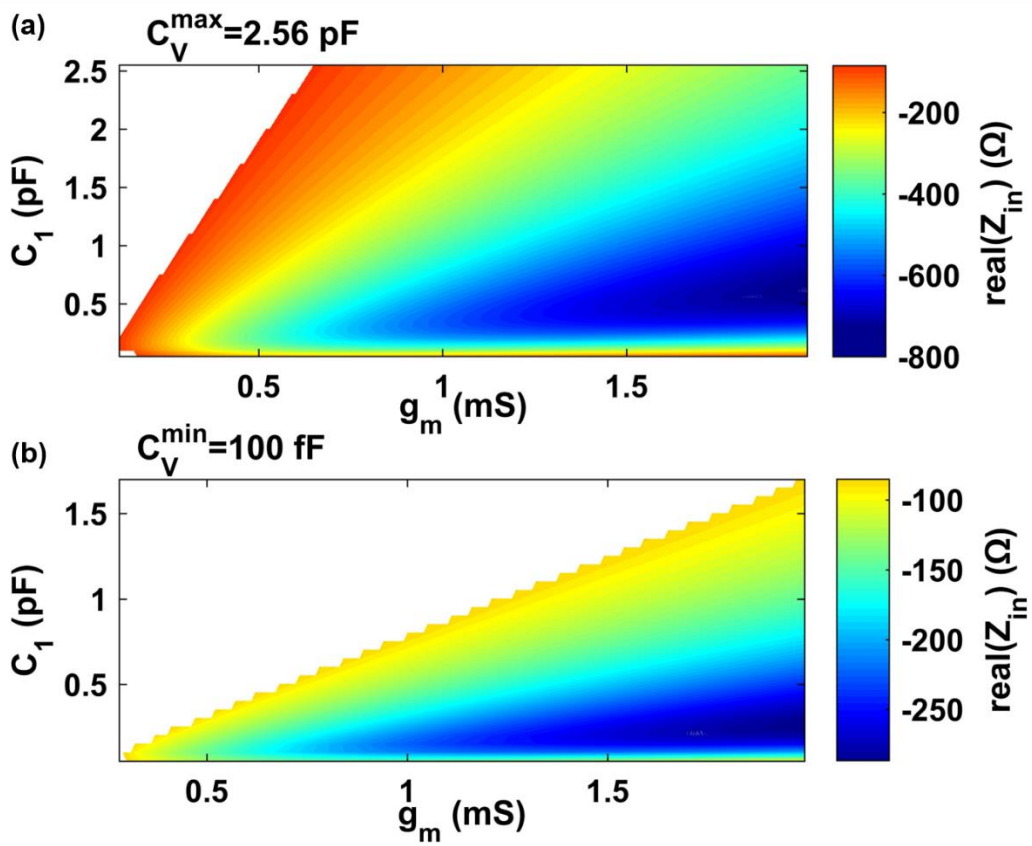

Fig. 2.11. Negative resistance as a function of C_1 and g_m for (a) C_v^{max} of 2.56 pF. (b) C_v^{min} of 100 fF [11].

2.3.3 Tradeoffs Among Tuning Range, Gain and Power Consumption

In our VCMO design, we have a tradeoff between power consumption and tuning range that can be improved with gain compensation. In this section we will analyze these tradeoffs based on (2.13) - (2.15). We first examine the tradeoff between gain (equivalent to the negative resistance) and power consumption (equivalent to g_m). Fig. 2.11 shows the effects of g_m and C_1 on the negative

resistance seen by the motional arm of the LVR at the minimum and maximum oscillation frequencies (f_o). Fig 2.11 (a) shows the negative resistance with a varactor capacitance of 2.56 pF for the operation at the minimal oscillation frequency. Fig. 2.11 (b) shows the negative resistance with a varactor capacitance of 0.1 pF for the operation at the maximum oscillation frequency. The forbidden regions of oscillation where the $|real\ (Z_{in})| < 85\ \Omega$ are whitened so as not to appear in the plots. A larger gain is expected with a larger g_m value and a small C_1 in certain ranges. Instead of increasing the g_m via pumping more dc current in the circuit to compensate for the extra losses in the loop while tuning the oscillation frequency, C_1 values can be reduced to increase the gain and overcome the extra losses without increasing the dc power consumption as shown in Fig. 2.11. Hence, the importance of the gain compensation circuitry implemented via tuning C_1 in saving dc power consumption is justified in our design.

Second, we examine the tradeoff between the tuning range and power consumption. Fig. 2.12 shows f_o versus g_m and C_1 values with C_v^{max} of 2.56 pF and C_v^{min} of 100 fF. It can be deduced from the plot that a higher f_o is expected via increasing g_m for a specific C_1 value or decreasing C_1 value for a specific g_m value. Figs. 2.11 and 2.12 are helpful in setting the g_m and the range of C_1 values needed to realize the gain compensation circuitry for a low-power tunable VCMO targeting IoT applications. C_1 maximum value was set to 0.65 pF while g_m was fixed to 680 μS. The *W/L* ratio of M_0 transistor was chosen so that the oscillator consumes a DC of 60 μA ($I_d = g_m v_{ov}/2$). v_{ov} is the overdrive voltage of M_0. C_2 was fixed to 0.5 pF.

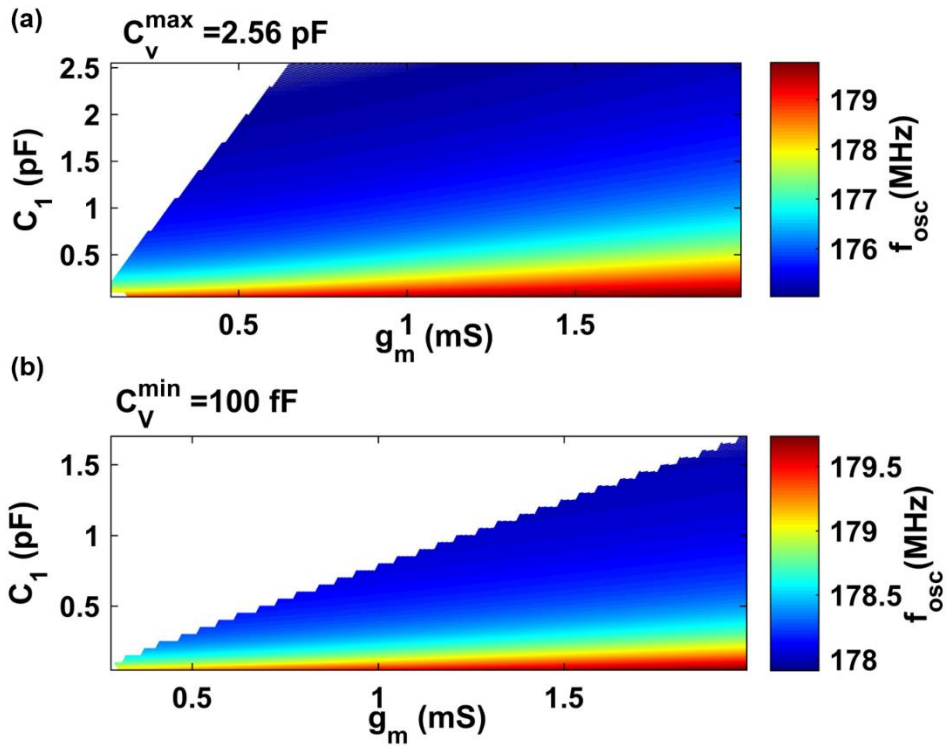

Fig. 2.12. Oscillation frequency as a function of C_1 and g_m for (a) C_v^{max} of 2.56 pF. (b) C_v^{min} of 100 fF [11].

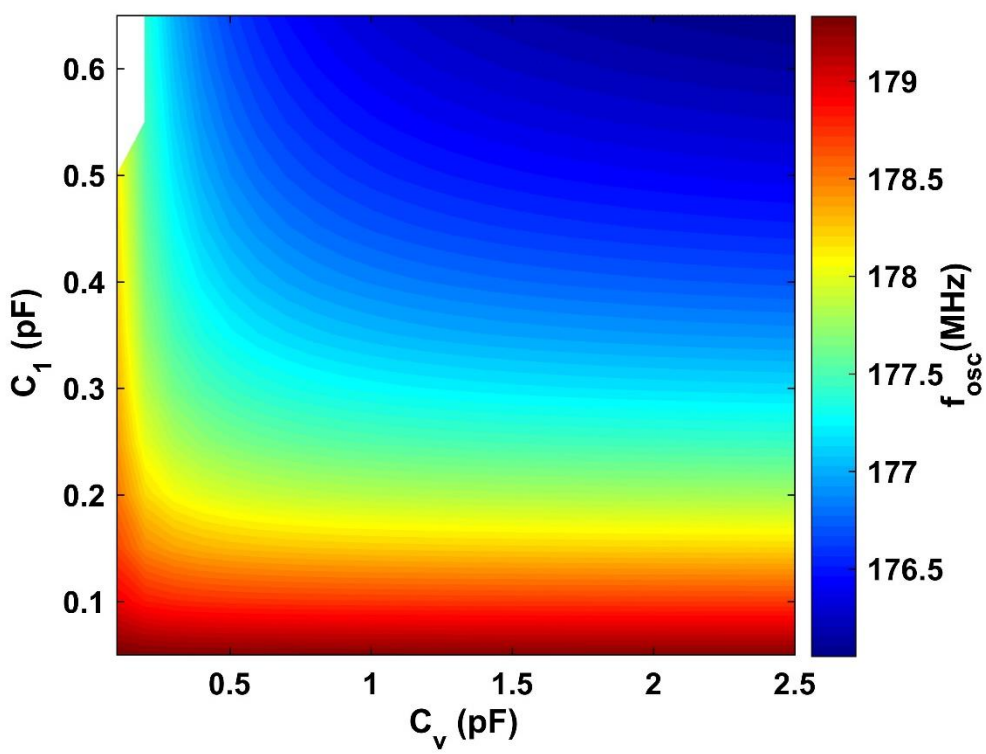

Fig. 2.13. Oscillation frequency as a function of C_1 and C_v [11].

To complete our study, we studied how C_1 and C_v simultaneously affect the tuning range at a fixed g_m of 680 μS. The results are shown in Fig. 2.13 with a simulated tuning range around 3.2 MHz. It can be concluded from the plot that smaller C_1 and C_v values increase the tuning range of the VCMO. The following equation was used to produce Fig. 2.13.

$$f_o^{lossless} = f_s\sqrt{\left(1 + \frac{C_m}{C_o + C_T}\right)} \tag{2.16}$$

Equation (2.16) predicts f_o assuming a lossless circuit. Hence it is the solution for (2.15) for very small g_m values. It can be easily derived using (1.9) and (2.11). Equation (2.16) becomes very handy especially for low-power VCMOs design.

2.3.4 Tuning Circuitry Implementation

Coarse and fine tuning of the oscillation frequency are implemented by respectively controlling an 8 binary-weighted capacitor bank and a varactor C_{var} that are connected in parallel to form C_v. The digital capacitor bank provides discrete capacitance values while the varactor covers the gap between adjacent discrete capacitance values in an analog and continuous fashion.

A second 6 binary-weighted capacitor bank is used to implement C_1 for additional control of the oscillators' closed-loop gain and phase as shown in Fig. 2.7. There was no need for continuous gain tuning while tuning the frequency, hence the varactor was omitted in the gain compensation circuitry implementation. The 6 least significant control bits of C_v are coupled to the 6 control bits of C_1 so that frequency and gain tuning are done in tandem to adaptively allow for the

designed tuning range and lower power. In other words, the tuning of C_v and C_1 follows a certain trajectory in Fig. 2.13 to achieve the frequency tuning and its required gain tuning.

Each digital capacitor is controlled via an on-chip RF switch through digital inputs (1 or 0). For the 8-bit varactor bank, when the input is set to 1 and the switch is turned on, the resonator is coupled with a larger capacitance in series, thus inducing a lower frequency of oscillation. Otherwise, 0 is applied to turn the switch off for a smaller capacitance loading and a higher frequency of oscillation. In other words, the 8-bit code is fed to the switches for rendering capacitance values ranging from 10 fF to 2.56 pF with a step of 10 fF. The varactor dimensions are designed to attain a favorable trade-off between the varactor Q and its capacitance tuning range (30 fF at 0 V to 50 fF at 1.2 V) so that the varactor does not significantly reduce the overall Q of the tank while no dead zones exist over the entire tuning range of the oscillation frequency.

To complete our study, transient simulations of the current consumption during startup and steady state for different frequencies of oscillation set by the variations of control bits are shown in Fig. 2.14 (a). Input words of 11111111, 11000000, 10000000, 01000000, and 00000011 correspond to five frequencies ranging from 175.83 MHz to 178.23 MHz were used to investigate the power consumption versus the oscillation frequency. As shown in Fig. 2.14 (a), the amplitude of the current consumption decreases with an increasing frequency due to the combined effect of two factors. First, a higher loss in the loop at a higher oscillation frequency induces a smaller closed-loop swing and gain at the steady-

state, as also mentioned in Section 2.2.2. On the other hand, the transistor M_0 remains in the ON state for a longer time at a higher oscillation frequency as shown in the zoom-in Figs. 2.14 (b) and (c). Considering both effects (smaller and wider current spikes as tuning up the frequency), the average current consumption over the entire tuning range remains approximately 60 μA.

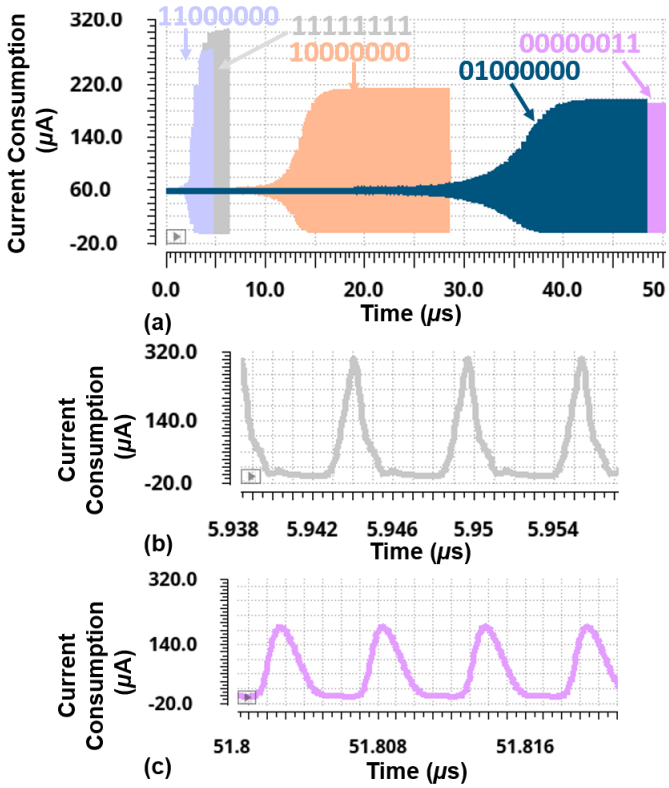

Fig. 2.14. (a) Simulated current consumption during startup and steady state for different control bits. Input words of 11111111, 11000000, 10000000, 01000000, and 00000011 correspond to five frequencies ranging from 175.83 MHz to 178.23 MHz. (b) Zoomed-in view on the current consumption for the 11111111 state (lowest oscillation frequency). (c) Zoomed-in view on the current consumption for the 00000011 state (highest oscillation frequency) [11].

The VCMO was implemented using TSMC RF LP 65 nm kit. M_0 and all RF switches are RF low voltage threshold transistors (LVTs), while M_1 and M_2 are analog high voltage threshold transistors (HVTs) with a large channel length for

better current mirroring accuracy and less flicker noise contribution to the oscillator. The bias point of the M_0 is chosen to optimize the phase noise and to satisfy the closed-loop gain requirements simultaneously. RF switches are carefully sized to reduce their flicker noise contribution while providing a sufficiently small C_{off} for a wide tuning rage. R_1 and R_2 are set to be large enough (400 kΩ) to minimize overloading the resonator. The on-chip buffer is designed for a 50 Ω measurement system, and the input of the buffer is coupled from the source of M_0 rather than the gate to minimize the loading on the resonator.

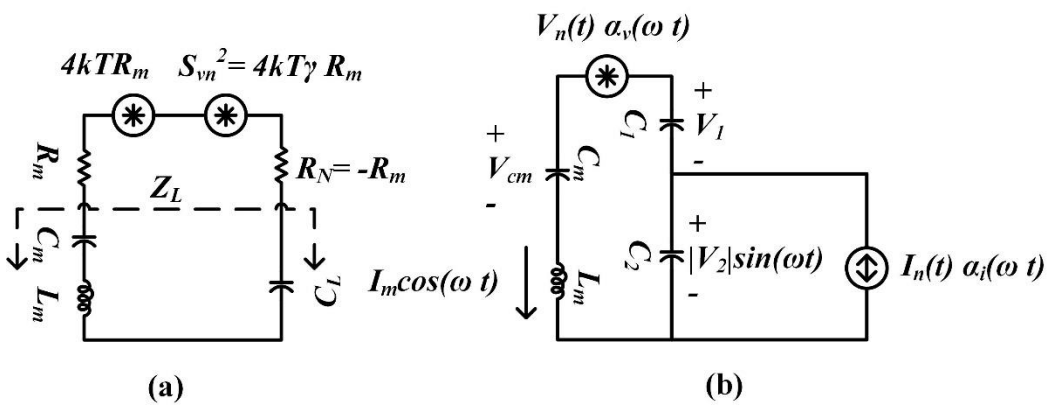

Fig. 2.15. Noise calculation using (a) equivalent circuit at stable oscillation, (b) equivalent circuit for linear time variant analysis, noise sources are R_m, M_0 and biasing transistors' white and flicker noises [11].

2.3.5 Phase Noise Analysis

Q_L mentioned in (1.1) is defined as:

$$Q_L = \frac{R_T}{R_{load} + R_T} Q_T \tag{2.17}$$

where R_{load} is the loading circuitry resistance on the resonator. It should be minimized to maximize Q_L for a good phase noise performance. Q_T is the quality

factor of the tank (resonator and varactor combined). R_T is the series resistance of the tank. The Leeson frequency f_L, given in (2.18), can be used to estimate Q_L.

$$f_L = \frac{f_o}{2Q_L} \tag{2.18}$$

Now, a general simple analysis will be presented to prove the power spectrum of the phase noise $S_{\varphi_n^2}$ in the $1/f^2$ regime. The equivalent circuit of the oscillator at a stable condition is shown in Fig. 2.15. (a) [20]. At a stable oscillation, (2.13) applies and hence an open-loop circuit voltage noise V_n of a spectral density $S_{v_n^2}$ is also present. $S_{v_n^2}$ is given as:

$$S_{v_n^2} = 4kT\gamma R_m \tag{2.19}$$

where γ is the noise excess factor that depends on the noise contributions from all the noise sources in the circuit as will be shown later. At a stable oscillation, the impedance Z_L that loads the total noise voltage source of spectral density $4kTR_m$ $(1+\gamma)$ is given by:

$$Z_L \approx 2j\omega L_m \frac{\omega_n - \omega_o}{\omega} = 2jQR_m \frac{f_n - f_o}{f} \tag{2.20}$$

where f_n is the noise frequency. The power spectral density of the noise current I_{nL} flowing in the loop is given by:

$$S_{I_{nL}^2} = \frac{4kT(1+\gamma)R_m}{|Z_L|^2} = \frac{4kTF}{R_m}\left(\frac{f}{2Qf_m}\right)^2 \tag{2.21}$$

where $f_m = f_n - f_o$. This power spectral density takes the R_m noise (γ = 0) into account. The open-loop current noise I_{nL} will be added to the motional current I_m in the motional arm of the MBVD model of the resonator. The power spectrum of the phase noise $S_{\varphi_n^2}$ is given as:

$$S_{\varphi_n^2} = \frac{1}{2}\frac{S_{I_{nL}^2}}{(|I_m|/\sqrt{2})^2} = \frac{4kTF}{R_m|I_m|^2}\left(\frac{f}{2Qf_m}\right)^2 \tag{2.22}$$

where the phase noise floor is the first term of (2.22) and it is the far-from-carrier noise associated with an oscillator.

2.3.5.1 Linear Time-Invariant Colpitts Detailed Solution

Let us narrow our previous general analysis to our Colpitts oscillator. Assuming that the oscillator is lossless, linear, and time-invariant, and via neglecting the feedback path effect on the noise for simplicity, a detailed solution can be found for the white phase noise.

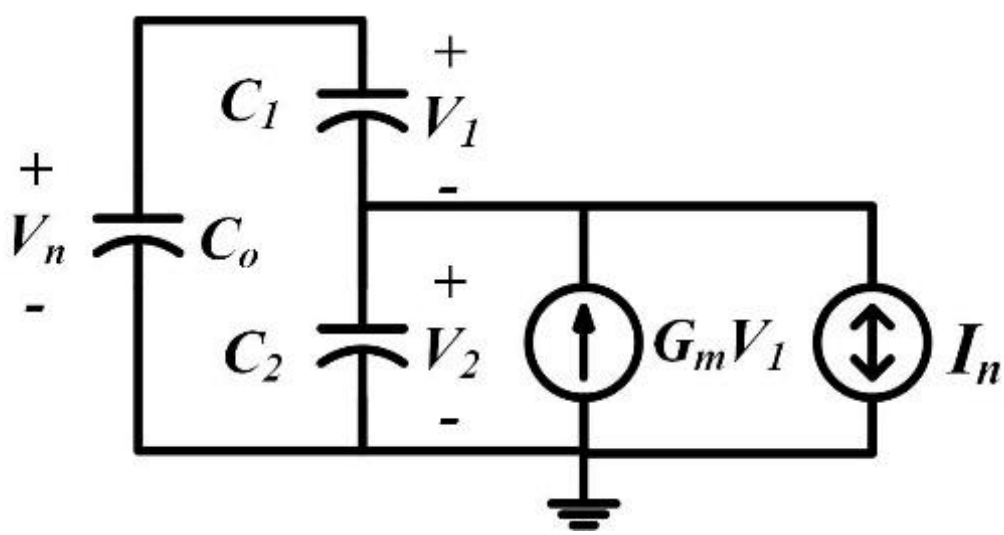

Fig. 2.16. Simplified equivalent circuit to calculate V_n from a single noise current source I_n [11].

I_m at a stable oscillation can be given as:

$$I_m = -\frac{j\omega C_1 V_1}{1 + j\omega C_o Z_m^{stable}} \tag{2.23}$$

where $Z_m^{stable} = R_m - imag\left(Z_{in}^{lossless}\right)$.

If we assume that $R_m << \max\left(real\left(Z_{in}^{lossless}\right)\right)$, then $imag\left(Z_{in}^{lossless}\right)$ can be reduced to $1/(j\omega(C_o + C_T))$. Hence,

$$I_m = -\frac{j\omega C_1 V_1}{1 - \frac{C_o}{C_o + C_T} + j\omega C_o R_m} \tag{2.24}$$

$$|I_m| = \frac{\omega C_1 |V_1|}{\sqrt{\left(1 - \frac{C_o}{C_o + C_T}\right)^2 + (\omega C_o R_m)^2}} \tag{2.25}$$

where the last term in the denominator of (2.25) is inversely proportional to the resonator $FoM^2 = (Qk_t^2)^2$ and can be neglected for a high FoM resonator. Hence,

$$|I_m| = \omega C_1 |V_1| \left(1 + \frac{C_o}{C_T}\right) \tag{2.26}$$

V_n as a function of the noise current I_n shown in Fig. 2.16 can be expressed as:

$$v_n = \frac{I_n}{SC_2\left(1 + \frac{C_o}{C_v} + \frac{C_o}{C_1}\right) + SC_o + \frac{C_o}{C_1} G_m} \tag{2.27}$$

where I_n is the summation of the switching transistor M_0 channel noise and the bias transistor white noise, and $S = j2\pi f_n$. The circuit noise excess factor for small amplitudes γ_o is given by:

$$\gamma_o = \frac{S_{v_n^2}}{4kTR_m} = \frac{S_{I_n^2}}{4kTR_m\left(SC_2\left(1+\frac{C_o}{C_v}+\frac{C_o}{C_1}\right)+SC_o+\frac{C_o}{C_1}G_m\right)^2} \qquad (2.28)$$

where $S_{I_n^2} = 4kT\gamma_t(g_{mc} + g_{mbias})$, γ_t is the M_0 channel noise excess factor, and g_{mbias} is the transconductance of the bias transistor. By using $F = 1+\gamma_o$ and substituting (2.28) in (2.22), a detailed analysis for the Colpitts linear time-invariant phase noise is presented.

2.3.5.2 Linear Time-Variant Colpitts Detailed Solution

Equation (2.22) is only applicable under the assumption that the noise sources are time-invariant sources. The noise generated by the transistors becomes cyclostationary and hence time variant. Phase noise can then be examined by using the impulse sensitivity function (ISF) [16]. Two uncorrelated noise sources—a voltage noise source $V_n(t)$ $\alpha_v(\omega t)$ and a current noise source $I_n(t)$ $\alpha_i(\omega t)$—are shown in Fig. 2.15(b). $\alpha_v(\omega t)$ and $\alpha_i(\omega t)$ are the modulation functions synchronized with current and voltage, respectively. Those functions represent the time variance of the noise sources.

For R_m noise in the resonator, $\alpha_v(\omega t) = 1$ [16]. Hence the white phase noise density spectrum generated by R_m is the same as that given in (2.22) when F=1. For a white noise current $I_n(t)$ of a spectral density $S_{I_{n\_white}^2}$, the white phase noise spectrum $S_{\varphi_{n\_white}^2}$ can be calculated as:

$$S_{\varphi^2_{n\_white}} = \frac{1}{2}\frac{\overline{\Gamma_i^2}\, S_{I^2_{n\_white}}}{(C_2|V_2|)^2(f_m)^2}\left(\frac{C_m}{C_2 + C_o\left(1 + \frac{C_2}{C_1} + \frac{C_2}{C_v}\right)}\right)^2 \tag{2.29}$$

$$\Gamma_i = -\cos(\varphi)\alpha_i(\varphi) \tag{2.30}$$

$$V_2 = -\frac{V_1}{j\omega C_2}(g_{mc} + j\omega C_1) \tag{2.31}$$

where Γ_i is the effective impulse sensitivity function (ISF) for the sinusoidal current $|V_2|\sin\varphi$, $C_2|V_2|$ is the maximum charge value on the capacitor C_2, and $|V_1|$ is the magnitude of the gate to source voltage of M_0. The last term of (2.29) resembles the square of the fraction of the total voltage on C_m that appears across C_2. In the case of M_0 strictly working in strong inversion, $\overline{\Gamma_i^2} = 0.5$ [20].

For a flicker noise current source of a spectral density $S_{I^2_{n\_flicker}}$, the flicker phase noise spectral density $S_{\varphi^2_{n\_flicker}}$ is given as:

$$S_{\varphi^2_{n\_flicker}} = \frac{(\overline{\Gamma_i})^2\, S_{I^2_{n\_flicker}}}{(C_2|V_2|)^2(f_m)^2}\left(\frac{C_m}{C_2 + C_o\left(1 + \frac{C_2}{C_1} + \frac{C_2}{C_v}\right)}\right)^2 \tag{2.32}$$

$$S_{I^2_{n\_flicker}} = \frac{k_f {g_{mc}}^2}{f_m} \tag{2.33}$$

$$(\overline{\Gamma_i})^2 = \left[\frac{|V_1|}{2V_{ov}}\sin(\Delta\varphi)\right]^2 \tag{2.34}$$

where $\Delta\varphi$ is the phase shift across the resonator and can be calculated as:

$$\Delta\varphi = \text{angle}\,(V_1 + V_2) = \tan^{-1}\left(\frac{g_{mc}}{\omega C_2\left(1 - \frac{C_1}{C_2}\right)}\right) \tag{2.35}$$

The summation of the noise floor, (2.22), (2.29), and (2.32) gives the total phase noise of the oscillator. The prediction will be shown in the next section in comparison with the simulated and measured phase noise performances.

For a good phase noise performance, the capacitor C_2, C_1/C_2 ratio, the W/L of the transistor M_0, and the current bias I_0 have been optimized using SpectreRF. The values were chosen to ensure a large amplitude swing and sufficiently high overdrive voltage to reduce the conduction angles of M_0, consequently reducing the noise injection in the loop and the phase noise [16].

2.4 VCMO MEASUREMENTS

The fabricated CMOS chip using TSMC LP RF 65 nm kit is shown in Fig. 2.17. The chip was integrated with the MEMS resonator via wire bonding. The VCMO was tested using a probe station where the output was sensed using 100 μm pitch GSG probes. A dc probe with large decoupling capacitors between the power and ground tips was used to deliver the dc inputs and the control signals of the RF switches.

Phase noise measurements were taken using an Agilent E5052A signal source analyzer and are reported in Fig. 2.18 alongside results from analytical equations and simulation. The prediction is in good agreement with the measured results; the small discrepancy in the analytical results is due to considering the unloaded Q of the resonator rather than the loaded Q in our phase noise calculations.

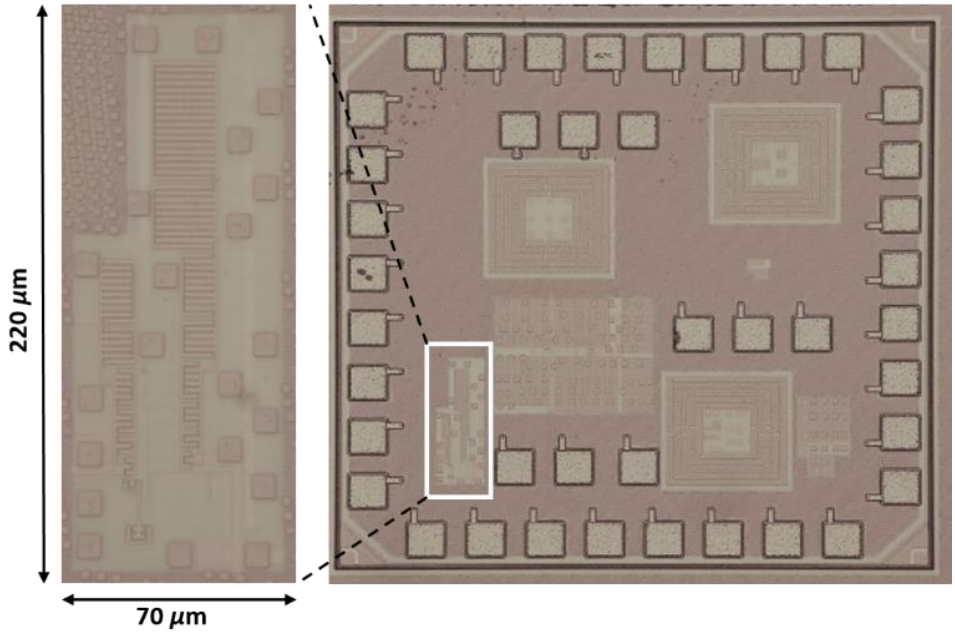

Fig. 2.17. Microscope zoomed image of the VCMO on the left, 2×2 mm^2 chip on the right that includes other circuitry [11].

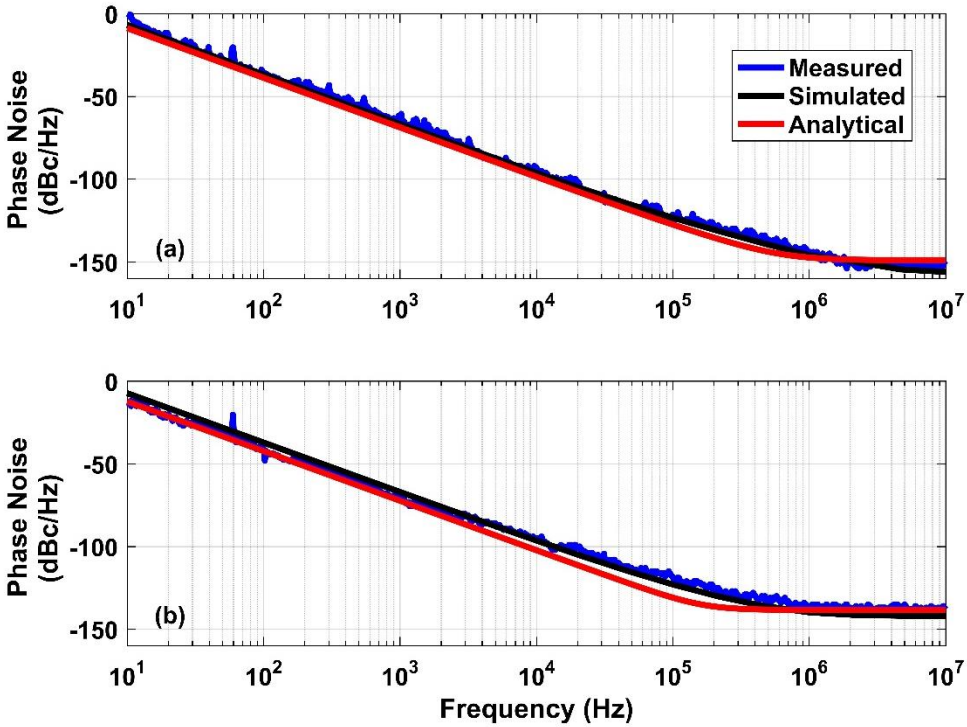

Fig. 2.18. Analytical, simulated and measured phase noise. Resonator specifications: C_o=0.26 pF, k_t^2= 12.7%, and Q= 410. (a) C_v= 2.56 pF. (b) C_v= 100 fF [11].

SpectreRF simulations are crucial for an accurate noise profile. Identifying the noise sources with the most noise contributions through simulations at different frequency offsets is important because it eases the equation-based prediction by considering a smaller number of sources for simpler calculations. Parameters like k_f, v_{ov}, and $|V_1|$ were extracted from SpectreRF simulations and used in the noise equations.

Fig. 2.19 shows measured phase noise of - 65 dBc/Hz and -72 dBc/Hz at 1 kHz offset from 175.83 and 178.23 MHz carriers, respectively. The phase noise performance was achieved with a dc power consumption of 72 μW. However, the VCMO can work with only 29 μW for the lower end of the tuning range. It is worth mentioning that with only 29 μW, the control signal set to 11111111, and the varactor voltage set to 1.2 V, the VCMO achieves a phase noise of -73 dBc/Hz at 1 kHz offset from a 175.9 MHz carrier and -139 dBc/Hz noise floor. The enhancement in the close-in phase noise is attributed to the lower gain settings. A lower output amplitude for the 29 μW setting resulted in a worse phase noise floor. As shown in Fig. 2.19, the phase noise was reasonably maintained over the tuning range. The measured profile matches well with the theory presented earlier. Comparing the phase noise performance of 175.83 MHz to 178.23 MHz carrier, the phase noise floor at the lower frequency is better due to the larger available output swing. Regarding the close-in profile, lower gain settings and higher loaded Q at higher frequency operation proved to provide better close-in noise in comparison to the 175.83 MHz case.

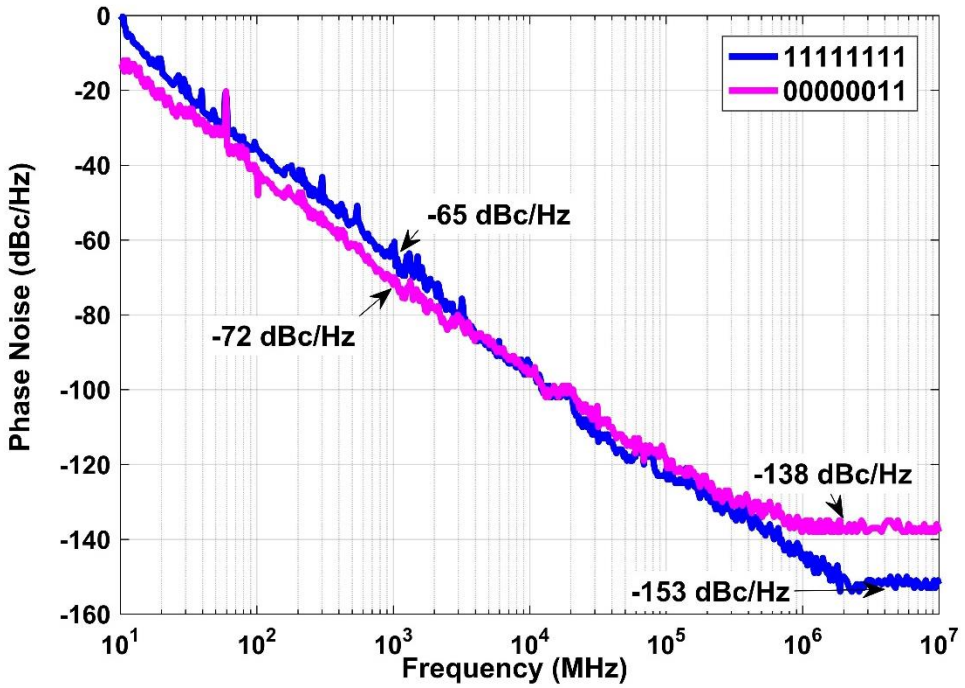

Fig. 2.19. Measured phase noise spectrum for 175.83 MHz (control signal: 11111111, varactor voltage= 1.2 V) and 178.23 MHz (control signal: 00000011, varactor voltage= 0 V) carriers [11].

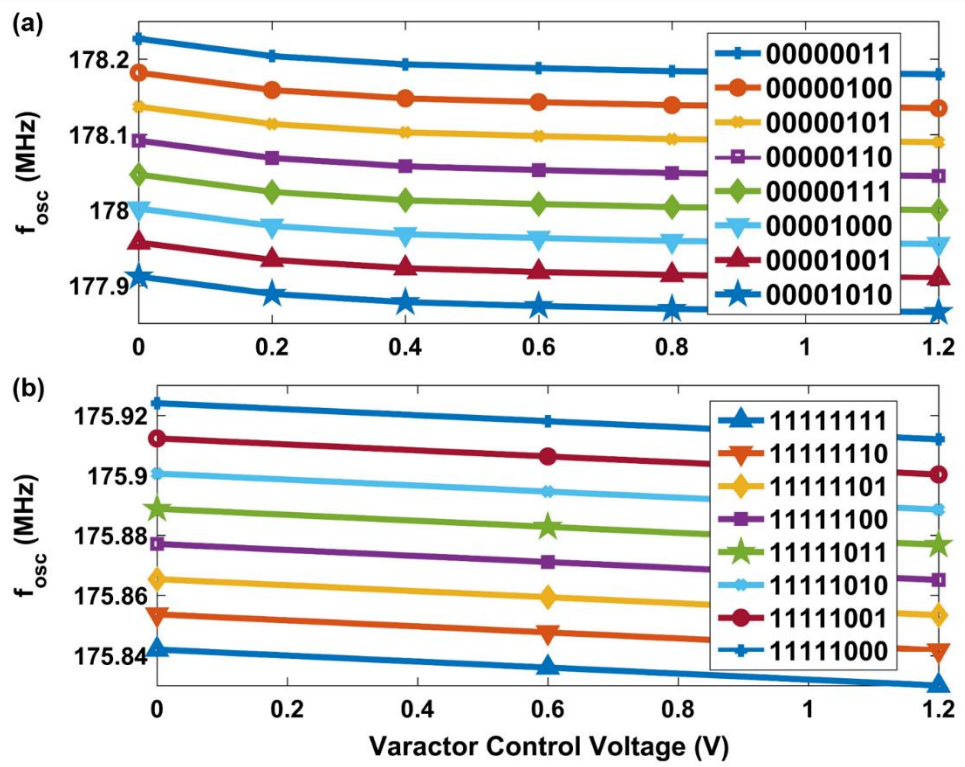

Fig. 2.20. (a) Upper 8 frequency bands. (b) Lower 8 frequency bands [11].

The VCMO demonstrated a tuning range of 2.4 MHz, and thus a 1.4% fractional tuning range. The measured tuning curves are shown in Fig. 2.20 with no dead zones. The effects of the non-linearity in the varactor and the parasitic capacitance of the bank appear mostly at the high end of the tuning range where the 8-bit capacitor bank is in an off state. At lower frequencies, the nonlinearities are much less pronounced, and the varactor tuning range is smaller by a factor of 4 as the varactor small capacitance is swamped by the large capacitance of the capacitor bank in its on-state. Currently, the tuning range is mainly limited by the circuit design and not by the MEMS resonator. The tuning range can be further enhanced by increasing the power consumption of the VCMO for the same resonator, thereby harnessing most of the available bandwidth of the resonator (8.6 MHz). Future circuit optimization for $LiNbO_3$ MEMS resonators will also give better phase noise and tuning range performances simultaneously. The VCMO performance, in comparison to the-state-of-the-art MEMS resonator-enabled VCOs, is summarized in Table 2.1.

2.5 SUMMARY AND CONCLUSION

The chapter presents a comprehensive guide to co-design piezoelectric RF-MEMS resonators and CMOS for enabling VCMOs that harness the best benefits of both platforms, hence enabling the design of tunable low-power high *Q* VCMOs. The analysis herein is applicable to any kind of piezoelectric resonators but specific for Colpitts VCMOs. As the experiments validate our analysis, this dissertation has demonstrated the first VCMO based on a $LiNbO_3$ LVR resonator and CMOS. The phase noise of the VCMO is measured to be -72 dBc/Hz at 1 kHz offset from a

178.23 MHz carrier. A tuning range of 2.4 MHz (~1.4%) has been demonstrated with a maximum dc power consumption of 72 μW. The reported VCMO has one of the highest FoMs (202.3 dB at 1 MHz) and the highest FoM^T (185 dB at 1 MHz) among the MEMS based VCOs found in the literature.

Table 2.1 VCMO Performance Summary and Comparison

Ref.	MEMS Tech.	Circuit Tech.	Freq. (MHz)	Tuning Range			dc Power (mW)	Phase Noise (dBc/Hz)			FoM	FoM^T
											(dB)	
				(ppm)	(MHz)	%		1 kHz offset		1 MHz offset	1 MHz offset	
This work [11]	**$LiNbO_3$ LVR**	**65 nm CMOS**	**175.83.178.23**	**13650**	**2.4**	**1.37**	**0.072**	**-72 @178.23 MHz carrier**		**-146 @175.83 MHz carrier**	**202.3**	**185**
[37]	AlN CMR	65 nm CMOS	204	611	0.125	0.06	0.047	-77	-78.2*	-120	179.5	130
[38]	AlN CMR	0.5 μm CMOS	1500	1500	2.25	0.15	6.9	-45	-63.5*	-151	206.1	169.7
[39]	AlN-on-Si LBAR	0.18 μm CMOS	427	810	0.35	0.08	13	-82	-89.6*	-147	188.5	146.5
[31]	FBAR	0.25 μm BiCMOS	2100	-	37	1.8	58.32	-	-	-144	193	177.9
[32]	Coupled FBAR	0.13 μm CMOS	1550	28000	43.4	2.8	7.9	-56.3	-74.8*	-140.5	195.5	184.2
[98]	FBAR	Bipolar	2000	-	2.5	0.13	115.5	-	-	-150	195	157.7
[59]	$LiNbO_3$ LVR	Discrete	150	2800	0.42	0.28	5	-84.4	-83*	-146	182.5	151.5
[99]	FBAR	90 nm CMOS	1705.9	-	6.4	0.38	1.5	-	-	-	-	-

*Normalized to 178 MHz.

CHAPTER 3: A WIDEBAND OSCILLATOR EXPLOITING MULTIPLE RESONANCES IN LITHIUM NIOBITE MEMS RESONATOR

3.1 INTRODUCTION

This chapter focuses on our second project, direct RF synthesis based on wideband multi resonances VCMOs. This chapter presents a comprehensive guide to co-design $LiNbO_3$ LOBARs and VCOs using discrete components on a printed circuit board (PCB). The analysis focuses on understanding the oscillator-level tradeoffs between the number of locked tones, frequency stability, tuning range, power consumption, and phase noise. Moreover, the chapter focuses on understanding the relationship between the above specifications and the different LOBAR parameters such as k_t^2, Q, transducer design and the resonator size. As a result of this study, a VCMO based on $LiNbO_3$ LOBAR is demonstrated. The LOBAR excites over 30 resonant modes in the range of 100 to 800 MHz with a frequency spacing of 20 MHz. The VCMO consists of a LOBAR in a closed-loop with two amplification stages and a varactor-embedded tunable LC tank. By adjusting the bias voltage applied to the varactor, the tank can be tuned to change

the closed-loop gain and phase responses of the oscillator so that the Barkhausen conditions are satisfied for a particular resonant mode. The tank is designed to allow the proposed VCMO to lock to any of the ten overtones ranging from 300 to 500 MHz. These ten tones are characterized by average Qs of 2100, k_t^2 of 1.5%, FoM_{RES} of 31.5 enabling low phase noise, and low-power oscillators crucial for IoT. Owing to the high Qs of the $LiNbO_3$ LOBAR, the measured VCMO shows a close-in phase noise of -100 dBc/Hz at 1 kHz offset from a 300 MHz carrier and a noise floor of -153 dBc/Hz while consuming 9 mW [12]. With further optimization, this VCMO can lead to direct RF synthesis for ultralow-power transceivers in multi-mode IoT nodes.

The rest of the chapter is organized as follows: Section 3.2 discusses the design of a $LiNbO_3$ LOBAR in the context of using it later to implement a wideband VCMO enabling direct RF synthesis for multi-mode IoT applications. Section 3.3 then focuses on the design and simulated performance of our VCMO. Different design tradeoffs between the number of locked tones, frequency stability, tuning range, power consumption, and phase noise will be discussed. Moreover, the study will focus on understanding the relationship between the oscillator specifications and the different LOBAR parameters such as k_t^2, Q, transducer design and the resonator size. Section 3.4 reports on the oscillator measurement results. Finally, Section 3.5 concludes the chapter.

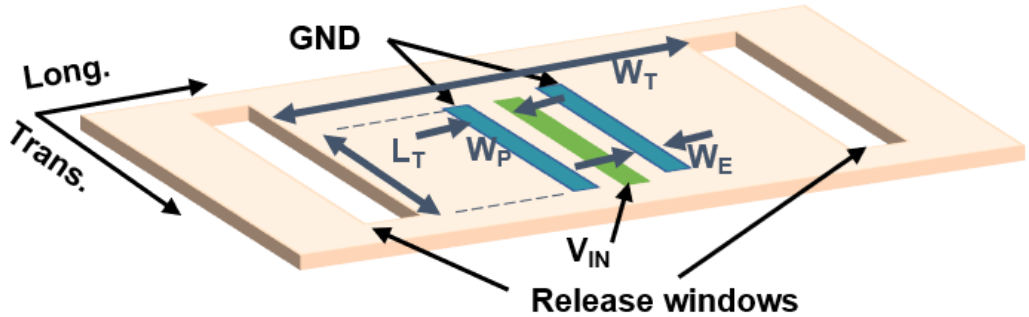

Fig. 3.1. Schematic of a LOBAR [12].

3.2 LITHIUM NIOBATE LOBARS

3.2.1 Overview

As shown in Fig 3.1, the LOBAR consists of aluminum IDEs partially covering the top surface of a suspended $LiNbO_3$ thin-film. The resonator width (W_T) is significantly larger than the electrodes (W_E) and the gap widths (W_G) needed for the overmode operation. The orientation of the device is chosen as −10° to the +Y-axis in the X-cut plane of $LiNbO_3$ for exciting a family of SH modes of various lateral mode orders characterized by high k_t^2 [52]. Key dimensional parameters of a typical LOBAR using two transducers (three IDEs) are shown in Fig. 3.1.

In contrast to a conventional resonator targeting the excitation of a single resonant mode, LOBARs excite several equally-spaced resonances simultaneously. These modes are principally the eigenmodes of the resonant cavity. Assuming a small ratio of the film thickness (h) to the acoustic wavelength (λ) for the frequency range of interest, the frequencies of different resonant modes (f_n) can be approximated by:

$$f_n = \frac{n\, v_{SH0}}{2\, W_T} \tag{3.1}$$

where f_n is the resonant frequency of the nth-order mode, v_{SH0} is the SH0 mode phase velocity.

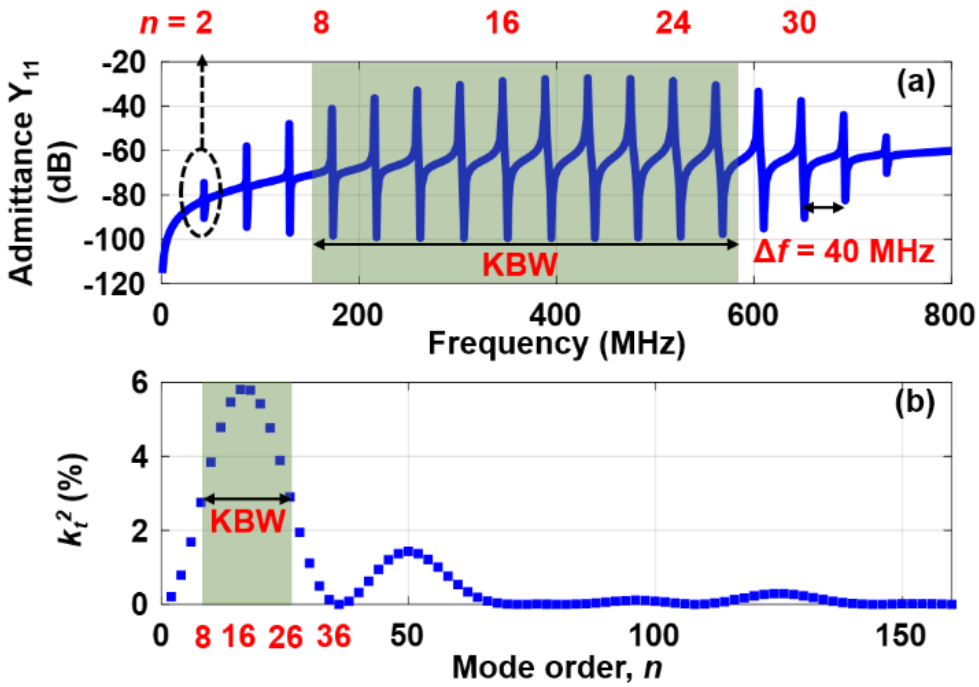

Fig. 3.2. Simulated response of a two-transducer LOBAR using the model demonstrated in [73]. (a) admittance response. (b) k_t^2. Parameters used in the simulation: W_T = 100 µm, W_E = W_G = 2.5 µm, C_o = 180 fF, Q = 2000 for all tones [12].

Based on the simplified model demonstrated in [77], the LOBAR characteristics are shown in Fig. 3.2. For resonances further away from the center frequency (f_{center}), the modes are less excited, hence a reduced k_t^2. This is because the transducer cannot uniformly couple energy to all the modes. It couples energy most efficiently to a mode (n) that corresponds to the center frequency (f_{center}) of the resonator. f_{center} is set by the transducer pitch (W_P) as:

$$f_{center} = \frac{v_{SH0}}{2\,W_P} \tag{3.2}$$

The resonant mode is most effectively excited when the $W_P = \lambda/2$. The coupling decreases when the W_P and the λ mismatch and becomes zero when the $W_P = \lambda$ due to the full cancellation of mutual energy. The third specification is the electromechanical coupling bandwidth (KBW) of the resonator, defined as the frequency range where various modes are excited with no less than half of the k_t^2 at f_{center}. The fourth specification of the LOBAR is the frequency spacing (Δf) between adjacent tones which can be expressed as:

$$\Delta f = \frac{v_{SH0}}{W_T} \tag{3.3}$$

Apart from the frequency-related specifications mentioned above, the device static capacitance C_o, Q, and k_t^2 of each tone are the most important specifications for building oscillators. C_o is mostly set by the IDE dimensions, the thickness of the resonator, and the materials used. The static capacitance identifies the minimum power consumption of the VCMO as will be seen later in the chapter. Q, affecting the phase noise of the VCMO, is collectively determined by various loss mechanisms originating from the materials stack and the design. Finally, the k_t^2 distribution among different tones is modeled and shown in Fig. 3.2(b). The figure shows an excitation of 17 tones ranging from 100 to 800 MHz with a spacing of 40 MHz. The tones are centered around 400 MHz (mode order 16). This mode has the highest k_t^2 of ~6% among the 17 modes. Only 10 tones (mode orders 8 to 26) lie within the KBW of the resonator (the green shaded area). The first lobe in Fig. 3.2(b) covers mode orders from 2 to 36, corresponding to the resonances from 100 to 800 MHz in Fig. 3.2(a).

The next subsection focuses on optimizing the three main design parameters, namely W_T, W_P, and the number of transducers (N_T). These parameters set the resonator specifications f_n, Δf, f_{center}, KBW, and k_t^2; which will finally determine the VCMO tuning range and the number of RF carriers generated at the output of the VCMO. The fabricated device performance will be presented in Section 3.2.3

3.2.2 Design Space

Investigating the design space of the LOBAR is an important step towards building the VCMO. This space can be quantified through capturing the effect of varying the main resonator parameters on the admittance profile as shown in Figs. 3.3 - 3.6. By varying W_T while fixing W_P = 5 μm, C_o = 180 fF, and Q = 2000, the frequency spacing (Δf) can be controlled while fixing the center frequency (f_{center}) to 400 MHz as shown in Fig. 3.3. Δf and k_t^2 almost get halved by doubling W_T. A smaller Δf ideally results in a wider tuning range for the VCMO, however the ability of the oscillator to lock to a certain tone and suppress others decreases. A smaller k_t^2 as a result of a larger resonator width will increase the VCMO power consumption as shown in Fig. 3.3 (e), where the real portion of the admittance ($1/R_m$) at different f_n is plotted versus the mode orders for different W_T values. Moreover, the resonator KBW increases with increasing W_T at the expense of a smaller k_t^2. In summary, a larger resonator width translates to a wider tuning range, lower locking stability, and higher power consumption.

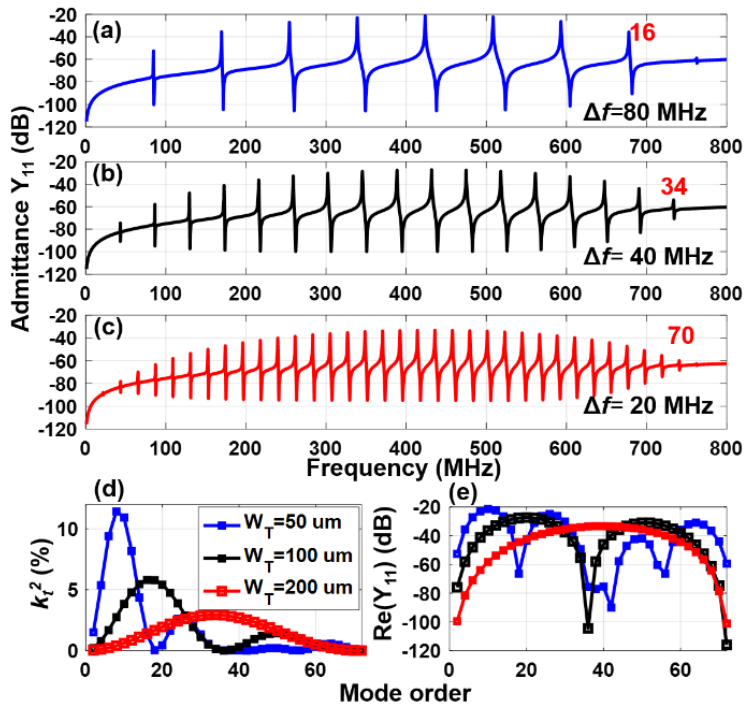

Fig. 3.3. Admittance of the LOBAR with (a) W_T = 50 μm, (b) W_T = 100 μm, and (c) W_T = 200 μm. (d) k_t^2 and (e) $1/R_m$ of LOBAR with W_T = 50, 100 and 200 μm. $W_E = W_G$ = 2.5 μm, C_o = 180 fF, and Q = 2000 values are used in these simulations [12].

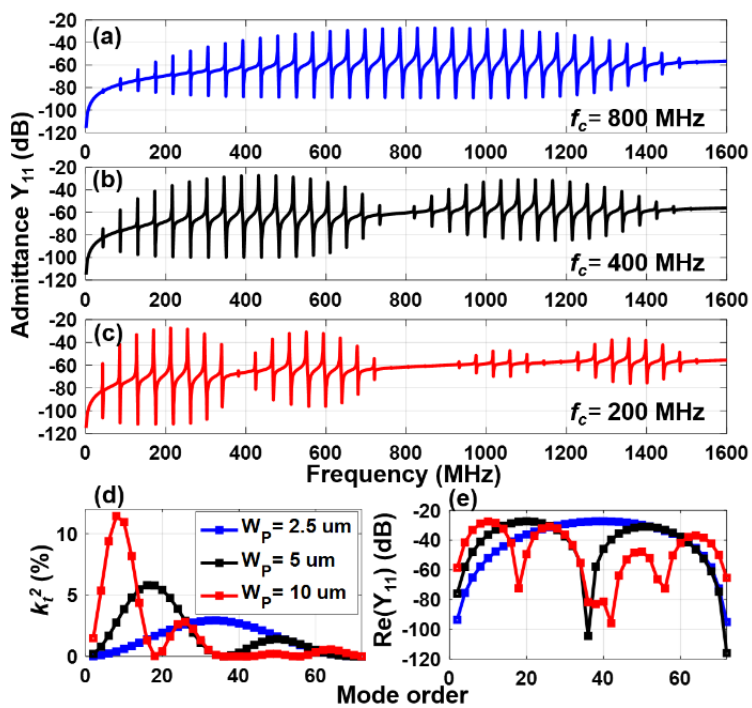

Fig. 3.4. Admittance of the LOBAR with (a) W_P = 2.5 μm, (b) W_P = 5 μm, and (c) W_P = 10 μm. (d) k_t^2 and (e) $1/R_m$ of LOBAR with W_P = 2.5, 5 and 10 μm. W_T = 100 μm, C_o = 180 fF, and Q = 2000 values are used in these simulations [12].

On the other hand, by varying W_P while fixing W_T = 100 μm, C_o =180 fF, and Q = 2000, f_{center} can be controlled while fixing Δf to 40 MHz as shown in Fig. 3.4. f_{center} gets halved while k_t^2 almost double via doubling W_T. A smaller f_{center} results in a smaller frequency of oscillation. A larger k_t^2 as a result of a larger resonator pitch will result in a reduction in the VCMO power consumption as shown in Fig. 3.4(e), where $1/R_m$ is plotted versus the mode orders for different W_P values. Moreover, the resonator KBW and hence the VCMO tuning range decrease with increasing W_T. To summarize, a larger resonator pitch translates to a lower oscillation frequency, a small tuning range, and less power consumption.

Following the RF synthesizer requirements, the VCMO should lock to at least 10 overtones centered around 400 MHz with a tuning range of at least 200 MHz. These numbers translate to a Δf of 20 MHz and f_{center} of 400 MHz. Hence, the LOBAR should have a KBW greater than 200 MHz exciting the resonant modes characterized by the highest k_t^2 spanning between 300 and 500 MHz. According to the above specifications, and equations (3.1) - (3.3), W_T is set to 200 μm and W_P to 5 μm. The number of transducers (N_T) must be determined as the next design step to complete the LOBAR design.

Figs. 3.5 and 3.6 show the effect of N_T (N_T = no. of IDEs-1) on the resonator performance. According to [77], even and odd-order modes cannot be excited simultaneously in a resonator cavity with centered transducers. Only even-order modes can be excited with even numbers of centered transducers while only odd-order modes can be excited with odd numbers of centered transducers. A detailed

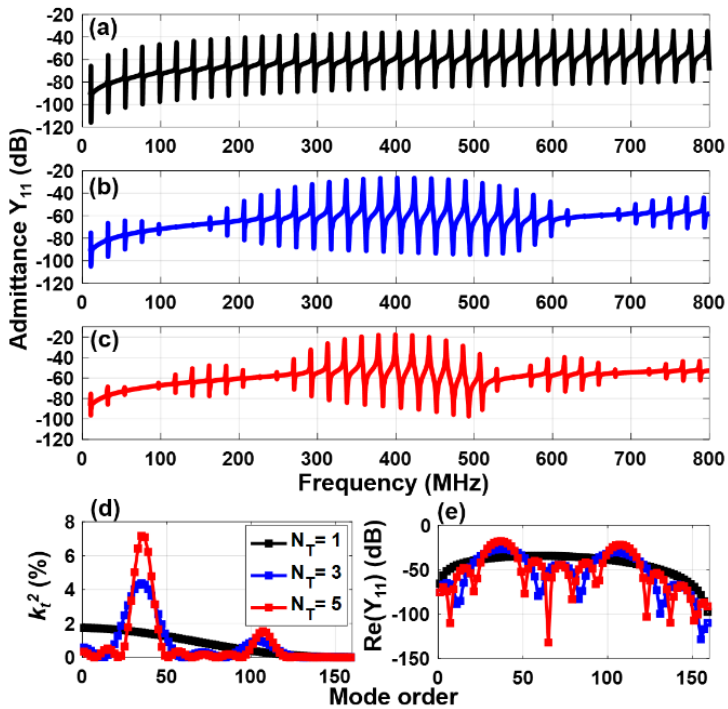

Fig. 3.5. Admittance of the LOBAR with (a) $N_T = 1$, (b) $N_T = 3$, and (c) $N_T = 5$. (d) k_t^2 and (e) $1/R_m$ of LOBAR with $N_T = 1$, 3 and 5. $W_T = 200\ \mu$m, $W_P = 5\ \mu$m, and $Q = 2000$ are used in these simulations [12].

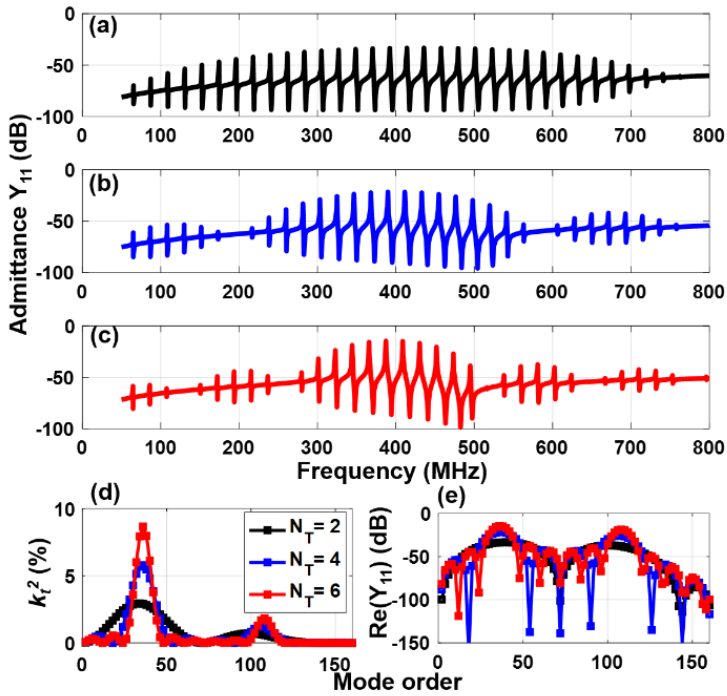

Fig. 3.6. Admittance of the LOBAR with (a) $N_T = 2$, (b) $N_T = 4$, and (c) $N_T = 6$. (d) k_t^2 and (e) $1/R_m$ of LOBAR with $N_T = 2$, 4 and 6. $W_T = 200\ \mu$m, $W_P = 5\ \mu$m, and $Q = 2000$ are used in these simulations [12].

study on offsetting the transducers from the center of the resonator can be found in [77], which will allow excitation of both the odd and even order modes. In this dissertation, the focus is on LOBARs with IDTs centered on the resonator cavity. Although N_T has no primary effect on setting f_{center} or Δf, its effect on the KBW and k_t^2 should be considered. A larger N_T translates to a higher maximum k_t^2 and a smaller KBW. Hence lower power consumption and smaller tuning range for VCMOs, respectively. Moreover, larger N_T translates to lower Q due to the increase of the metal-piezo losses. For a single transducer design, the low-pass behavior seen in Fig. 3.5(d) rejects signals at higher frequencies, which is not desirable for tunable RF VCMOs where the tuning range is usually specified around a certain carrier. Moreover, Fig. 3.5(e) shows a much higher R_m for a single IDT when compared to 3 or 5 IDTs thus higher power consumption. Finally, after considering the above tradeoffs, N_T of 2 is chosen in this work to achieve a maximum Q (hence, best close-in phase noise on the circuit level) and maximum tuning range at the expense of slightly higher power consumption.

The LOBAR is modeled inside in the VCMO circuitry using the MBVD model. The model has only one static branch realized by C_o in parallel to 10 motional branches instead of 10 static branches if those 10 modes are to be realized through ten conventional resonators, each targeting a single mode.

3.2.3 Fabricated LOBAR

Fig. 3.7(a) shows the measured and MBVD fitted responses of the fabricated LOBAR. The LOBAR has the following parameters: $W_T = 200$ μm, $W_P = 5$ μm, $N_T = 2$, and $C_o = 125$ fF. The main specs (f_n, Q, k_t^2, FoM, and R_m) of the

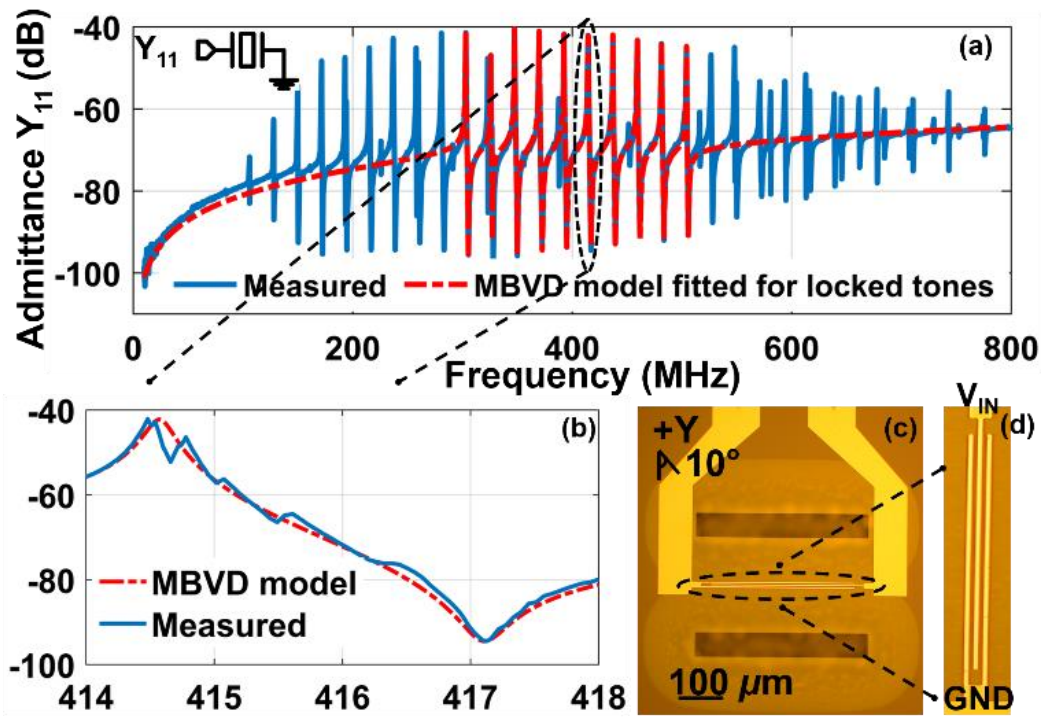

Fig. 3.7. (a) Measured and MBVD fitted responses of the LOBAR. (b) Measurement of the 415 MHz resonance. (c) Optical image of the LOBAR. (d) Zoomed-in picture of the LOBAR [12].

Table 3.1 Extracted Parameters of the Ten Overtones in 300 – 500 MHz Range

Spec/Mode	1	2	3	4	5	6	7	8	9	10
f_n (MHz)	305	325	345	370	390	415	435	460	480	505
Q	1650	1671	1945	1825	1908	1970	2608	2050	2202	3000
k_t^2 (%)	2.56	1.29	2.19	2.02	1.69	1.48	1.09	1.13	0.89	0.59
FoM	42.3	21.6	42.63	36.9	32.2	29.2	28.4	23.2	19.6	17.7
R_m (Ω)	122	225	107	115	125	130	127	147	167	175
C_o (fF)	125									

LOBAR for the ten locked overtones spanning from 300 to 500 MHz are given in Table 3.1. As a zoomed-in example, the measured admittance of the 415 MHz resonance is shown in Fig. 3.7(b), while the optical image of the device is shown in Fig. 3.7(c). The device uses the same fabrication process reported in [100]. The resonator was fabricated using a transferred $LiNbO_3$ thin-film on a Si carrier substrate. The resonator is composed of an 800 nm $LiNbO_3$ thin-film with 250 nm

Al electrodes on top. Average Qs of 2100, k_t^2 of 1.5%, FoM_{RES} of 31.5, and R_m of 140 help in enabling low phase noise, low-power oscillators that are crucial for IoT.

In comparison to switching between lithographically defined multiple resonators, our LOBAR saves area by packing over 30 resonances in a single device rather than using 30 standalone resonators. Moreover, LOBARs usually have higher Q at the same frequency when compared to the conventional single-mode resonators due to the lower metallization ratio, thus improving the close-in phase noise performance.

3.3 RECONFIGURABLE OSCILLATOR

In this section, we first introduce the VCMO schematic and the optimization of phase noise, tuning range, and power consumption. Then, RF measurements on the $LiNbO_3$ LOBAR VCMO are presented. The VCMO is designed with the capability to lock to the maximum number of LOBAR tones centered around f_{center} (~ 400 MHz).

3.3.1 Overview

The oscillator in Fig. 3.8(a) consists of a LOBAR in a closed-loop with two common-emitter degenerated amplifiers and a voltage tunable varactor-embedded LC resonator. Each of these blocks has a function inside the loop, the LOBAR excites the different tones, while the amplifier provides enough gain to start and sustain the oscillation, and the LC tank selects a certain overtone and suppresses others. The tunable LC tank is comprised of an inductor and a varactor in parallel,

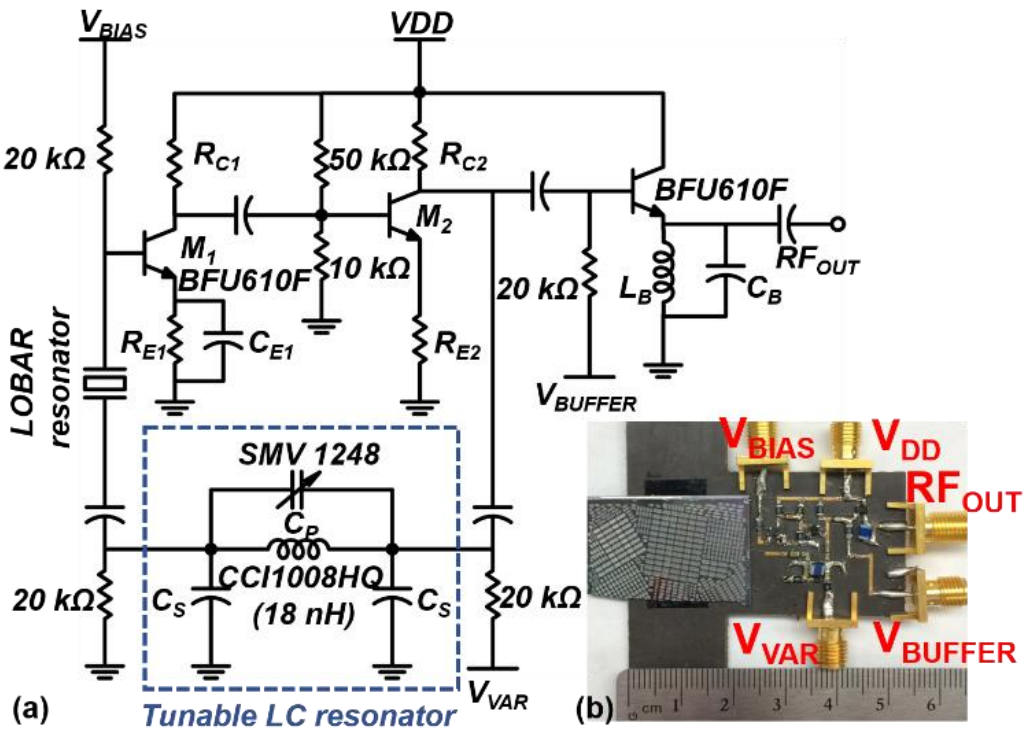

Fig. 3.8. (a) VCMO circuit schematic. (b) Board implementation [12].

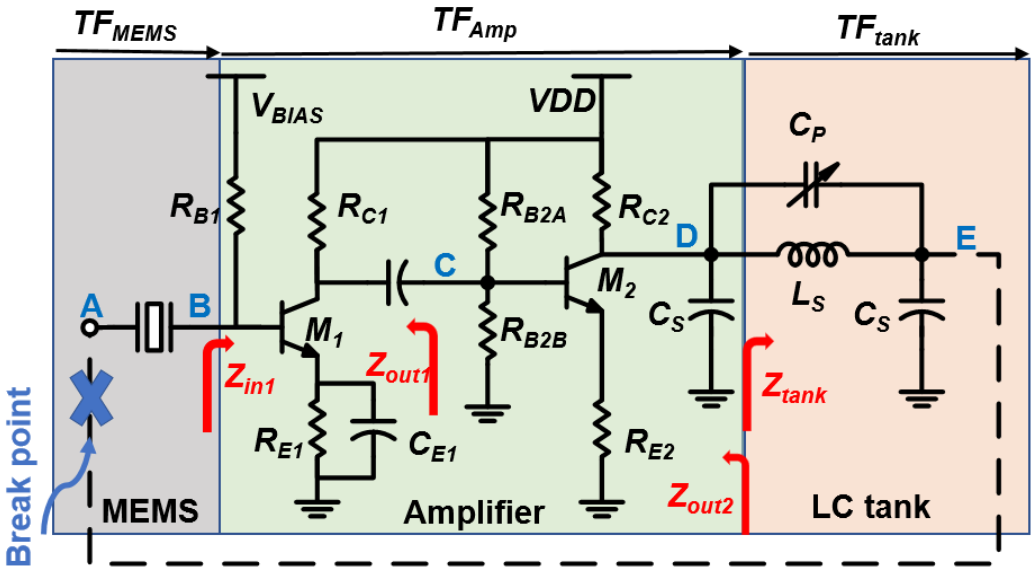

Fig. 3.9. Breaking the loop at point A. The figure also shows the three main components of our VCMO [12].

loaded by two shunt capacitors C_s to the ground. By tuning the bias voltage V_{VAR} of the varactor C_p, the LC tank adjusts the loop so that the Barkhausen conditions can

be satisfied for an acoustic resonant mode excited via the LOBAR. Hence, only one oscillation frequency (f_o) is produced at the output guaranteeing a stable oscillation. A common collector buffer is used to match the output to 50 Ω needed for the measurements. The following subsections will focus on the design and analysis of the LOBAR VCMO; several specifications will be considered in our analysis such as tuning range, power consumption, and phase noise.

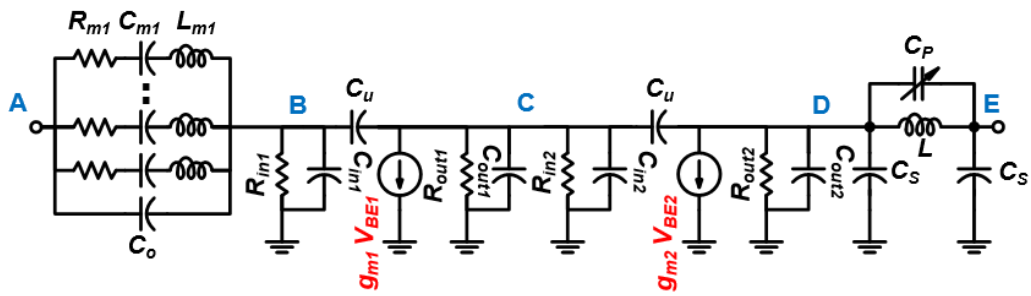

Fig. 3.10. Small-signal model of the VCMO [12].

3.3.2 Transfer Functions

To fully understand the VCMO, several transfer functions (*TFs*) are developed. These functions characterize the gain or the loss of the circuit. To this end, we will divide the oscillator loop into three segments as shown in Fig. 3.9 and derive the *TF* for each segment. We break the loop at Point *A* shown in Fig. 3.9 while paying attention to the loading of the circuitry.

3.3.2.1 Amplifier

The two degenerated common-emitter stages have a combined gain of TF_{Amp} which is defined as the voltage at node *D* divided by the voltage at node *B* as shown in Fig. 3.9. TF_{Amp} is derived as below:

$$TF_{Amp} = TF_{Amp1}\, TF_{Amp2} = G_{m1} Z_{out1} G_{m2} Z_{out2} \tag{3.4}$$

where G_{m1} and G_{m2} are the degenerated transconductances of the first and second stages, Z_{out1} and Z_{out2} are the output impedances of the first and second stages. They are given below as functions of the small-signal circuit parameters shown in Fig. 3.10.

$$G_{m1} = \left(\frac{g_{m1}}{1 + \left| \frac{g_{m1} R_{E1}}{1 + sR_{E1} C_{E1}} \right|} \right) \tag{3.5}$$

$$Z_{out1} = \left(\frac{R_{out1} || R_{in2}}{1 + s(R_{out1} || R_{in2})(C_{out1} + C_{in2})} \right) \tag{3.6}$$

$$G_{m2} = \left(\frac{g_{m2}}{1 + g_{m2} R_{E2}} \right) \tag{3.7}$$

$$Z_{out2} = \left(\frac{R_{out2}}{1 + sR_{out2}(C_{out2} + C_S)} \right) || \, Z_{tank} \tag{3.8}$$

where $C_{out1} = C_{o1} + C_{\mu}$, and $C_{in2} = C_{i2} + C_{\mu}\,(1 + g_{m2}\, R_{out2})$. C_{o1} is the parasitic capacitance at the collector of M1, C_{i2} is the parasitic capacitance at the base of M2, and C_{μ} is the parasitic capacitance between the base and collector of M1 or M2. $s = j\omega$, $g_{m1} = I_{C1}/(KT/q)$. R_{out1} is given as:

$$R_{out1} = R_{C1} || [R_{x1} + r_{o1}(1 + g_{m1} R_{x1})] \tag{3.9}$$

$$R_{x1} = R_{E1} || (r_{\pi 1} + r_b) \tag{3.10}$$

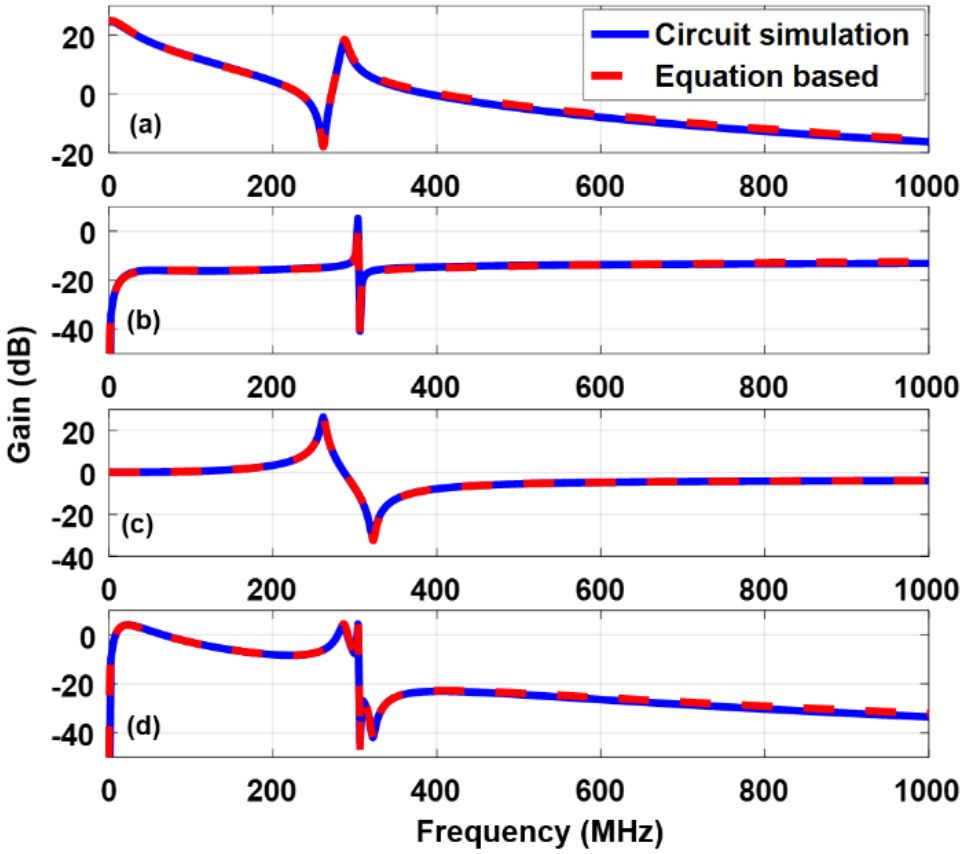

Fig. 3.11. Circuit simulations and equation-based transfer functions of different components in the VCMO. (a) TF_{Amp}, (b) TF_{MEMS}, (c) TF_{tank}, and (d) TF_{loop}. Equations and simulations match perfectly. Parameters used in these simulations: g_{m1} = 11.9 mS, g_{m2} = 6.4 mS, R_{out} = 1.98 kΩ, R_{out2} = 510 Ω, R_{in1} = 10 kΩ, R_{in2} = 7 kΩ, R_m = 122 Ω, C_m = 2.6 fF, L_m = 106.05 μH, C_s = 7 pF, and C_p = 13.5 pF. Only one LOBAR overtone (300 MHz) is shown in the plot for figure clarity [12].

$$R_{in2} = R_{B2}||\left(r_{\pi 2} + r_b + \frac{R_{E2}(1+\beta_o)\left(r_{o2} + \frac{R_{C2}}{1+\beta_o}\right)}{r_{o2} + R_{C2} + R_{E2}}\right) \tag{3.11}$$

$$Z_{tank} = \left(\frac{r_s + sL}{1 + s\, r_s C_P + s^2 L C_P}\right) + \frac{1}{sC_s} \tag{3.12}$$

where $R_{B2} = R_{B2A}||R_{B2B}$, $r_{\pi 1} = \beta_o/g_{m1}$, r_{o2} = *early voltage*/I_{C2}, r_b is the base series resistance, and β_o is the small-signal current gain. $r_s = \omega L/Q_{tank}$, L is the tank inductance, Q_{tank} is the tank coil quality factor, C_p is the tank varactor, and C_s is the tank capacitive load. R_{out2} equation is the same as R_{out1} but using subscript 2 instead

of 1. The same goes for $r_{\pi 2}$, R_{in2} and C_{out2}. Equation (3.4) is shown along with a circuit simulation in Fig. 3.11(a). The equation matches perfectly the circuit simulations.

For the amplifier, the design aims to provide enough loop gain TF_{Amp} to satisfy the Barkhausen conditions with minimum noise added to the loop and lowest power consumption. Silicon germanium BFU610F is chosen as the transistors for its low noise figure and low power consumption. V_{BE} bias voltages of M1 and M2 are chosen based on three factors: first, a small BJT base current (I_B) that gives a low flicker noise; second, a reasonable gain for a single resonance without satisfying Barkhausen conditions for any other tones, especially when the tones are very close with a Δf of 20 MHz; third, low power consumption. The buffer design is borrowed from the millimeter-wave regime, where the VCO buffers use a quarter wavelength stub to cancel the imaginary output impedance and match the real output impedance ($1/g_m$) of the buffer emitter to 50 Ω. For lower frequency designs, an LC tank can be used to have the same effect as the stub. The tank reduces the power consumption in the buffer for the same output power when compared to a resistive loading.

3.3.2.2 LOBAR

The LOBAR admittance profile and MBVD model are presented in the previous section. Z_{MEMS} derived in (1.7) is the voltage across the resonator divided by the current through it. Here we define $TF_{MEMS} = V_B/V_A$, taking into consideration the loading of the amplifier on the LOBAR. TF_{MEMS} is shown in Fig. 3.11(b) for only the 300 MHz tone and is given as:

$$TF_{MEMS} = \frac{Z_{in1}}{Z_{in1} + Z_{MEMS}} \tag{3.13}$$

where Z_{in1} is given as:

$$Z_{in1} = \left(\frac{R_{in1}}{1 + sR_{in1}C_{i1}}\right) || \left(\frac{\frac{R_{out1}}{1 + sR_{out1}C_{out1}} + \frac{1}{sc_u}}{1 + G_{m1}\frac{R_{out1}}{1 + sR_{out1}C_{out1}}}\right) \tag{3.14}$$

3.3.2.3 LC tank

A CCI1008HQ inductor of 18 nH is chosen as the tank inductor. This value allows for locking to the LOBAR resonances with the lowest R_m in the range of 300 to 500 MHz. The inductor has a minimum Q_{tank} of 62 at 350 MHz, a minimum self-resonant frequency (SRF) of 2.7 GHz, and a max DCR of 0.07 Ω. For the LC tank, $TF_{tank} = V_E/V_D$ is given below and shown in Fig. 3.11(c).

$$TF_{tank} = \frac{1}{sC_s\left(\frac{r_s + sL}{1 + s\,r_sC_P + s^2LC_P}\right) + 1} \tag{3.15}$$

As deduced from (3.15), the tank has both series (f_s^t) and parallel resonances (f_p^t). Controlling these frequencies will be discussed in the next subsection. Both frequencies are given below:

$$f_s^t = \frac{1}{2\pi\sqrt{L(C_s + C_p)}} \tag{3.16}$$

$$f_p^t = \frac{1}{2\pi\sqrt{LC_p}} \tag{3.17}$$

Finally, the loop gain TF_{loop} is shown in Fig. 3.11(d) and given as:

$$TF_{loop} = TF_{Amp}\, TF_{MEMS}\, TF_{tank} \tag{3.18}$$

where the multiplication of TF_{MEMS} and TF_{tank} will be referred to as β_{loop}. By satisfying $abs(TF_{loop}) > 1$ and solving for $Imag(TF_{loop}) = 0$, the VCMO oscillation frequency (f_o) is calculated. The parameters used to generate Fig. 3.11 are given as follows, g_{m1} = 11.9 mS, g_{m2} = 6.4 mS, R_{out1} = 1.98 kΩ, R_{out2} = 510 Ω, R_{in1} = 10 kΩ, R_{in2} = 7 kΩ, R_m = 122 Ω, C_m =2.6 fF, L_m = 106.05 μH, C_s= 7 pF, and C_p=13.5 pF. The equations for different *TF*s are derived in equations (3.4) - (3.18); these *TF*s will serve as an introduction to fully explore the design space of the VCMO analytically in the next subsection.

3.3.3 Locking Mechanism

Design choices related to the LC tank such as C_s, C_p, and Q_{tank}, and others related to the LOBAR such as k_t^2, and C_o, need to be investigated. The effects of C_s and C_p on the tank transfer function are shown in Fig. 3.12. C_s controls only f_s^t given in (3.16) while C_p controls both f_s^t and f_p^t given in (3.17). A smaller C_s translates to a higher f_s^t, and to smaller the tank inductive range, i.e., bandwidth (BW= f_p^t - f_s^t). Hence, affecting fewer overtones.

On the other hand, a smaller C_p translates to a larger spacing between both resonant frequencies and BW, hence affecting more overtones. Since C_s does not have control over the position of f_p^t as shown in Fig. 3.12(c) while C_p does, C_s is chosen to be fixed in the implementation and an SMV1248 varactor is chosen to

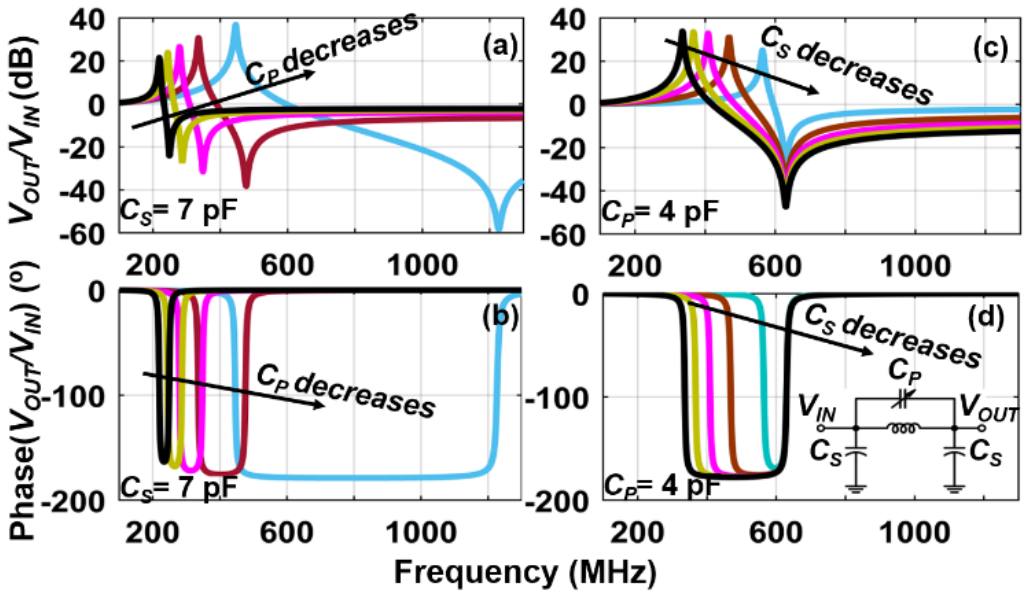

Fig. 3.12. (a) Gain and (b) phase responses with C_s fixed to 7 pF and C_p varying from 1 to 25 pF. (c) Gain and (d) phase responses with C_p fixed to 4 pF and C_s varying from 1 to 10 pF [12].

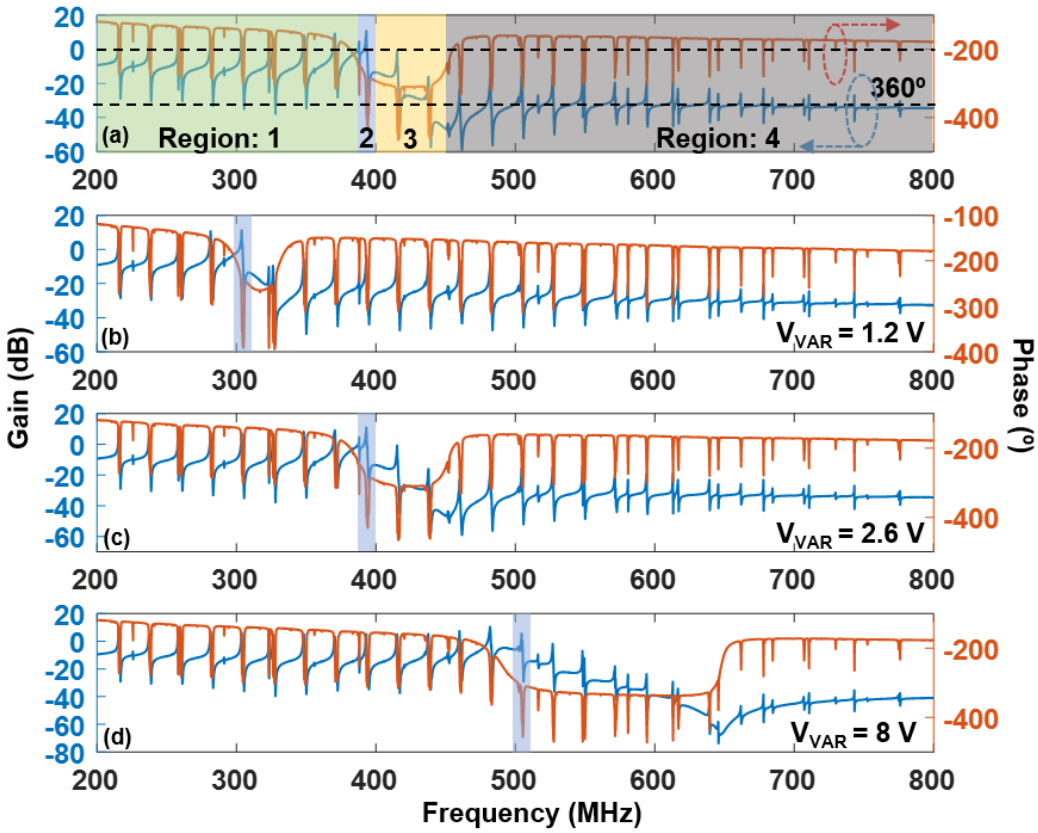

Fig. 3.13. (a) Illustration of four regions. (b) - (d) Simulated loop gain and loop phase response for three different varactor bias voltages spanning the tuning range. Only three voltages are represented instead of ten for figure clarity. The measured S-parameters of the LOBAR are used in these simulations [12].

implement C_p which can be varied from 22.62 pF to 1.3 pF as V_{VAR} varies from 0 to 8 V.

The spectrum can be divided into four regions with respect to f_s^t and f_p^t as shown in Fig. 3.13 (a). In Region 1 where frequencies are lower than f_s^t, the overtones fulfill the gain condition of oscillation but do not fulfill the phase condition. In Region 2 where the frequency aligns with f_s, the tone is coupled with a maximum gain. Furthermore, in Region 3 where frequencies lie within the tank BW closer to f_p^t, the tones get suppressed in gain despite fulfilling the phase condition. Finally, in Region 4 where frequencies are larger than f_p^t, the overtones do not fulfill both the gain and phase conditions. Therefore, the targeted LOBAR tone should be as close as possible to f_s^t inside the tank inductive region. Fig. 3.13 (b) - (d) show the simulated loop gain and phase response of the VCMO for three different varactor bias voltages spanning the tuning range.

As previously mentioned, the LC tank selects the targeted resonance to be amplified inside the oscillator, creating a stable RF carrier, and suppressing other LOBAR modes. Hence, the suppression of the nearby tones and the oscillation stability depend on the value of Q_{tank}. Moreover, the loop phase and loop gain TF_{loop} at the targeted resonance, and thus the power consumption, depend on Q_{tank}. A study showing the effect of the Q_{tank} on the TF_{loop} is shown in Fig. 3.14. A larger Q_{tank} translates to a higher loop gain for the targeted LOBAR resonance and a larger suppression of the nearby modes. For instance, one can target the 300 MHz mode by setting V_{VAR} to 1.2 V as shown in Figs. 3.14(a)-(b). As a result, TF_{loop} increases

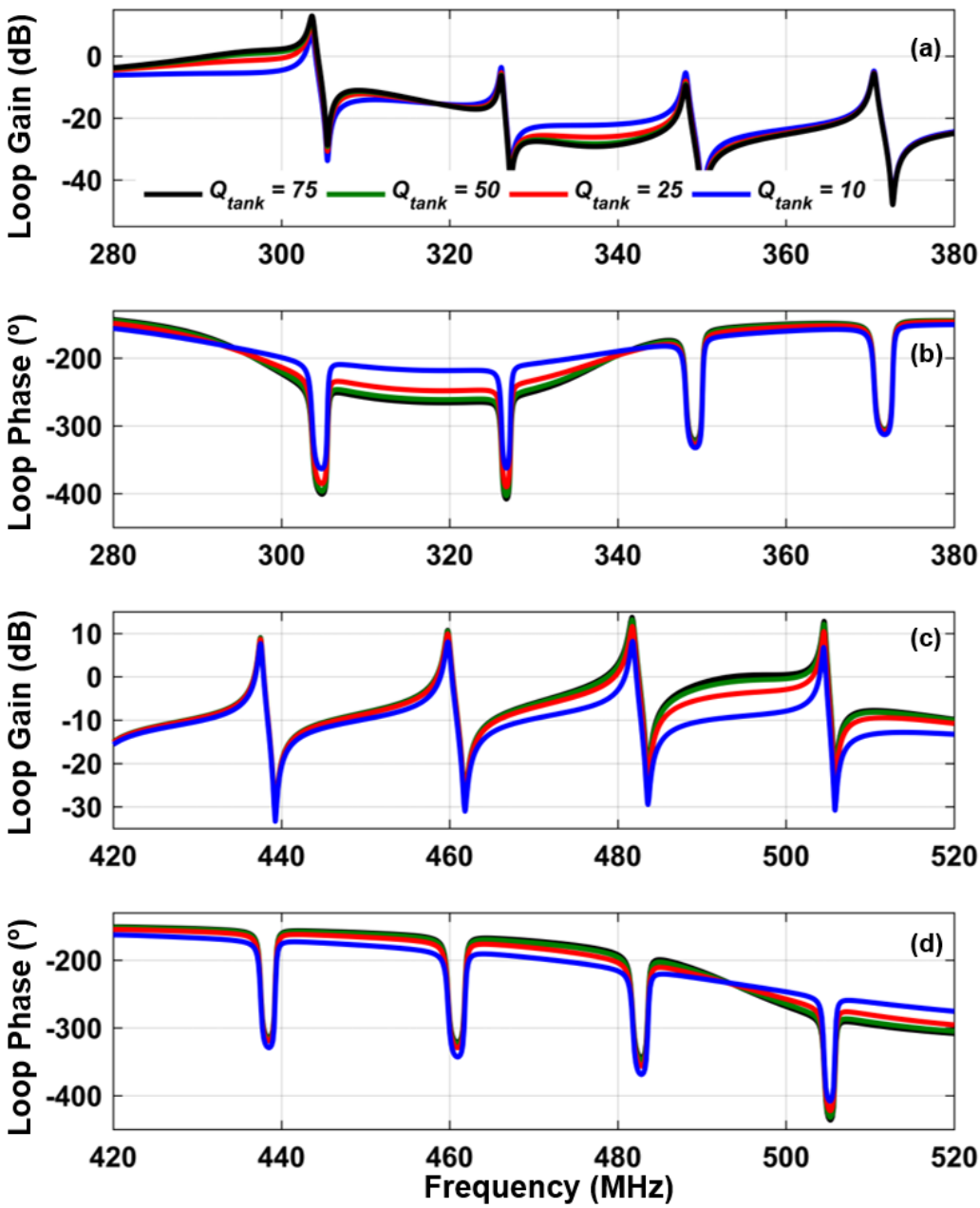

Fig. 3.14. Effect of Q_{tank} on the simulated loop gain and loop phase. (a)-(b) V_{VAR} = 1.2 V. (c)-(d) V_{VAR} = 8 V. Q_{tank} is varied from 10 to 75. The LOBAR MBVD model is used in these simulations rather than measured S-parameters for figure clarity [12].

by 5 dB and the suppression of the nearest unwanted mode ($TF_{loop|300MHz}$ - $TF_{loop|320MHz}$) increases by 7.6 dB as Q_{tank} increases from 10 to 75. Moreover, the phase dip increases by ~40° providing enough margin for phase shift and more

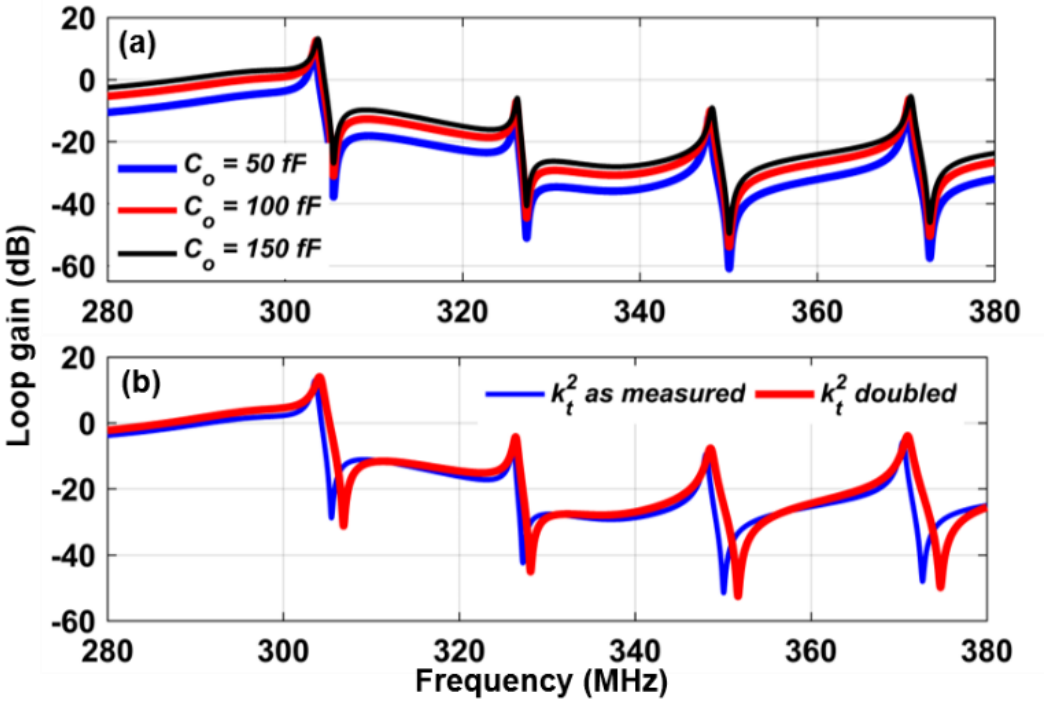

Fig. 3.15. (a) Effect of increasing C_o from 50 to 150 fF in three steps. (b) Effect of doubling k_t^2. V_{VAR} = 1.2 V [12].

stable oscillation. The 500 MHz resonance is excited by setting V_{VAR} to 8 V as shown in Figs. 3.14(c)-(d). TF_{loop} increases by 6 dB and the suppression of the nearest unwanted mode ($TF_{loop|505MHz}$ - $TF_{loop|480\ MHz}$) increases by 4.7 dB as Q_{tank} increases from 10 to 75. Moreover, the phase dip increases by ~28° at 505 MHz providing enough margin for phase shifts and more stable oscillation. A Q_{tank} below 25 permits satisfying the Barkhausen conditions of oscillation for more than one mode, thus making it undesirable for our application. For instance, a Q_{tank} of 10 increases the phase dip for the 480 MHz resonance by ~24°, consequently allowing oscillations at both the 480 MHz and 505 MHz resonances.

This Q_{tank} study also sheds some light on the applicability of implementing LOBAR VCMOs on CMOS. CMOS offers on-chip inductors with low Qs, hence

affecting the design choices of the LOBAR itself. Larger frequency spacing (Δf) between the modes might be needed for stable oscillations with CMOS. A larger Δf can be easily achieved using a smaller device width W_T as discussed previously in Section 3.2.2.

3.3.4 C_o, and k_t^2 of LOBAR

Continuing with the idea of co-designing the mechanical and electrical portions of our system, investigating the effect of C_o and k_t^2 is crucial for building the largest tuning range, lowest power consumption, and best phase noise MEMS oscillator. Revisiting Chapter 1, R_m is inversely proportional to f_s, Q, C_o, and k_t^2; while C_o is set by the size of the IDTs. Hence, both parameters heavily depend on W_T, W_P, and N_T mentioned earlier. By fixing k_t^2, f_s, and Q (through fixing W_T, W_P, and N_T) and increasing C_o (via increasing the lengths of the IDTs), the MBVD model should be adjusted by increasing C_m and decreasing both L_m and R_m with the same ratio of increasing C_o. Fig. 3.15(a) shows the effect of increasing C_o on TF_{loop}. Take the 300 MHz resonance for instance: The loop gain increases by 2 dB with increasing C_o from 50 to 150 fF as seen in Fig. 3.15(a). This is attributed to a 3 times smaller R_m. The phase dip is minimally affected by C_o variations. Larger loop gain translates to lower power consumption and better far-from-carrier phase noise.

A study on varying k_t^2 while fixing Q, f_s and C_o was also considered. Fig. 3.15(b) shows the effect of doubling k_t^2 on the loop gain. For the 300 MHz resonance, loop gain increases by 1 dB, phase dip increases by 10°, and the BW of each tone (f_p -f_s) increases by ~50% which is beneficial for fine-tuning the oscillation frequency within the BW of the tone by fine adjusting the varactor bias

V_{VAR}. Fine-tuning might be helpful to overcome environmental or temperature frequency shifts. After analyzing the effect of the LOBAR and LC tank parameters on the loop transfer functions, the next step is to analyze the phase noise of our LOBAR VCMO.

3.3.5 Phase Noise

The phase noise analysis presented in Section 1.3.1.1 is general for any oscillator. In the following subsections, we will perform phase noise analysis more specifically to our LOBAR oscillator. The goal is to find all the unknown parameters such as G_{noise} (the closed-loop noise transfer function), F, and f_c, relating the LOBAR VCMO circuit parameters and the circuit loading effects on the resonator. P_o will be treated as a given value since the oscillator output power is usually given for an oscillator.

3.3.5.1 Amplifier Noise Factor F, and Flicker Corner f_c

To find F, we start by identifying the noise sources in our VCMO. Generally, the noise sources for a MEMS oscillator can be divided into two groups: electronic and mechanical. Electronic noise sources include thermal and flicker noises of the active and passive devices used in the VCMO and these are the focus of this subsection. The low-frequency mechanical noise in the resonator originates from two sources: the nonlinearity of the micromechanical resonator, and the random low-frequency vibrations. The resonator can be driven into nonlinearity by pumping power beyond its power handling capability. Mechanical noise sources are neglected in the coming analysis as their effect on the oscillator phase noise is much lower when compared to electronic noise.

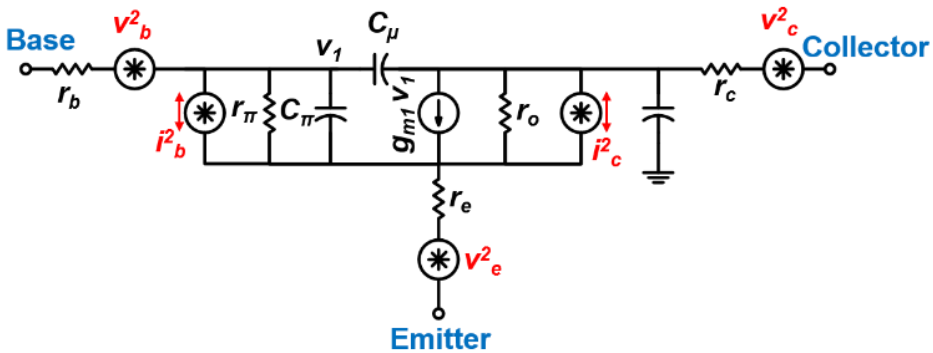

Fig. 3.16. BJT small-signal model with noise sources [12].

The main noise sources of a BJT are shown in Fig 3.16 and their *TF*s can be derived as follows for the amplifier.

$$v_{n,r_{b1}} = \sqrt{4KTr_b}\,|TF_{Amp}|$$
$$v_{n,r_{b2}} = \sqrt{4KTr_b}\,|TF_{Amp2}| \tag{3.19}$$

$$v_{n,R_{E1}} = \sqrt{4KTR_{E1}}|TF_{Amp}|$$
$$v_{n,R_{E2}} = \sqrt{4KTR_{E2}}|TF_{Amp2}| \tag{3.20}$$

$$v_{n,R_{C1}} = \sqrt{4KT\left|\frac{1}{1+sR_{C1}(C_{out1}+C_{in2})}\right|}\,|TF_{Amp2}|$$
$$v_{n,R_{C2}} = \sqrt{4KT\left|\frac{1}{1+sR_{C2}C_{out2}}\right|} \tag{3.21}$$

$$v_{n,ib_1} = \sqrt{2qi_{b1} + \left(KF\ i_{b1}{}^{AF}\ \frac{1}{f^{BF}}\right)r_b}\,|TF_{Amp}|$$
$$v_{n,ib_2} = \sqrt{2qi_{b2} + \left(KF\ i_{b2}{}^{AF}\ \frac{1}{f^{BF}}\right)r_b}\,|TF_{Amp2}| \tag{3.22}$$

$$v_{n,ic_1} = \sqrt{2qi_{c1}} \left| \frac{\left(\frac{R_{C1}}{1+g_{m1}R_{E1}}\right)}{1+s\left(\frac{R_{C1}}{1+g_{m1}R_{E1}}\right)C_{out1}} \right| \left|TF_{Amp2}\right| \tag{3.23}$$

$$v_{n,ic_2} = \sqrt{2qi_{c2}} \left| \frac{\left(\frac{R_{C2}}{1+g_{m2}R_{E2}}\right)}{1+s\left(\frac{R_{C2}}{1+g_{m2}R_{E2}}\right)C_{out2}} \right|$$

$$v_{n,A1} = \sqrt{{v_{n,r_{b1}}}^2 + {v_{n,R_{E1}}}^2 + {v_{n,R_{C1}}}^2 + {v_{n,ib_1}}^2 + {v_{n,ic_1}}^2} \tag{3.24}$$

$$v_{n,A2} = \sqrt{{v_{n,r_{b2}}}^2 + {v_{n,R_{E2}}}^2 + {v_{n,R_{C2}}}^2 + {v_{n,ib_2}}^2 + {v_{n,ic_2}}^2}$$

$$v_{n,Amp} = \sqrt{{v_{n,A1}}^2 + {v_{n,A2}}^2} \tag{3.25}$$

where v_{n,r_b}, v_{n,R_E}, and v_{n,R_C} are the thermal noises from the base, emitter and collector resistances respectively. $v_{n,ib}$, and $v_{n,ic}$ are the base shot noise + flicker noise, and the collector shot noise, respectively. *KF*, *AF*, and *BF* are model parameters for the flicker noise of the amplifier. In the above analysis, the noise of R_{B1} and R_{B2} are neglected due to their small effect on the overall noise in good oscillator design. Fig. 3.17 shows the good correlation between the simulations and (3.25) with 1 dB difference in noise floors. The figure is generated assuming certain values for the flicker parameters (*KF*, *AF*, and *BF*) since they were not modeled for the transistor. These parameters were extracted from a simple curve fitting of the measured oscillator phase noise in the lab. Hence f_c and F were extracted and fed back to (1.1).

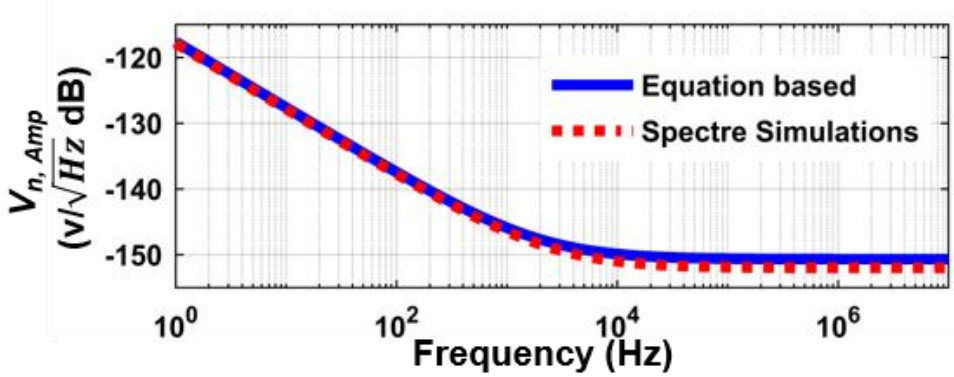

Fig. 3.17. Amplifier output noise based on Equation (3.25) and circuit simulations [12].

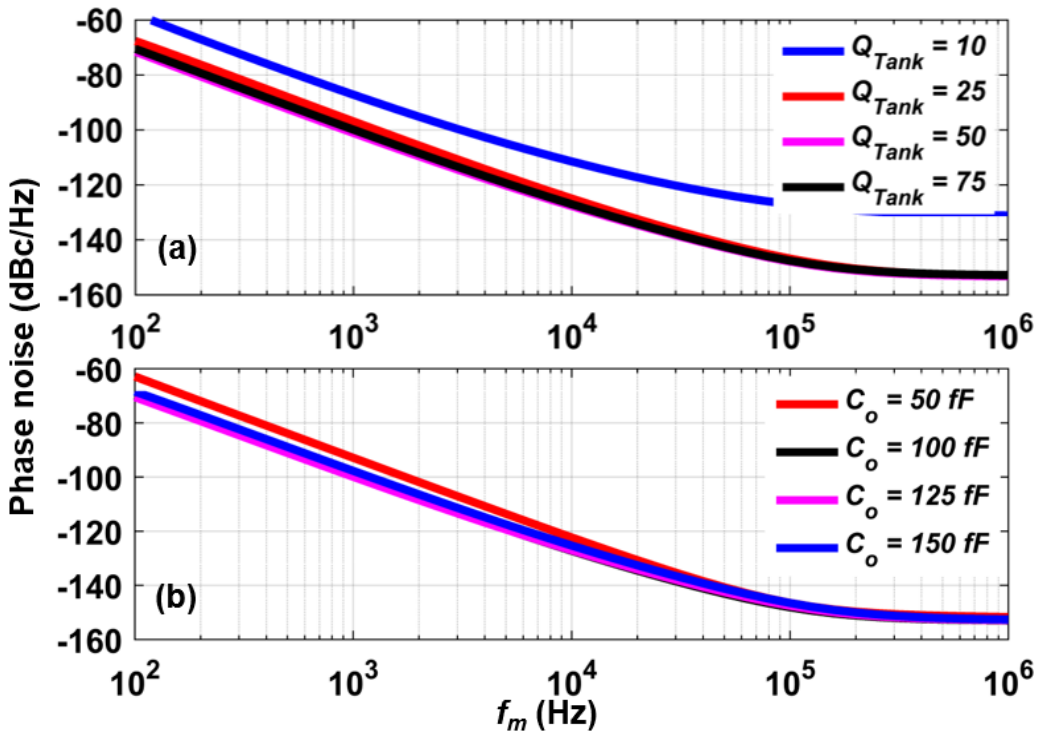

Fig. 3.18. Simulated effect of (a) Q_{tank} and (b) C_o on the phase noise profile of the 415 MHz carrier [12].

3.3.5.2 Closed-Loop TF G_{noise} Including Loading Effect

The remaining unknown parameter is G_{noise}. Considering all the parasitics and the loading effects on the LOBAR, G_{noise} is given as:

$$G_{noise} = \frac{TF_{Amp}}{1 - TF_{Amp}\, TF_{MEMS}\, TF_{tank}} \tag{3.26}$$

And now we have a modified Leeson's equation for our VCMO.

3.3.5.3 Effect of Q_{tank}, and C_o on Phase Noise

Following the same approach as the previous subsections, phase noise should be investigated as a function of critical circuit parameters. Fig. 3.18(a) shows the effect of varying Q_{tank} on the 415 MHz resonance phase noise. The mode is excited using a simulated V_{VAR} of 3V. Increasing the Q_{tank} from 25 to 75 enhances the 1 kHz offset phase noise by 4.2 dB due to the lower loading on the LOBAR. A Q_{tank} of 10 shows a completely different phase noise profile when compared to the rest. A very low Q_{tank} deteriorates the noise floor by 23 dB due to the lower carrier power which is a result of a lower loop gain provided for such resonance as explained earlier in Section 3.3.3 and deteriorates the 1 kHz offset noise by 14 dB when compared to a Q_{tank} of 75. The effect of increasing C_o on the phase noise profile is shown in Fig. 3.18(b). Increasing C_o while fixing other parameters like f_s, Q, and k_t^2 reduces R_m with the same ratio of increasing C_o as previously mentioned in Section 3.3.4. An optimal combination of C_o and R_m produces the optimum phase noise. For the 415 MHz resonance as an example, there is a sweet point at C_o of 125 fF. A very small resonator hurts the phase noise in general due to larger R_m at resonance and hence smaller carrier power.

Fig. 3.19 shows the effect of varying the Q_{tank} on the phase noise of the 505 MHz carrier (the mode with the lowest FoM). Increasing the Q_{tank} from 25 to 75 enhances the 1 kHz offset noise by 7 dB due to the lower loading on the LOBAR.

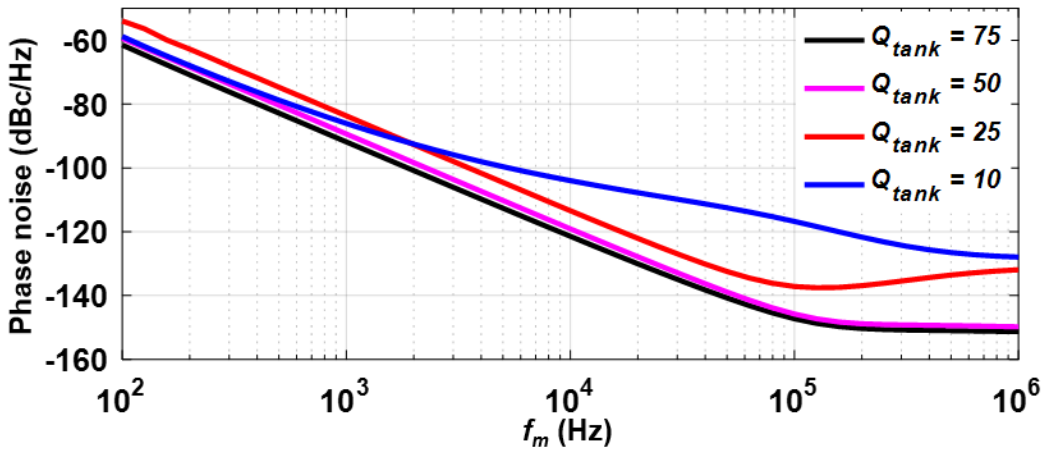

Fig. 3.19. Simulated effect of Q_{tank} on the phase noise profile of the 505 MHz carrier [12].

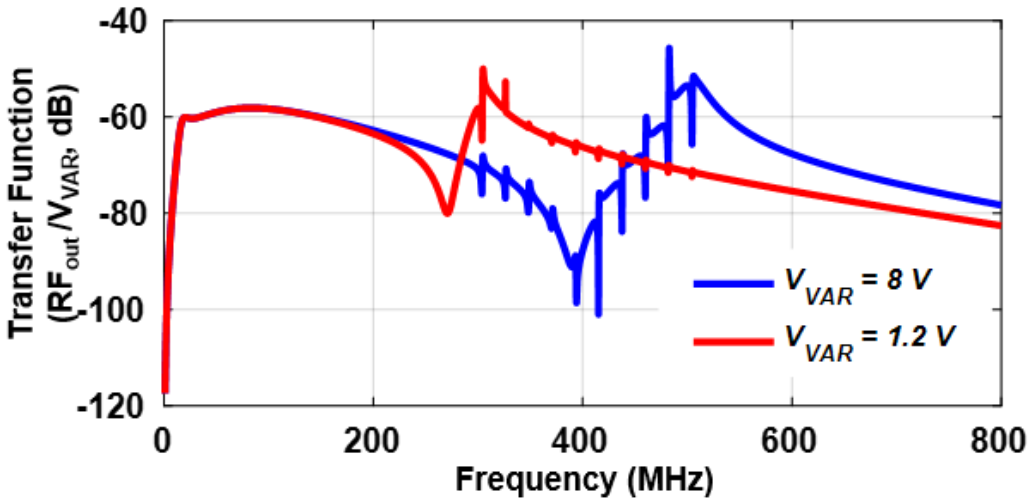

Fig. 3.20. Transfer function from the varactor input (V_{VAR}) to the oscillator output (RF_{OUT}) [12].

A Q_{tank} of 10 shows a completely different phase noise profile in comparison to the rest, suggesting the excitement of a close-by mode (480 MHz resonance in this case, as mentioned above). When compared to the case with a Q_{tank} of 75, a low Q_{tank} of 10 deteriorates the 1 kHz offset noise by 5 dB and the noise floor by 23 dB due to the lower carrier power resulting from a lower loop gain provided for such resonance.

Understanding the effect of the noise at the varactor input on the phase noise profile is critical. Fig. 3.20 shows the transfer function from V_{VAR} to the oscillator output. High *Q* passive components and the high *Q* varactor used in the demonstration give a minimum noise suppression of 45 dB at 480 MHz at the varactor input. This suppression translates to -105 dBc/Hz phase noise contribution from the varactor input at 1 kHz offset from a 500 MHz carrier, suppressing up to 2 $\mu V_{rms}/\sqrt{Hz}$ noise density or ~ 2 mV_{rms} integrated noise up to 1 MHz bandwidth at the varactor input without affecting the phase noise values.

3.4 VCMO MEASUREMENTS

SMA connectors are used for all DC-biases to minimize any noise pick-up from the external sources. Fig. 3.8(b) shows a PCB prototype with $LiNbO_3$ LOBAR sample bond-wired to the oscillator. A tunable oscillation frequency ranging from 300 to 500 MHz has been achieved by exploiting the ten overtones in the LOBAR. As shown in Fig. 3.21(a), the VCMO shows continuous tuning near the series resonance of each overtone and a discrete hop of roughly 20 MHz when switching to an adjacent overtone. The continuous tuning region for each varactor bias V_{VAR} is shown in Fig 3.21(c). Such a continuous range can be helpful for environmental and temperature shift corrections. This range can be increased by increasing the k_t^2 of each tone and increasing the power consumption of the VCMO. As shown in Fig. 3.21(b), a specific V_{VAR} can produce a maximum output power of 0 dBm for each tone across their continuous tuning range. The VCMO consumes only 9 mW in operation owing to the high FoM of the LOBAR.

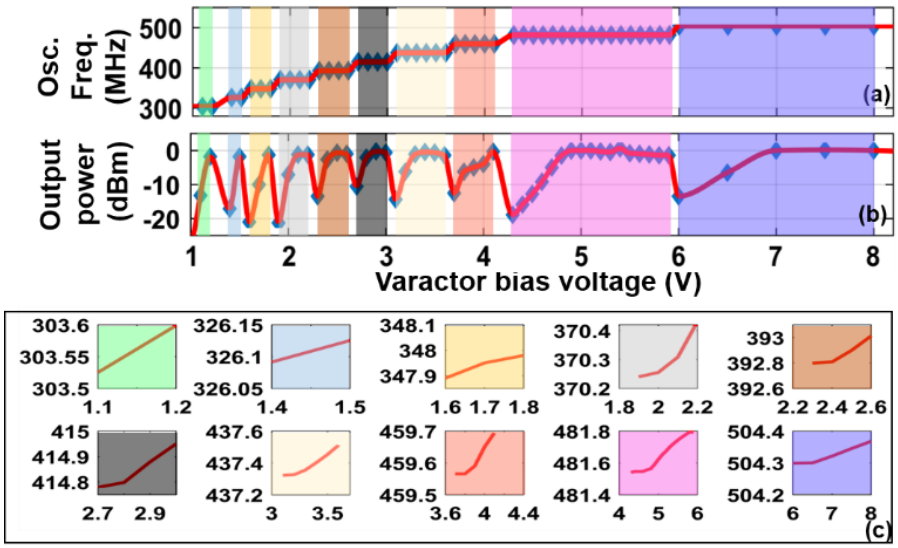

Fig. 3.21. (a) Oscillation frequency and (b) output power versus varactor bias. (c) Tuning response for each mode. Color codes are included for easy correlation [12].

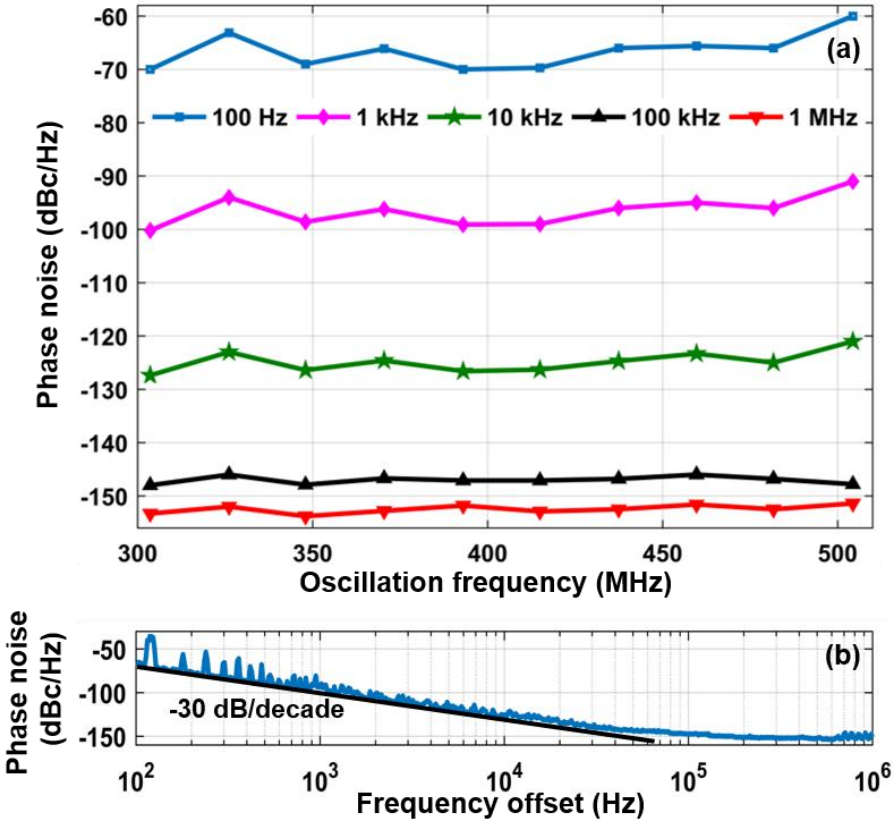

Fig. 3.22. (a) Phase noise of the 10 locked modes at different frequency offsets. (b) Phase noise plot of the 415 MHz mode [12].

Phase noise measurements were done with an Agilent E5052A Signal Source Analyzer and are reported in Fig. 3.22. The VCMO demonstrates -100 dBc/Hz phase noise at 1 kHz offset from a 300 MHz carrier, and the best noise floor of -153 dBc/Hz due to high FoMs of $LiNbO_3$ LOBARs. Fig. 3.22(b) shows the phase noise profile for the 415 MHz carrier as an example. The spurious profile is believed to be a result of the spurious resonance mode shown in Fig 3.7(b). Our VCMO is characterized with an FoM_{OSC} (1.2) of 200 dB, and 193 dB at 1 kHz and 1 MHz offsets from a 300 MHz carrier.

3.5 SUMMARY AND CONCLUSIONS

Table 3.2 shows a performance summary and comparison to other reconfigurable MEMS oscillators. This dissertation presents the highest number of locked tones of a single acoustic resonator with competitive phase noise and FoM_{OSC} results, making $LiNbO_3$ LOBAR VCMO a great candidate for direct RF synthesis deployed in wireless transceivers targeting multi-mode IoT applications. The tuning range and power consumption can be further enhanced via implementing the active circuitry in a recent-node CMOS. Moreover, having a switchable bank of tunable LC tanks with different inductor values would allow the VCMO to harness all the overtones provided by the LOBAR for a broader tuning range.

To have a fully continuous tuning range rather than a discrete one, the VCMO may lock to more closely packed resonances (i.e., a resonator with a smaller Δf). Hence, the LOBAR would have a larger width W_T, trading off k_t^2 of the resonances and inducing worse phase noise and larger power consumption in the

oscillator. In addition, this solution requires a very high Q_{tank} and a widely reconfigurable filter to pick up the intended resonance. An alternative solution might be switching among a bank of LOBARs with slightly different f_{center}. Only the LOBAR with the target resonance would be connected to the loop. This approach saves on power consumption and maintains the phase noise at the expense of a larger footprint. A third approach is to use an open fractional divider after the VCMO buffer to produce a continuous range of lower frequency carriers.

Table 3.2 Performance Summary and Comparison to Reconfigurable MEMS Oscillators

Reference		**This work [12]**	[61]				[63]				[65]		[66]		[101]		
MEMS		**$LiNbO_3$ LOBAR**	AlN CMR				AlN CMR				AlN CMR		AlN-on-Si		SAW		
Process		**Discrete**	0.5 µm CMOS				0.5 µm CMOS				0.5 µm CMOS		0.5 µm CMOS		0.18 µm CMOS		
General-purpose		**Yes**	Yes				Yes				No		No		Yes		
Number of resonances		**10**	4				4				2		2		3		
Number of resonators		**1**	4				4				1		1		3		
Frequencies (MHz)		**300 - 500 (ten equally-spaced tones)**	268	483	690	785	176	222	307	482	472	1940	35	175	315	433	500
dc power (mW)		**9**	As high as 35.5				10				-	20	3.8	13.5	11.3	8.1	6.8
Output power (dBm)		**0**	1.1	0	-2.7	-6	-4.7	-4.8	-6.7	-13.6	-6.5	-16	12.1	3.8	-	-	-
PN (dBc/Hz)	1 kHz	**-100**	-94	-88	-83	-70	-79	-88	-84	-68	-82	-69	-112	-103	-	-	-
		-149.5	-142.6	-141.7	-139.8	-127.9	-123.9	-134.9	-133.7	-121.66	-135.5	-134.8	-142.9	-147.9	-	-	-
	1 MHz	**-153**	-	-	-	-	-	-160	-	-	-160	-153	-142	-140	-134	-141	-135
		-202.54						-206.9			-213.5	-218.8	-172.9	-184.9	-184	-193.8	-189
FoM_{OSC} (dB)	1 kHz	**200**	187	186	184	172	174	185	184	172	-	182	197	197	-	-	-
	1 MHz	**193**	-	-	-	-	-	197	-	-	-	205.7	167	173.6	173.4	184.6	180.6

The values in the shaded cells are referenced to a 1 MHz carrier.

PART II: MULTI-GHz RF-MEMS OSCILLATORS

CHAPTER 4: A *Ku*-BAND OSCILLATOR UTILIZING OVERTONE LITHIUM NIOBATE RF-MEMS RESONATOR FOR 5G

4.1 INTRODUCTION

This chapter focuses on our third project, a *Ku*-band RF-MEMS oscillator for 5G communications. This chapter presents a 12.9 GHz silicon germanium (SiGe) Pierce oscillator utilizing a third antisymmetric overtone in a $LiNbO_3$ resonators. Quarter-wave resonators are used to satisfy the Barkhausen oscillation conditions for the 3rd overtone while suppressing the fundamental and higher-order resonances. The oscillator achieves measured phase noise of -70 and -111 dBc/Hz at 1 kHz and 100 kHz offsets from a 12.9 GHz carrier while consuming 20 mW of dc power. The oscillator achieves a FoM_{OSC} of 200 dB at 100 kHz offset, surpassing the SoA EM and overtone MEMS oscillators. The achieved oscillation frequency is the highest reported to date for a MEMS oscillator. The demonstrated performance shows the strong potential of microwave acoustic oscillators for 5G frequency synthesis. This work will enable low-power 5G transceivers featuring high speed, high sensitivity, and high selectivity in small form factors.

The rest of the chapter is organized as follows: Section 4.2 introduces the SoA multi-GHz resonators. Section 4.3 then focuses on antisymmetric mode $LiNbO_3$ resonators employed to implement the oscillators in Chapters 4 and 5. Section 4.4 reports on the design, and implementation of the oscillator, while Section 4.5 presents the measurements results. Finally, Section 4.6 compares the results with prior arts, summarizes and concludes the chapter.

4.2 SoA MULTI-GHz RESONATORS

SoA microwave oscillators are based on *LC* [102], microstrip [103], active [104], and dielectric resonators (DR) [105]. On-chip lossy LC tanks are compact, hence offering a low-cost solution. However, their low Q at microwave frequencies translates to poor phase noise and high-power consumption. Quarter wavelength EM resonators have footprints on the order of 7.5 mm for a 10 GHz resonance, making them too bulky for handsets. DROs offer superior phase noise performance, but they are bulky and consume a large amount of power.

Alternatively, oscillators based on RF-MEMS resonators that harness the confinement of acoustic waves and have the size of hundreds of microns, are attractive for portable devices. Recently, acoustic resonators with resonances above 10 GHz have been demonstrated in different platforms such as aluminum nitride (AlN) thin-film bulk acoustic resonators (FBARs) [106], AlN contour mode resonators (CMRs) [107], [108], scandium doped AlN resonators [109], [110], ferroelectric resonators [111], finFET resonators [112], and lithium niobate (LiNbO3) resonators [113]-[116]. From this group, $LiNbO_3$ resonators feature the highest demonstrated FoM_{RES} making them the more suitable candidate for

enabling chip-scale oscillators with simultaneously low phase noise and low power consumption.

4.3 ANTISYMMETRIC MODE $LiNbO_3$ RF-MEMS RESONATORS

4.3.1 Overview

Antisymmetric modes (A-modes) are a class of Lamb-wave modes characterized by their antisymmetric vibrations about the median plane of the plate. These modes have equal vertical but opposite longitudinal displacement components on the opposite sides of the median plane. The resonance of an A-mode resonator is primarily set by the thickness of the $LiNbO_3$ film (T_{LN}), the wavelength (λ_l) and the mode order (m). A smaller thickness would translate to a higher fundamental frequency; however, this requires careful fabrication and a sophisticated deposition method for thin films to maintain high Q. Empirically, thinner films display worse crystallinity than thicker ones causing degradation in Q. Thinner films are also more susceptible to any fabrication-induced non-uniformity, causing meager yield and uncertainties in setting the center frequency precisely. The overmoding approach helps in achieving higher resonant frequencies without thinning down the resonator and adding fabrication complexity. It also provides better linearity and power handling due to the larger volume of the device structure. A high FoM_{RES} is crucial for overmode resonances scaling towards microwave frequencies [13].

The theory defining the resonant frequencies for the excited odd modes can be found in [113]. Higher-order A-modes are better confined between electrodes due to the increasingly larger dispersion mismatch between metalized and un-

metalized regions for higher-order modes. This feature leads to less acoustic damping loss from the electrodes and less energy loss to the supporting substrate for the higher-order modes. Hence, higher order-mode might display higher mechanical FoM ($Q_m \cdot f$) product but lower loaded FoM ($Q_l \cdot f$) product due to EM losses as will be shown later.

The resonators used to build the acoustic oscillators reported in Chapters 4 and 5 are comprised of a 3-electrode transducer on top of a mechanically suspended Z-cut $LiNbO_3$ thin-film. The electrodes, being connected to signal and ground, induce lateral electric fields in the piezoelectric film, hence exciting the resonator into odd-order antisymmetric vibrations. The resonators were fabricated using a process described in [56].

4.3.2 A_3 $LiNbO_3$ Z-cut Resonator Design and Measurements

For the resonator shown in Fig. 4.1 (a), a 400 nm thick Z-cut $LiNbO_3$ film is used. For a λ_l of 6 μm and m of 3, A_3 resonance rises beyond 12 GHz which is desired for investigating *Ku*-band acoustic oscillators in this chapter. A 50 nm gold (Au) layer is sputtered and lifted off to form the top electrodes. Au probing pads of 60×40 μm^2 are electroplated to 2 μm thickness with a 200 μm pitch to reduce the parasitics between the pads.

The resonator was measured and characterized using the Keysight N5230A PNA-L network analyzer. A Thru-Reflect-Line (TRL) calibration is done in measurements using on-wafer standards. A multi-resonance MBVD model shown in Fig. 4.1 (d) is used to interpret the measured admittance shown in Fig. 4.1 (c). The MBVD model includes an additional series inductor (L_s = 90 pH) and a resistor

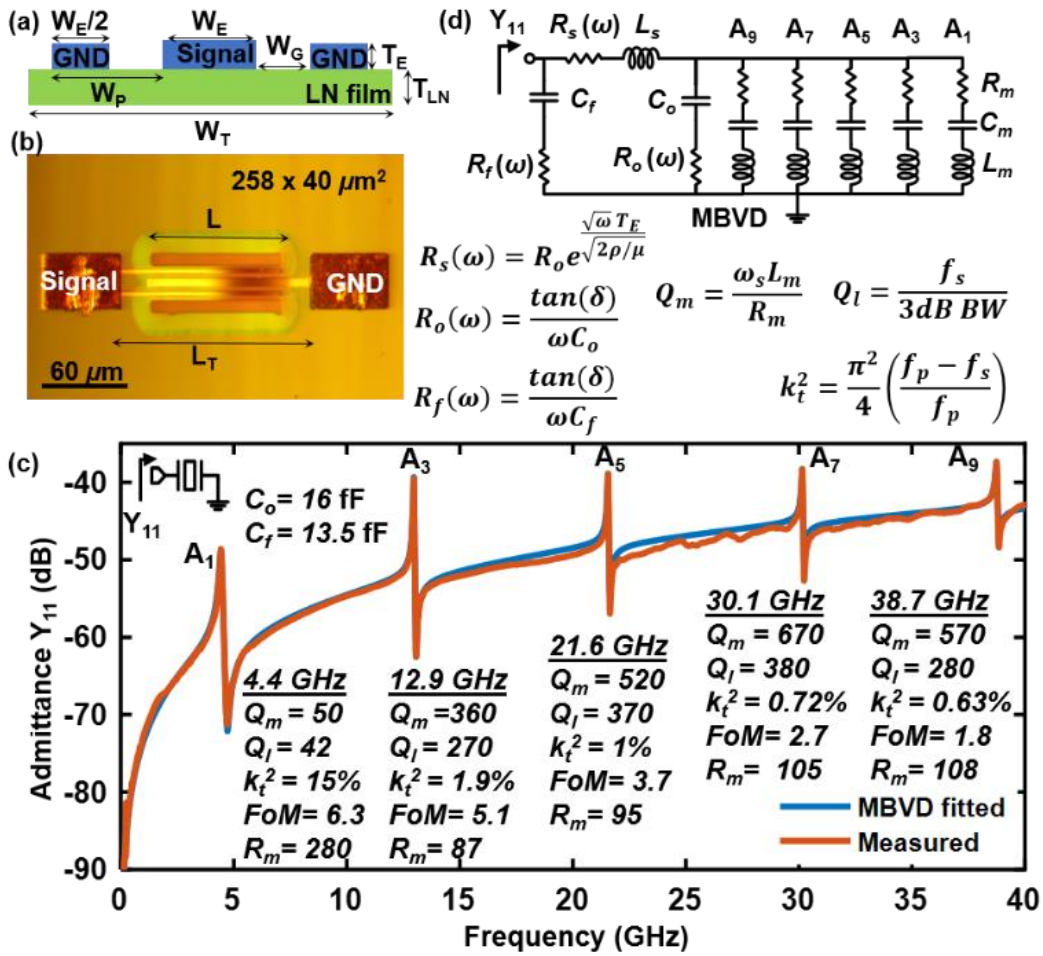

Fig. 4.1. (a) Mockup cross-sectional view of the $LiNbO_3$ resonator with key parameters shown. W_T = 21 µm, $W_G = W_E/2$= 3 µm, T_E = 50 nm, thickness of the electroplated Au pad is 2 µm, T_{LN} = 400 nm, L_T = 142 µm, L = 100 µm, and pad area is 60 x 40 µm^2. (b) Optical image of the fabricated resonator. (c) Measured and MBVD fitted response for the first 5 odd modes. (d) Multi-resonance equivalent MBVD model with parasitics included. tan(δ) is the loss tangent of $LiNbO_3$, ρ is the resistivity of thin-film Au, and μ is the permeability of Au. Mechanical (Q_m), loaded (Q_l) quality factors, k_t^2, FoM, and R_m of each tone are shown [13].

(R_s = 13.4 Ω at 13 GHz) to model the non-negligible inductance and the surface resistance of the electrodes at high frequencies, respectively. It also includes a capacitor of 13.5 fF and a resistor (R_f) to model the feedthrough capacitance (C_f), and the resistive substrate loss, respectively. The resonator is also characterized by a static capacitance from the IDT (C_o) of 16 fF, which is set by the size of the resonator. The loaded quality factor (Q_l) is measured for each resonance using the

3dB bandwidth method, while the mechanical quality factor (Q_m) is extracted via the MBVD model by excluding the electrical loss. C_f is not de-embedded for catching all the parasitic effects associated with the resonator. k_t^2 is also extracted for each resonance considering all the device parasitics.

The first five odd modes A_1, A_3, A_5, A_7, and A_9 with resonances at 4.4, 13, 22, 30, and 39 GHz are characterized. Key measured and extracted parameters, including Q_l, Q_m, and k_t^2, are shown in Fig 4.1 (c). For higher-order modes, Q_l is 270 for A_3 and 380 for A_7 while Q_m is 360 for the A_3, and 670 for A_7. For these modes, Q_m varies from $1.3Q_l$ at 13 GHz to $2Q_l$ at 39 GHz, indicating that mitigating electrical loss is crucial for high-performance at microwave and mm-wave frequencies. k_t^2 decreases from 15% for A_1 to 0.63% for A_9 with a value of 1.9% for A_3. The reason behind the degradation of k_t^2 with an increasing mode order can be found in [113].

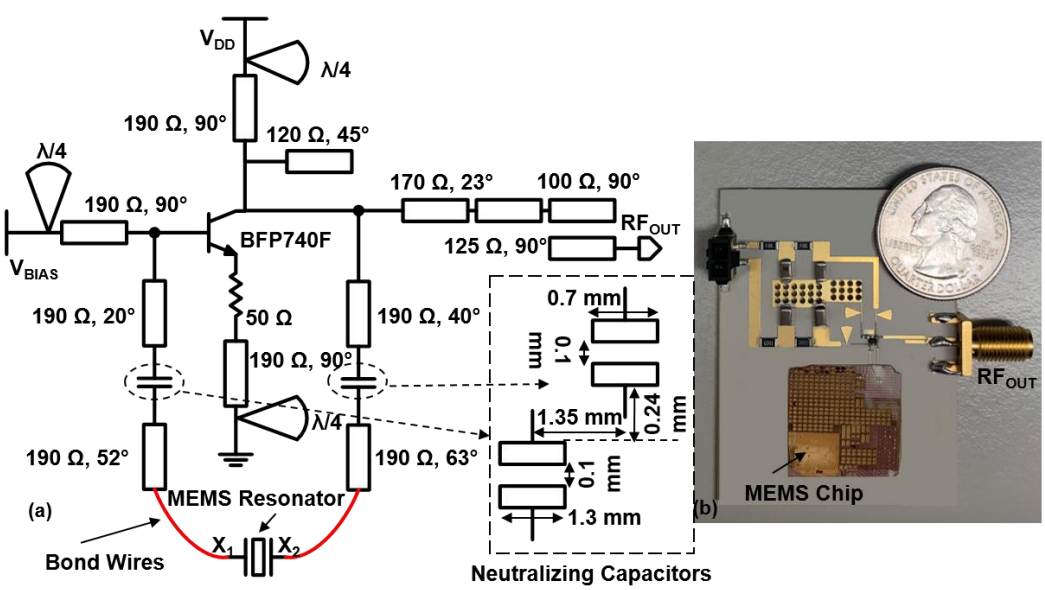

Fig. 4.2. (a) Simplified schematic of the RF portion of the 13 GHz oscillator. (b) Oscillator PCB. [13].

4.4 OSCILLATOR DESIGN

The Pierce oscillator shown in Fig. 4.2 (a) is used to excite the resonator 3rd overtone at 13 GHz. Infineon BFP740F Silicon Germanium (SiGe) NPN heterojunction bipolar transistor (HBT) is used for its low noise figure which is critical for low phase noise oscillations. The transistor has cut-off frequencies f_t of approximately 45, and 27 GHz at collector currents I_C of 25, and 5 mA. Rather than any higher-order resonance, A_3 is chosen for a low-power solution primarily due to the limitations of f_t. Bias voltages V_{CE} and V_{BE} of 2.7 and 0.8 V respectively are chosen for optimal phase noise performance while consuming 20 mW of dc power. A 50 Ω degeneration resistor is used to set the transistor bias and help in boosting the linearity at the expense of slightly higher power consumption.

The resonator-loading reactances needed for the Pierce operation at 13 GHz are realized mainly through the transistor junction capacitances (C_{CB} of 80 fF, C_{CE} of 0.3 pF, and C_{BE} of 0.4 pF) and an open circuit stub of 120 Ω and 45° in electrical length at 13 GHz. The stub creates a reactance equivalent to a capacitance of 100 fF at the collector terminal. In addition, the resonator static capacitance C_o, the feedthrough capacitance C_f, and the PCB parasitic capacitances are also included in the loading reactance.

Bias-Tees are critical in the design for optimal performance. Open $\lambda/4$ radial stub of low impedance is used to create an RF choke in the DC arm, hence allowing the DC bias and isolating RF from the bias network [not shown in Fig. 4.2 (a)]. A high impedance (190 Ω) $\lambda/4$ line is used to transform the RF short to an RF open

circuit at all the transistor terminals. Thus, the biasing arm does not load the RF path. The lengths of the quarter-wave stubs are chosen for 13 GHz. An output matching network is used for 50 Ω measurements. The network is designed to have a low insertion loss for high output power and low noise floor, while not loading the collector or worsen the flicker and thermal phase noises.

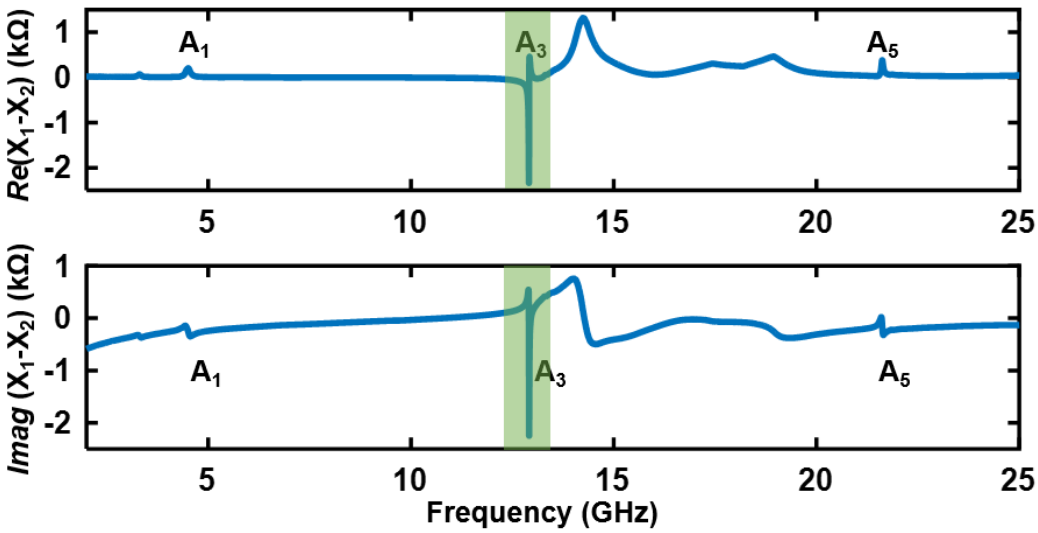

Fig. 4.3. Simulated real and imaginary input impedances across circuit nodes X_1, and X_2. Only the 3rd order mode is excited [13].

To satisfy the Barkhausen's loop-phase condition of oscillation, special attention is given to the trace between the base and the collector. Hence, the transmission lines impedances, lengths, and the resonator wire bonds are extensively simulated using Keysight Momentum. Variations in the trace lengths will change the frequency of oscillation and the phase noise profile. Two capacitors in the positive feedback path are implemented as parallel traces to neutralize the wire-bond inductances and hence force the frequency of oscillation to be as close to A_3 resonance as possible, thus enhancing the loaded Q and the phase noise. The

oscillator is assembled on a Rogers RO3003 board with a thickness of 1.52 mm, a dielectric constant of 3, and a dissipation factor of 0.0013 at 10 GHz. The conditions of oscillation are satisfied for only the 3rd order resonance, while the fundamental and higher-order resonances are suppressed as shown in Fig. 4.3.

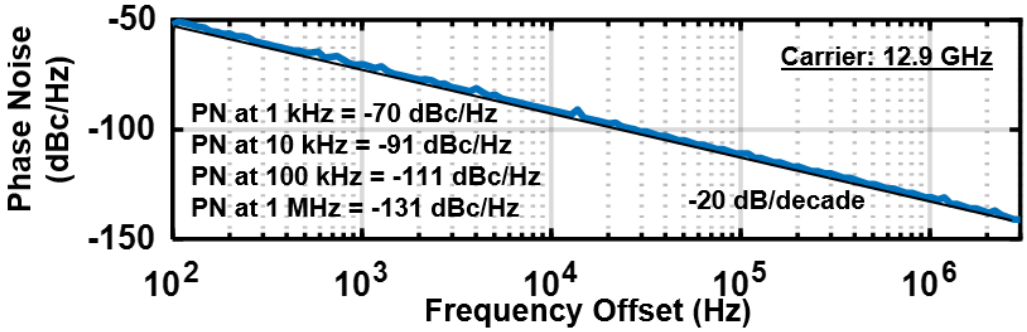

Fig. 4.4. Measured phase noise of the 13 GHz carrier [13].

4.5 MEASUREMENTS

The active portion of the Pierce oscillator on the Rogers RO3003 board is integrated with the MEMS chip (2 cm × 2 cm) via wire bonding. The assembly is shown in Fig. 4.2 (b). Phase noise measurements are taken using an R&S FSUP26 signal analyzer and reported in Fig. 4.4. The oscillator achieves measured phase noise of -70 and -111 dBc/Hz at 1 kHz and 100 kHz offsets from a 12.9 GHz carrier. The phase noise profile shows a -20 dB/decade trend between 100 Hz and 1 MHz offsets from the carrier. The -30 dB/decade trend is not captured in the region of interest due to the low flicker noise characteristics of the SiGe transistor. For the reported phase noise values, the oscillator consumes dc power of 20 mW and

achieves a FoM_{OSC} of 200 dB at 100 kHz offset. The measured output power is -8.5 dBm.

Table 4.1 Comparison to the SoA RF-MEMS Oscillators above 5 GHz

Reference		**This work [13]**	[117]		[118]		[119]	
Resonator		**$LiNbO_3$ 3rd tone**	FBAR fundamental		FBAR fundamental		FBAR 3rd tone	
IC Process		**discrete**	0.35 μm BiCMOS		discrete		discrete	
Osc. Freq. (GHz)		**12.9**	5.46		5		7	
Resonator footprint (mm^2)		**0.01**	0.034		> 0.1		-	
Q_l		**270**	300#		300		1350	
k_t^2 (%)		**1.9**	6.67#		4.3		-	
FoM_{RES}		**5.1**	20		12.9		-	
dc power (mW)		**20**	12.7		-		16.2	
PN (dBc/Hz)	1 kHz	**-70**	-64^	-56.5	-		-	
	100 kHz	**-111**	-117.7	-110.2	-109.5	-101	-80	-74.7
	1 MHz	**-131**	-		-		-110	-104.7
FoM_{Osc} (dB)	100 kHz	**200.2**	201.4		-		164.8	

Table 4.2 Comparison to the SoA EM Oscillators

Reference		**This work [13]**	[105]			[103]	[104]	[102]
Resonator		**$LiNbO_3$**	DRO			µstrip	Active	LC
IC Process		**discrete**	GaN	GaAs	SiGe	BJT	discrete	BiCMOS
Osc. Freq. (GHz)		**12.9**	10.6			10	10	15
Resonator footprint (mm^2)		**0.01**	-			-	-	-
Q_l		**270**	600			-	1211	-
dc power (mW)		**20**	-			200	500	72
PN (dBc/Hz)	1 kHz	**-70**	-53††	-76††	-90††	-65†	-	-
			-51.3	-74.3	-88.3	-62.8		
	100 kHz	**-111**	-118	-123	-135	-113	-114.4	-102*
			-116.3	-121.3	-133.3	-110.8	-112.2	-103.3
FoM_{Osc} (dB)	100 kHz	**200.2**	-			190	187.4	187

The values in the shaded cells are referenced to a 12.9 GHz output. # as reported in [120]. ^ value estimated from a plot in [117]. †† value estimated from a plot in [105]. † value estimated from a plot in [103]. *value estimated from a plot in [102].

4.6 SUMMARY AND CONCLUSIONS

In comparison to the SoA, as shown in Tables 4.1 and 4.2, the FoMs of our oscillator surpass those of the SoA EM and overtone MEMS oscillators. Moreover, the achieved oscillation frequency is the highest reported to date for an RF-MEMS oscillator. The demonstrated performance shows the strong potential of microwave acoustic oscillators for 5G frequency synthesis. They offer small form factors and long battery life solutions with competitive phase noise performance in comparison to other EM oscillators. Further reduction in footprint and power consumption can be achieved by realizing the active circuit with a recent CMOS node.

CHAPTER 5: AN *L*-AND-*X* BAND DUAL FREQUENCY SYNTHESIZER UTILIZING LITHIUM NIOBATE RF-MEMS AND OPEN LOOP FREQUENCY DIVIDERS

5.1 INTRODUCTION

With access to high *Q* acoustic resonators previously mentioned in Chapter 4 [106]-[115], the next challenge is to design the frequency synthesizer for generating different carrier frequencies. The conventional frequency synthesis has been relying on a power-hungry PLL referenced to a bulky high *Q* XO. XOs are hardly tunable and generate only low frequencies (<120 MHz), thus necessitating a PLL as a tunable frequency multiplier and leading to a larger footprint, higher power, more spurs, and greater cost [4]. To overcome these shortcomings, we develop a direct frequency synthesizer based on integrating an X-band $LiNbO_3$ RF-MEMS oscillator with CMOS open-loop frequency dividers. Instead of generating LO frequencies from a low-frequency source and "bubbling up" through a PLL, our work creates a low-power microwave low-noise source and then "trickles down" to an LO frequency range from X to L bands via the frequency division. Our approach has the following vital benefits: (1) lower power consumption; (2) a smaller footprint when compared to off-chip XOs/PLLs; (3) RF carriers with lower phase noise/jitter for better receiver sensitivity; (4) spurs-free phase noise (unlike

PLL) for enhancing receiver selectivity; and (5) a faster response and lower energy dissipation from removing the overhead for XO startup or a PLL locked to an XO.

This chapter presents an 8.6 GHz CMOS oscillator utilizing A_3 in a $LiNbO_3$ RF-MEMS resonator. The oscillator consists of an acoustic resonator in a closed loop with cascaded RF tuned amplifiers (TAs) built on TSMC RF GP 65 nm CMOS. The TA bandpass response, set by on-chip inductors, satisfies Barkhausen's oscillation conditions for A_3 while suppressing the fundamental and higher-order resonances. Two circuit variations are implemented. The first is an 8.6 GHz standalone oscillator with a source-follower buffer for direct 50-Ω-based measurements. The second is an oscillator-divider chain using an on-chip 3-stage divide-by-2 frequency divider for a ~1.1 GHz output. The standalone oscillator achieves measured phase noise of -56, -113, and -135 dBc/Hz at 1 kHz, 100 kHz, and 1 MHz offsets from an 8.6 GHz output while consuming 10.2 mW of dc power. The oscillator also attains a figure-of-merit of 201.6 dB at 100 kHz offset, surpassing the SoA EM [102]-[105], RF-MEMS oscillators [13], [117]-[120], and X-band PLLs [121]-[124]. The oscillator-divider chain produces phase noise of -69.4 and -147 dBc/Hz at 1 kHz and 1 MHz offsets from a 1075 MHz output while consuming 12 mW of dc power. Its phase noise performance also surpasses the SoA L-band PLLs [125], [126].

The rest of the chapter is organized as follows: Section 5.2 reports on the design and measurements of the antisymmetric mode $LiNbO_3$ MEMS resonators employed to implement the oscillators in this work. Section 5.3 then focuses on the design, implementation, and measurement results of the 8.6 GHz oscillator. Section

5.4 explains the design and the implementation of the oscillator-divider chain and reports the measurement results at 1.1 GHz. Finally, Section 5.5 compares the results with prior arts and concludes the paper.

5.2 A-MODE $LiNbO_3$ RF-MEMS RESONATORS

For the resonator shown in Fig. 5.1 (a), a 650 nm thick Z-cut $LiNbO_3$ film is used. For a λ_l of 12 μm and m of 3, A_3 resonance rises beyond 8 GHz, which is desired for investigating *X*-band acoustic oscillators. Two identical resonators (A and B) were fabricated, with the dimensions given in the inset of Fig. 5.1. A 180 nm layer of copper (Cu) is sputtered and lifted off to form the top electrodes. Cu probing pads of 60×62 μm^2 are electroplated to 3 μm thickness with a 200 μm pitch to reduce the parasitics between the pads.

Resonators A and B were measured and characterized using the same technique described in Chapter 4. The first five odd-order modes, namely A_1, A_3, A_5, A_7, and A_9 with resonances at 2.9, 8.6, 14.3, 20, and 25.7 GHz, are characterized. For resonator A, Q_l and Q_m are 384 and 424 for A_3, 12 and 300 for A_9, respectively. For these modes, Q_m varies from 1.1Q_l at 8.6 GHz to 25Q_l at 25.7 GHz. k_t^2 decreases from 6.9% for A_1 to 0.98% for A_9 with a value of 2.2% for A_3. Higher FoM_{RES} resonances translate to a larger phase transition from capacitive to inductive regions which is preferred for stable oscillations. As the FoM_{RES} degrade with the frequency, the phase transition becomes far from ideal (180°). Fig. 5.1 (f) shows that modes A_5 to A_{13} are capacitive as their phases do not cross the 0° needed

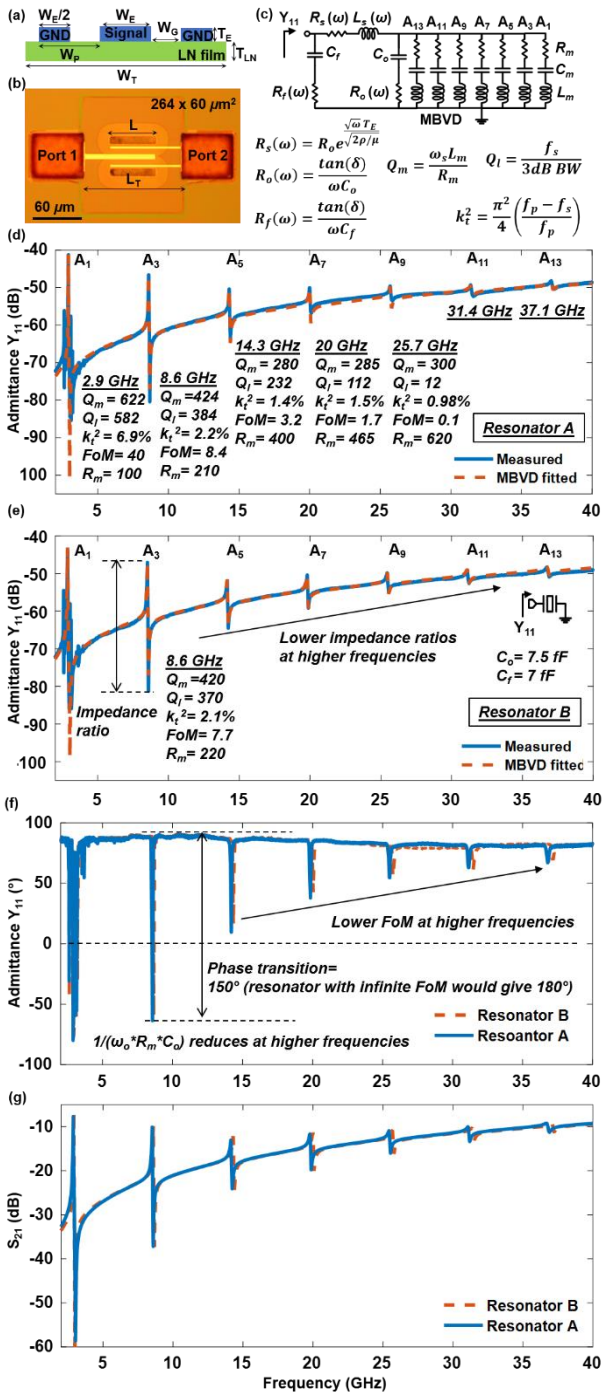

Fig. 5.1. (a) Mockup cross-sectional view of the $LiNbO_3$ resonator with key parameters shown. W_T = 32 μm, W_G = 6 μm, W_E = 8 μm, T_E = 180 nm, thickness of the electroplated Cu pad is 3 μm, T_{LN} = 650 nm, L_T = 140 μm, L = 60 μm, and pad area is 60 x 62 μm^2. (b) Optical image of the fabricated resonator. (c) Multi-resonance equivalent MBVD model with parasitics included. (d) Measured and MBVD fitted response for the first 7 odd modes of resonator A. (e) Measured and MBVD fitted response for the first 7 odd modes of resonator B. (f) Measured phase responses of resonators A and B. (g) S_{21} MBVD fitted response for resonators A and B. tan(δ) is the loss tangent of $LiNbO_3$, ρ is the resistivity of thin-film Cu, and μ is the permeability of Cu. Mechanical (Q_m), loaded (Q_l) quality factors, k_t^2, FoM, and R_m of each tone are shown [14].

at resonance. To excite these higher-order modes, extra inductors might be required to be added either in series or in parallel to the resonator hurting its Q.

Resonator B has a very similar admittance to resonator A. A_3 of resonator B is characterized by a Q_l of 370, a k_t^2 of 2.1%, and a FoM_{RES} of 7.7 at 8.6 GHz. Both resonators have an insertion loss of around 10 dB at 8.6 GHz, as shown in Fig. 5.1 (g). This value defines the minimum gain required by a 50 Ω matched oscillator to excite A_3.

The series resonant frequency of the tank—the acoustic part of the resonator plus the reactive parasitic elements (SRF_{RES})—can be deduced from the MBVD model [127]. Accounting for L_s, SRF_{RES} is around 66 GHz for our device. This SRF value was not captured by our VNA with an upper-frequency limit of 40 GHz. Careful codesign of the resonator, circuit, and integration solutions at microwave frequencies is required if a larger resonator is adopted for a smaller R_m. For example, the SRF decreases to 20 GHz for a device with R_m of 20 Ω at A_3 and C_o of 75 fF. More studies are required to fully understand the effect of the resonator size on microwave and mm-wave oscillator performance, including its power consumption, phase noise and tuning range.

5.3 *X*-BAND OSCILLATOR DESIGN

In this section, we introduce the *X*-band oscillator built on TSMC RF GP 65 nm CMOS and derive circuit parameters for meeting Barkhausen's conditions. The oscillator is designed to excite A_3 of resonator A at 8.6 GHz. Phase noise

measurements of the $LiNbO_3$ RF-MEMS oscillator are presented at the end of this section.

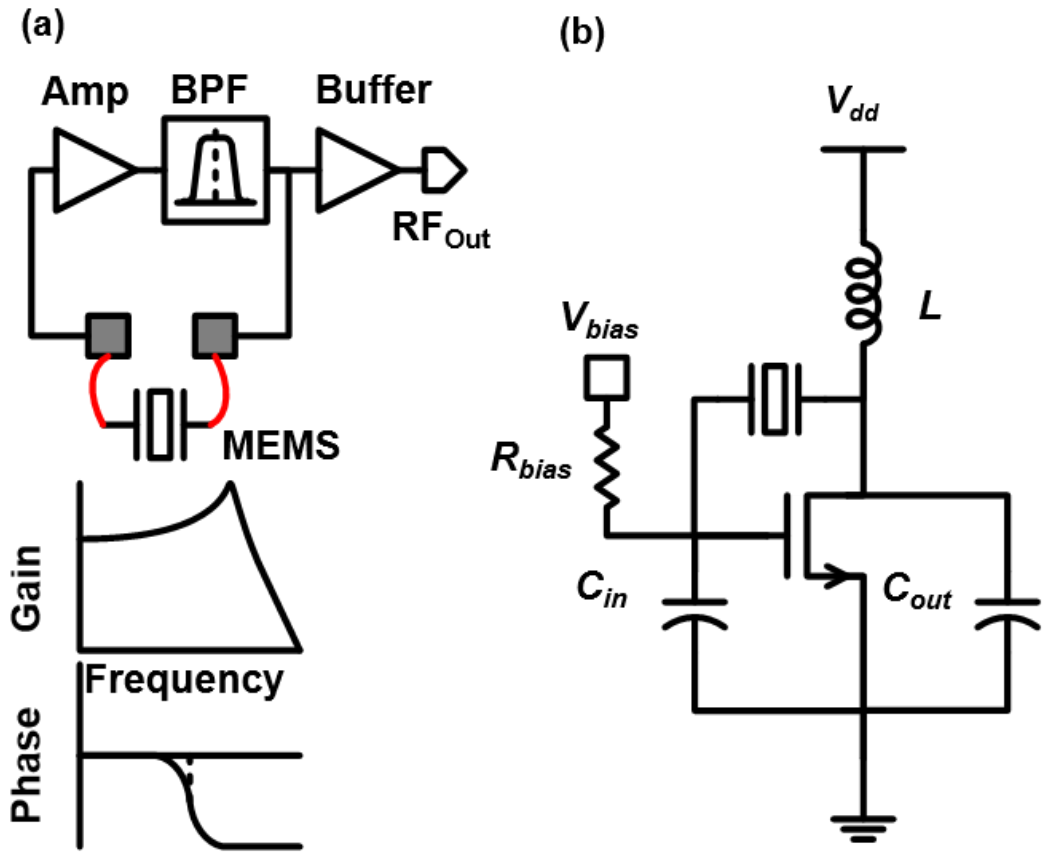

Fig. 5.2. (a) General schematic of an overtone RF-MEMS oscillator. (b) Modified Pierce oscillator with inductive loading [14].

5.3.1 Architecture

The oscillator consists of an amplifier connected to an RF-MEMS resonator in a positive feedback loop, as shown in Fig. 5.2(a). The bandpass transfer function of the amplifier allows excitation of A_3 while suppressing A_1 and other higher-order tones. The envisioned amplifier can be realized as an inductively loaded NMOS common source (CS) transistor. Connecting the resonator between the gate and drain creates a modified Pierce oscillator, as shown in Fig. 5.2(b).

Alignment of the gain peak frequency with A_3, as shown in Fig. 5.3 (the dashed-line curves), serves to satisfy Barkhausen's gain condition with minimal power consumption. However, the phase condition is not met by such alignment. The amplifier phase at the peak frequency is around -180°, as seen in Fig. 5.3(a) and the resonator phase at resonance is 0°, resulting in a loop phase of -180°. Placing the CS gain peak at a frequency between A_1 and A_3 satisfies both conditions, permitting oscillation at A_3. Unfortunately, this solution would increase the power consumption due to the lower loop gain for A_3, as the solid-line curves show in Fig. 5.3(b). The gain peak frequency depends mainly on the inductor L and the loading capacitor C_{out}. C_{in} does not change the peak frequency but affects the loop gain.

The loading inductor has a set of target metrics, such as Q, inductance L, and the self-resonant frequency (SRF_{IND}). An inductor designed for a large Q at a frequency between A_1 and A_3 translates to the design for a small L and a large C_{out}, hence lower loop gain at all frequencies. A high Q inductor provides a narrower bandpass response, thus producing a higher gain suppression of the unwanted tones. For A_3 to be minimally affected, the high Q gain peak should be close to the A_3 frequency. A larger L and a smaller C_{out} lead to lower Q, wider band response, higher loop gain at all frequencies, and a smaller gain suppression of the unwanted tones. With a lower Q inductor, the design is relaxed in terms of the precise frequency of the gain peak as long as it is between A_1 and A_3. Simulations anticipating two different sets of L and C_{out} are shown in Fig 5.4.

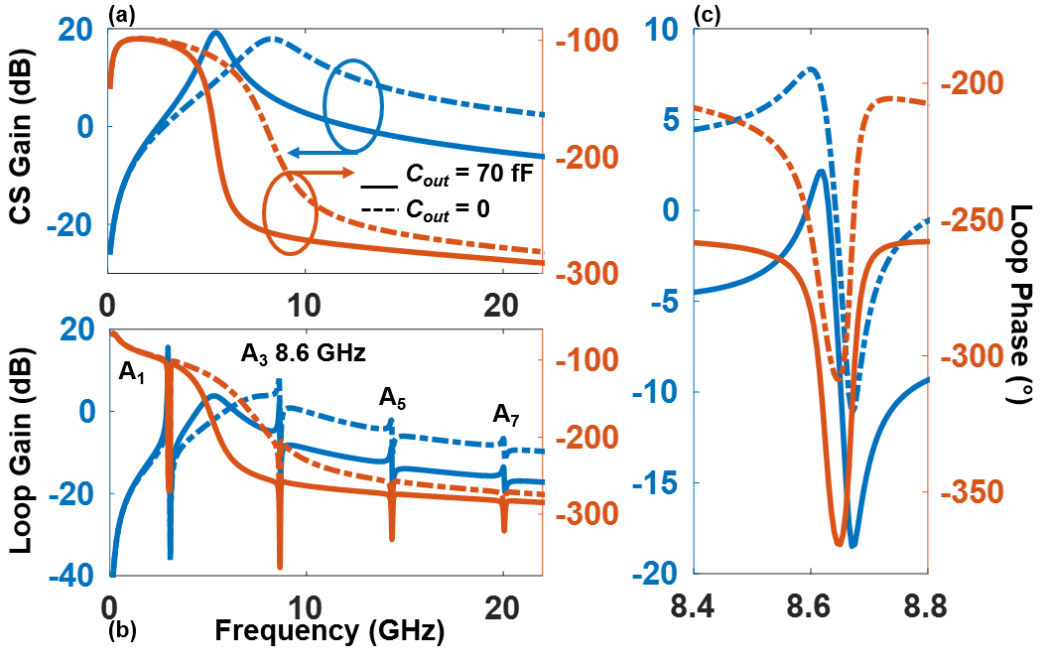

Fig. 5.3. (a) Amplifier small-signal voltage gain and phase using C_{out} of 0 (dashed-lines) and 70 fF (solid-lines). (b) Modified Pierce oscillator loop gain of the oscillator using C_{out} of 0 and 70 fF. (c) A zoom-in plot of the loop gain around 8.6 GHz. Amplifier parameters: I_{dc}= 1.97 mA, g_m=7.45 mS, *cds*=5 fF, *cgs*=32 fF, *cgd*=4.2 fF, r_{out}=4.4 kΩ, R_{bias}=10 kΩ [14].

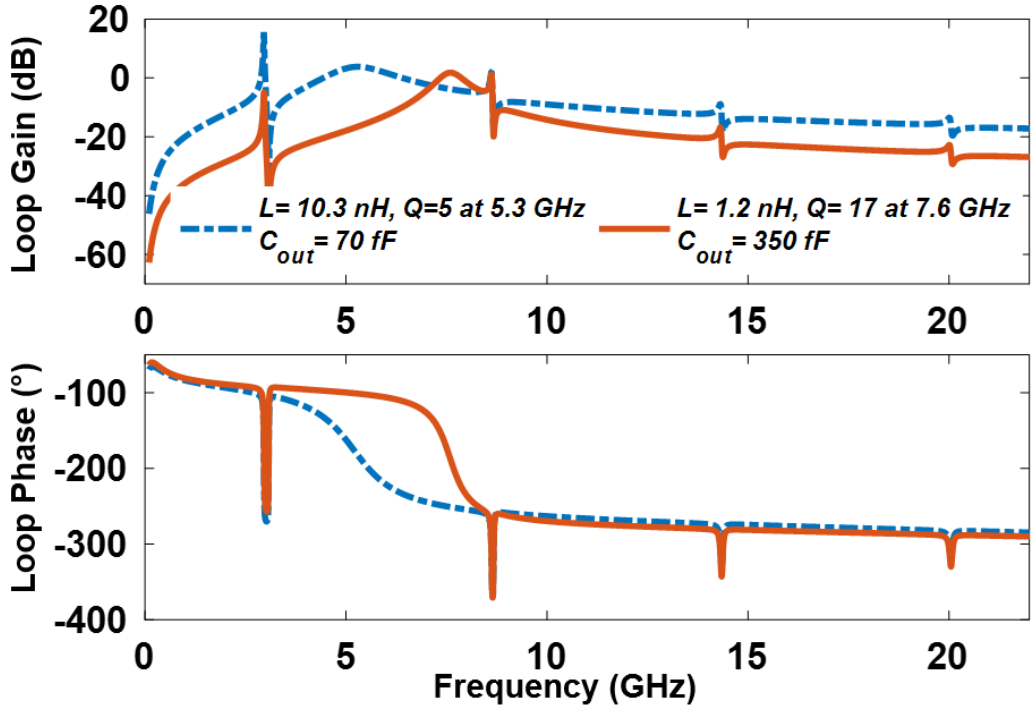

Fig. 5.4. Pierce loop gain for 2 different inductors [14].

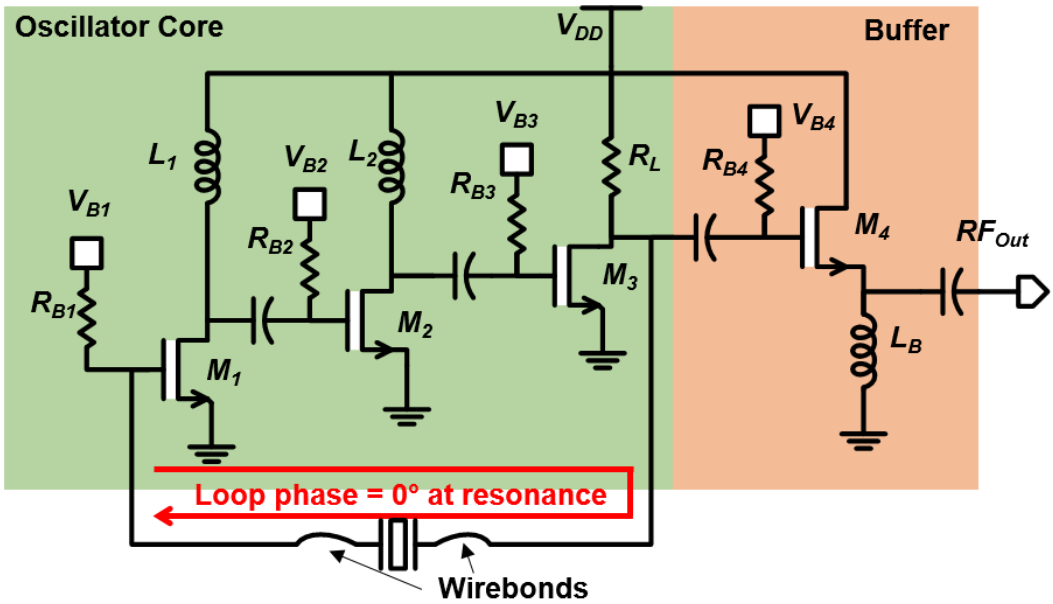

Fig. 5.5. Schematic of the 8.6 GHz oscillator core and buffer [14].

The modified Pierce loop gain response is shown in Figs. 5.3 and 5.4. It satisfies the oscillation conditions with a small gain and phase margins. Considering the fabrication, supply voltage, and temperature variations, in addition to post-layout parasitics, the single transistor oscillator would be impractical. Cascading amplifiers are adopted to have more control over the loop gain response, such as achieving a wide range of gain and phase margins. A second stage of inductively loaded CS would satisfy the oscillation conditions for A_1 and the inductor gain peak frequencies while suppressing the targeted mode.

Three inverting stages are adopted for our oscillator to excite A_3. The first and second stages are inductively loaded NMOS CS TAs. The third is a wideband resistive loaded NMOS CS stage that can operate as an amplifier or an attenuator by varying the gate voltage. The last stage controls the voltage swing available at the resonator port, ensuring the linear operation of the resonator. All stages are ac

coupled independently to provide the needed bias voltages for the transistors and low noise performance. The TA bandpass response is determined by the loading inductors (L_1 and L_2). The inductance values are chosen for a gain peak at 5.7 GHz, a frequency between A_1 (2.9 GHz) and A_3 (8.6 GHz). This bandpass response excites A_3 and suppresses A_1 and higher-order resonances. A low-power source-follower stage is used for 50-Ω-based measurements. The oscillator schematic is shown in Fig. 5.5.

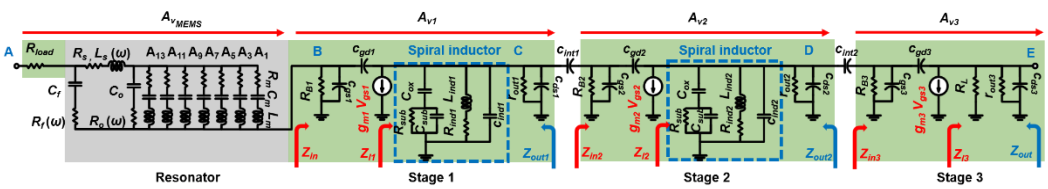

Fig. 5.6. Small signal model of the oscillator core [14].

5.3.2 Small-Signal Circuit Analysis

The circuit parameters for meeting Barkhausen's conditions are derived for fully understanding the oscillator. The process can identify the minimum dc power to start an oscillation and the exact frequency of oscillation. To this end, the oscillator loop is divided into four segments, as shown in Fig. 5.6, and the transfer function of each segment is analyzed. The loop can be divided at the drain node of M_3 shown in Fig. 5.5. The loading is represented by adding R_{load} resistor in series to the resonator, as shown in Fig. 5.6. The loop gain can be expressed as:

$$LG = A_{v_{mems}} \cdot A_{v1} \cdot A_{v2} \cdot A_{v3} \tag{5.1}$$

where A_{vmems}, A_{v1}, A_{v2}, and A_{v3} are given below:

$$A_{v_{mems}} = \frac{1/y_{in}}{1/y_{in} + Z_m + R_{load}} \tag{5.2}$$

$$A_{v1} = \frac{sc_{gd1} - g_{m1}}{sc_{gd1} + \frac{1}{r_{out1}} + sc_{ds1} + \frac{1}{z_{ind1}} + y_{in2}} \tag{5.3}$$

$$A_{v2} = \frac{sc_{gd2} - g_{m2}}{sc_{gd2} + \frac{1}{r_{out2}} + sc_{ds2} + \frac{1}{z_{ind2}} + y_{in3}} \tag{5.4}$$

$$A_{v3} = \frac{sc_{gd3} - g_{m3}}{sc_{gd3} + \frac{1}{r_{out3}} + sc_{ds3} + \frac{1}{R_L}} \tag{5.5}$$

where R_{load} is the loading resistance after breaking the loop. g_{m1}, g_{m2}, and g_{m3} are the transconductances of M_1, M_2, and M_3, respectively. c_{gd1}, c_{gd2}, and c_{gd3} are the gate-drain capacitances of M_1, M_2, and M_3, respectively. r_{out1}, r_{out2}, and r_{out3} are the output resistances of M_1, M_2, and M_3, respectively. c_{ds1}, c_{ds2}, and c_{ds3} are the drain-source capacitances of M_1, M_2, and M_3, respectively. R_L is the loading resistance of the third stage. z_{ind1}, z_{ind2} are the input impedances of L_1, and L_2 respectively, and are given as:

$$z_{ind1} = \left(\left((sL_{ind1} + R_{ind1})||\frac{1}{sC_{ind1}}\right) + \frac{1}{sC_{ox}}\right)||R_{sub}||\frac{1}{sC_{sub}} \tag{5.6}$$

$$z_{ind2} = \left(\left((sL_{ind2} + R_{ind2})||\frac{1}{sC_{ind2}}\right) + \frac{1}{sC_{ox}}\right)||R_{sub}||\frac{1}{sC_{sub}} \tag{5.7}$$

where L_{ind} is the self-inductance from the spiral metallization. R_{ind} is the ohmic loss from the finite conductance of the inductor metal. C_{ind} is the capacitance due to spiral inductor metals overlap. C_{ox} is the capacitance from the inductor metal to the

substrate. R_{sub} is the inductor ohmic losses due to eddy currents. C_{sub} is a fitting parameter. The resonator input impedance z_m is given as:

$$z_m = \left(\left(\left(\frac{1}{sC_m} + sL_m + R_m\right) || \left(R_o + \frac{1}{sC_o}\right)\right) + (R_s + sL_s)\right) || \left(R_f + \frac{1}{sC_f}\right) \qquad (5.8)$$

y_{in}, y_{in2}, and y_{in3} are the input admittances of the first, second, and third stage, respectively, and are given as:

$$y_{in} = \frac{1}{R_{B1}} + sc_{gs1} + sc_{gd1}\left(\frac{1 + \dfrac{g_{m1}}{\dfrac{1}{r_{out1}} + sc_{ds1} + \dfrac{1}{z_{ind1}} + y_{in2}}}{1 + \dfrac{sc_{gd1}}{\dfrac{1}{r_{out1}} + sc_{ds1} + \dfrac{1}{z_{ind1}} + y_{in2}}}\right) \qquad (5.9)$$

$$y_{in2} = \frac{1}{R_{B2}} + sc_{gs2} + sc_{gd2}\left(\frac{1 + \dfrac{g_{m2}}{\dfrac{1}{r_{out2}} + sc_{ds2} + \dfrac{1}{z_{ind2}} + y_{in3}}}{1 + \dfrac{sc_{gd2}}{\dfrac{1}{r_{out2}} + sc_{ds2} + \dfrac{1}{z_{ind2}} + y_{in3}}}\right) \qquad (5.10)$$

$$y_{in3} = \frac{1}{R_{B3}} + sc_{gs3} + sc_{gd3}\left(\frac{1 + \dfrac{g_{m3}}{\dfrac{1}{r_{out3}} + sc_{ds3} + \dfrac{1}{R_L}}}{1 + \dfrac{sc_{gd3}}{\dfrac{1}{r_{out3}} + sc_{ds3} + \dfrac{1}{R_L}}}\right) \qquad (5.11)$$

where R_{B1}, R_{B2}, and R_{B3} are the gate biasing resistances of M_1, M_2, and M_3, respectively. C_{gs1}, C_{gs2}, and C_{gs3} are the gate-source capacitances of M_1, M_2, and M_3, respectively. y_{out}, y_{out2}, and y_{out1} are the output admittances of the third, second, and first stage, respectively, and are given as:

$$y_{out} = \frac{1}{r_{out3}} + sc_{ds3} + \frac{1}{R_L} + sc_{gd3}\left(\frac{\frac{1}{R_{B3}} + sc_{gs3} + y_{out2} + g_{m3}}{\frac{1}{R_{B3}} + sc_{gs3} + y_{out2} + sc_{gd3}}\right) \tag{5.12}$$

$$y_{out2} = \frac{1}{r_{out2}} + sc_{ds2} + \frac{1}{z_{ind2}} + sc_{gd2}\left(\frac{\frac{1}{R_{B2}} + sc_{gs2} + y_{out1} + g_{m2}}{\frac{1}{R_{B2}} + sc_{gs2} + y_{out1} + sc_{gd2}}\right) \tag{5.13}$$

$$y_{out1} = \frac{1}{r_{out1}} + sc_{ds1} + \frac{1}{z_{ind1}} + sc_{gd1}\left(\frac{\frac{1}{R_{B1}} + sc_{gs1} + g_{m1}}{\frac{1}{R_{B1}} + sc_{gs1} + sc_{gd1}}\right) \tag{5.14}$$

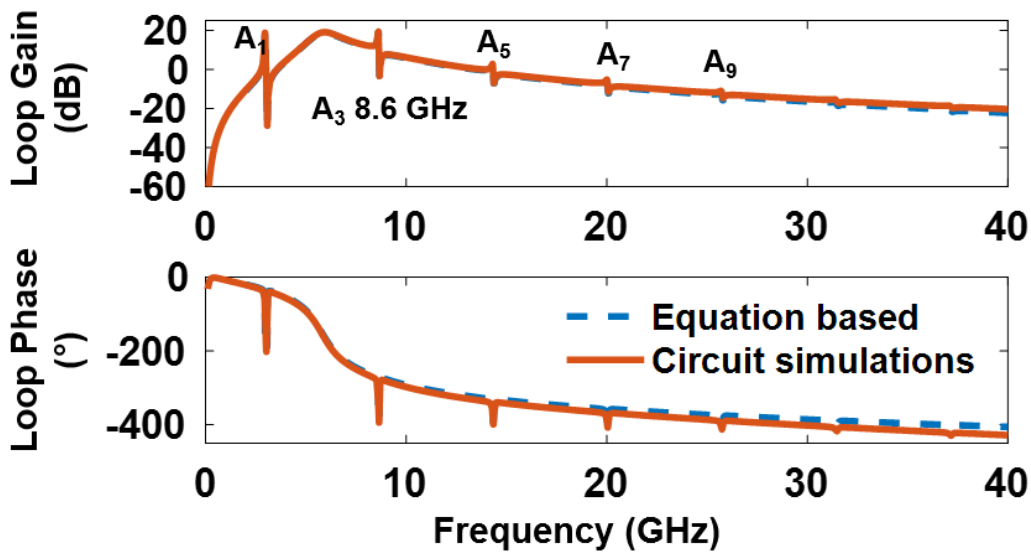

Fig. 5.7. Circuit-simulated and equation-predicted loop gain for the oscillator. Amplifier parameters used in these simulations: g_{m1} = 7.45 mS, g_{m2} = 16 mS, g_{m3} = 9.6 mS, r_{out1} = 4.4 kΩ, r_{out2} = 1.048 kΩ, r_{out3} = 128 Ω, C_{gs1} = 32 fF, C_{gs2} = 15 fF, C_{gs3} = 10 fF, C_{gd1} = 4.2 fF, C_{gd2} = 4 fF, C_{gd3} = 10 fF, C_{ds1} = 5 fF, C_{ds2} = 11 fF, C_{ds3} = 14 fF, R_{B1} = 10 kΩ, R_{B2} = R_{B3} = 2 kΩ, R_L = 400 Ω, L_{ind1} = L_{ind2} = 6.35 nH. [14].

The inter-stage coupling capacitances are designed to be large enough from affecting the signal transmission at 8.6 GHz. Hence, they are neglected in the above analysis. By solving for *abs*(*LG*) = 1 (or 0 dB), the minimal power consumption for

starting oscillations is estimated. Moreover, the frequency of oscillation is estimated by solving *phase*(LG) = 0. Results based on Equation (5.1) are shown along with circuit simulated outcome in Fig. 5.7. The parameters used in Equation (5.1) to generate Fig. 5.7 are given as follows: g_{m1} = 7.45 mS, g_{m2} = 16 mS, g_{m3} = 9.6 mS, r_{out1} = 4.4 kΩ, r_{out2} = 1.048 kΩ, r_{out3} = 128 Ω, C_{gs1} = 32 fF, C_{gs2} = 15 fF, C_{gs3} = 10 fF, C_{gd1} = 4.2 fF, C_{gd2} = 4 fF, C_{gd3} = 10 fF, C_{ds1} = 5 fF, C_{ds2} = 11 fF, C_{ds3} = 14 fF, R_{B1} = 10 kΩ, R_{B2} = R_{B3} = 2 kΩ, R_L = 400 Ω, and L_{ind1} = L_{ind2} = 6.35 nH. The above equations can guide the analysis of the oscillator small signal behavior independent of the employed IC technology.

5.3.3 Design for Phase Noise

The close-to-carrier noise adds directly to the system noise figure, while the far-from-carrier noise weakens the capability of a receiver to attenuate undesired adjacent channel signals. Both should be reduced in a sophisticated design. From the resonator standpoint, maximizing power dissipation in the motional branch ($P_m = R_m I_m^2$) of the resonator without exiting the linear regime (larger P_m reduces far-from- carrier phase noise) produces a better far-from-carrier noise. This can be guaranteed if most of the current passes through the motional arm at resonance (R_m) rather than the static arm (C_o). However, the oscillator should consume low power for battery-powered mobile applications, leading to the well-known trade-off between phase noise and power consumption. Resonators with a smaller R_m (thus, a larger resonator if FoM_{RES} is fixed [11]) are preferable for lower far-from-carrier noise. Also, doubling Q_m translates ideally to a lower-6 dB thermal phase noise.

The oscillator bias points, bias circuit design, and transistor flicker noise are all significant contributors to flicker noise. The amplifier should provide enough loop gain (*LG*) to satisfy Barkhausen's conditions only for A_3 while balancing noise performance and power consumption. To this end, M1, M2, and M3 have lengths of 240, 90, and 70 nm to reduce the impact of flicker noise. Bias voltages and transistor widths are optimized for both flicker and thermal noises with transconductance values given in Fig 5.7. The dc currents in M1, M2, M3, and the buffer are 2, 3.2, 2, and 3 mA, respectively, from a 1 V supply. L_1 and L_2 minimally affect resonator Q_l since their center frequencies are far from 8.6 GHz. Smaller loading resistance for M3 (R_L) translates to a better thermal phase noise yet more current consumption. Harmonic balance simulations show that M3 contributes to the noise at 1 kHz offset by 41%, M1 by 35%, and M2 by 20%. For the 1 MHz offset, the noise is dominated by R_m with 24%, M1 with 21%, and M3 with 5% of the total noise.

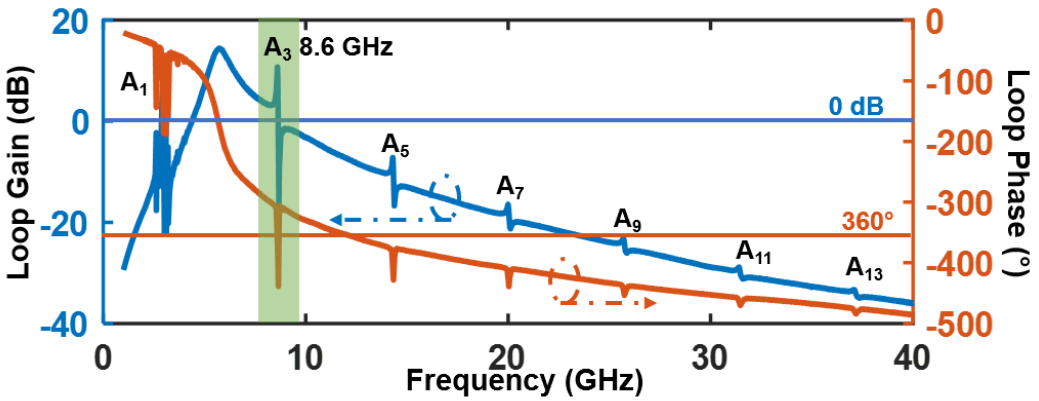

Fig. 5.8. Post-layout simulated loop gain and phase. Only the A_3 resonance satisfies Barkhausen's conditions of oscillation. Measured S-parameters of resonator A are used in this simulation [14].

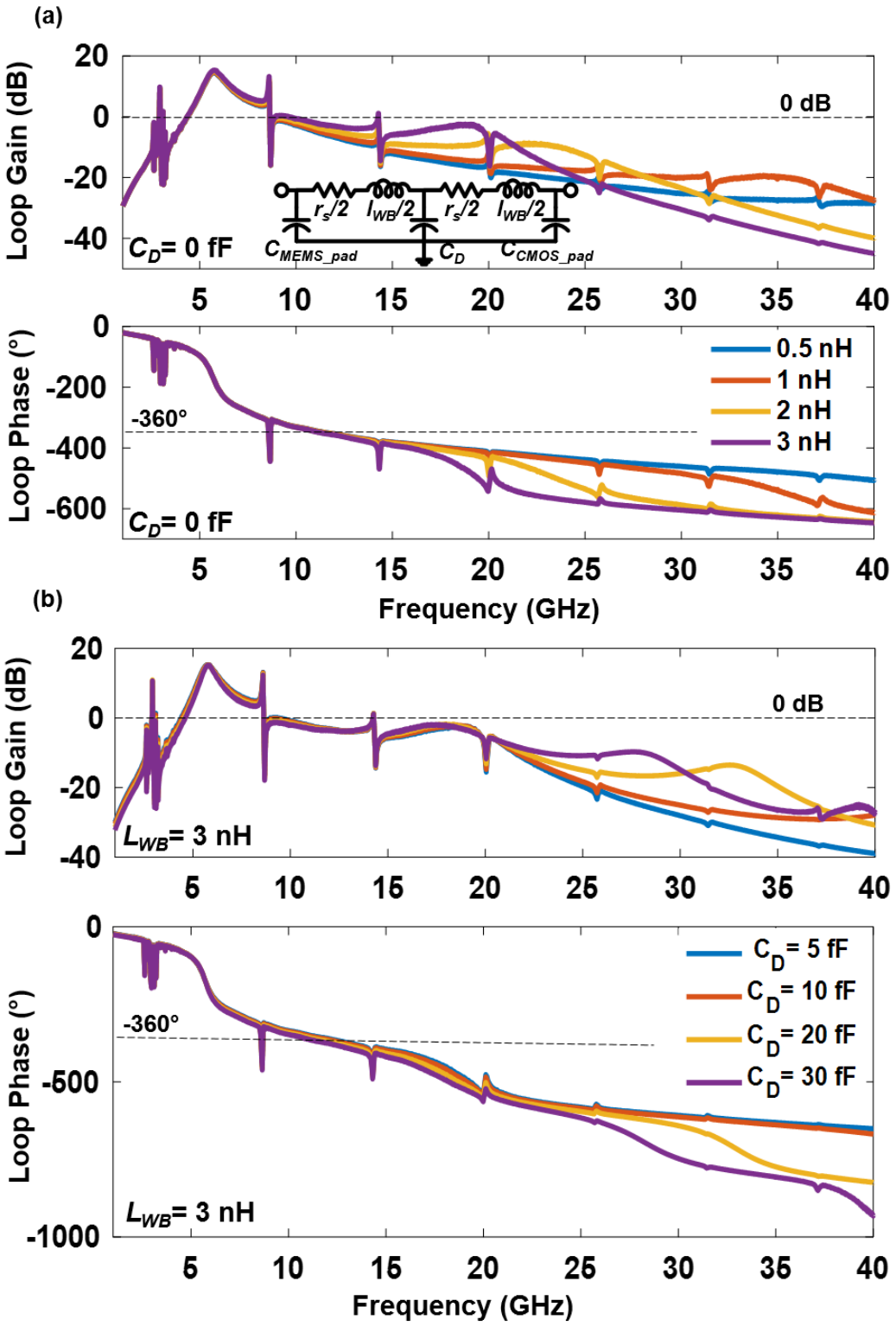

Fig. 5.9. Wire-bond effects on loop gain. (a) Variation of L_{WB} from 0.5 to 3 nH with Q of 30 where C_D = 0. (b) Variation of C_D from 5 to 30 fF where L_{WB} = 3nH [14].

5.3.4 Integration Effects

Figs. 5.8 and 5.9 show post layout stability simulations for the oscillator without and with wire-bonds effects, respectively. A parametric analysis of the impact of the wire-bond length on the oscillator loop gain was done using the wire-bond model shown in the inset of Fig. 5.9 (a). Apart from the wire inductances, the model includes three additional capacitances to the ground, C_D that captures the distributed capacitances effect over the wire length, and the bonding pads from the MEMS (C_{MEMS_pad}) and CMOS die (C_{CMOS_pad}). C_{MEMS_pad} is captured in the standalone resonator measurements, while the C_{CMOS_pad} is simulated in the CMOS circuitry. Wire-bonds Q of 30 is assumed in the simulations with different lengths. Fig. 5.9. (a) shows the effect of varying L_{WB} on the loop gain, while Fig. 5.9. (b) shows the impact of varying C_D on the loop gain. Integration parasitics did not affect the parallel resonant frequency (f_p) and only slightly lowered the series resonance frequency (f_s). Simulations showed that wire-bonds barely load the resonator, as long as the wire inductance gain peak happens far from 8.6 GHz. Phase noise can be recovered by increasing the gate voltage of M1, hence increasing the power consumption. Simulations showed an increase of less than 0.5 mW is needed for the 3 nH wire-bond case to retain the noise. This parametric study shows that the 8.6 GHz oscillations are resilient to wide variations in wire-bond length. Resonators are placed close to the edge of the MEMS chip to reduce the wire-bond lengths.

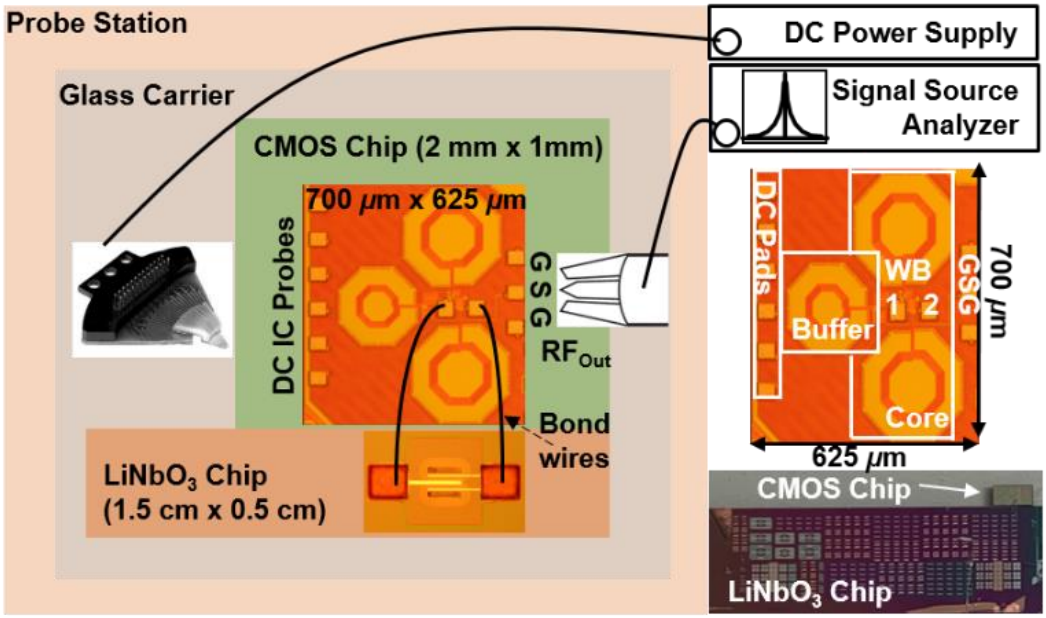

Fig. 5.10. Measurement setup [14].

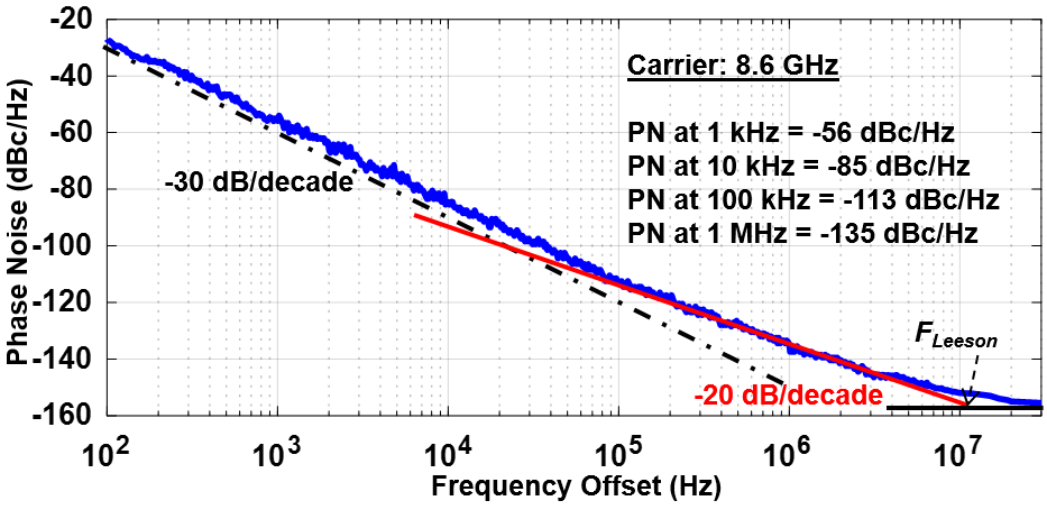

Fig. 5.11. Measured phase noise of the 8.6 GHz carrier [14].

5.3.5 *X*-Band Measurements

The TSMC RF GP 65 nm CMOS chip (2 mm × 1 mm) is integrated with the MEMS chip (1.5 cm × 0.5 cm) on a glass substrate via wire bonding. The CMOS circuitry occupying an area of 700 μm × 625 μm is integrated with resonator A as shown in Fig. 5.10. The oscillator is tested on a probe station where the output is

sensed using a 100 μm pitch GSG probe. DC probes with decoupling capacitors are used to deliver the transistor bias voltages. Probing was planned as the measurement method in the design stage to avoid complications from parasitic inductances added to L_1 and L_2. Phase noise measurements are taken using an R&S FSUP26 signal analyzer and reported in Fig. 5.11. The oscillator achieves measured phase noise of -56, -113, and -135 dBc/Hz at 1 kHz, 100 kHz, and 1 MHz offsets from an 8.6 GHz carrier while consuming 10.2 mW of dc power. From Fig. 5.11, Leeson frequency can be estimated to be around 12 MHz, suggesting a measured loaded Q of 358. This value is lower than the reported value in Fig. 5.1 due to the integration and circuit loading effects.

5.4 *L*-BAND OUTPUT

The *X*-band oscillator wire-bonded to resonator B is followed by a single-ended-to-differential output stage for conditioning the signals before entering the frequency divider. The inputs to the frequency dividers can be level-shifted through the V_{CM} input shown in Fig. 5.12 (a). The frequency dividers used are simple current mode logic (CML) dividers that operate with moderate input and output swings and very high speeds in submicron CMOS [128]. A divide-by-8 circuitry is needed to convert the 8.6 GHz RF-MEMS output to 1.1 GHz output. Hence, division-by-8 is achieved through three stages of divide-by-2 circuitry. As shown in Fig. 5.12 (b), the divide-by-2 circuit is created by placing two D-latches in a negative feedback loop.

The frequency divider derives its speed from the fact that a differential pair can be quickly enabled and disabled through its tail current source. The design has

several metrics, such as the clocking speed that halves after each division, the power budget, and the phase noise. The close-in phase noise of the 1.1 GHz output is limited by the flicker noise generated by the 8.6 GHz oscillator transistors. In contrast, the far-out noise is limited by the last divider stage and the CMOS inverters following it. The total dc power consumption of the *L*-band circuitry is 12 mW, where the oscillator consumes 6.9 mW and the dividers consume 5.1 mW. In the current chip, the three divider cells are a replica. Power consumed in the divider can be greatly reduced by at least halving the power of each following stage as the clocking speed halves.

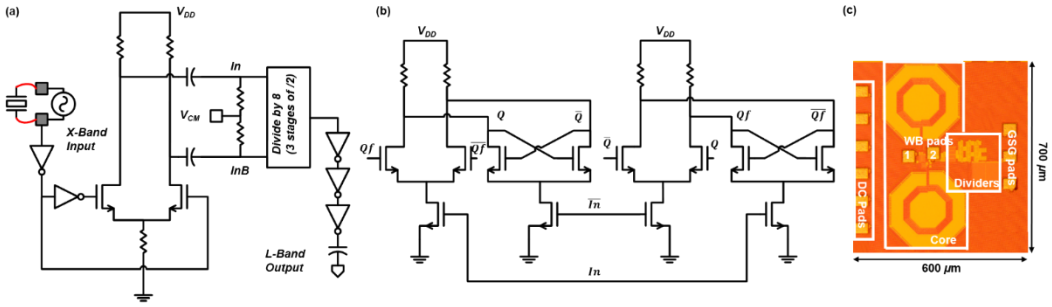

Fig. 5.12 (a) L-band output from X-band RF-MEMS oscillator. (b) Divide-by-2 stage. (c) Oscillator-dividers CMOS die [14].

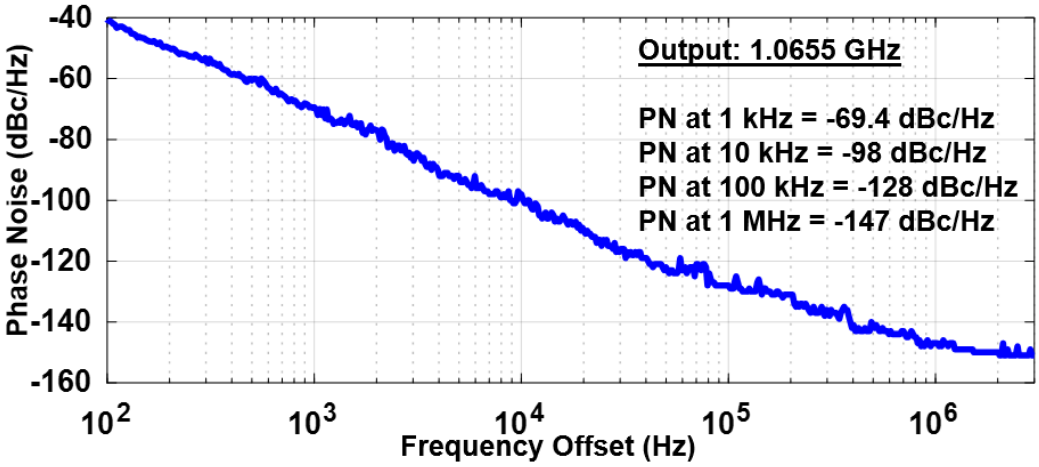

Fig. 5.13. Measured phase noise of the 1.07 GHz output [14].

Simulations show that the oscillator-divider interface realized through the squarer (buffer inverters following the oscillator) and the single-to-differential circuitry are noisier than the first two high-speed divider stages. This signal preconditioning is crucial for a stable division. The far-from-carrier noise is limited by the last divider stage (lowest speed) and the following CMOS inverters.

Table 5.1. Noise Contribution of the Interface Circuitry and Frequency Dividers for the 1.1 GHz Output

Offsets (kHz)	1	10	100	1000
Measured phase noise at 8.6 GHz (dBc/Hz)	-56	-85	-113	-135
Measured phase noise at 1.1 GHz (dBc/Hz)	-69.4	-98	-128	-147
Phase noise at 8.6 GHz – 20*log(8) (dBc/Hz)	-74.1	-103	-131	-153
Delta (dB)	4.7	5	3	6

Table 5.2. Comparison to the SoA RF-Mems Oscillators above 5 GHz

		This work [14]	[15]	[117]	[118]	[119]
Resonator		**$LiNbO_3$ A_3**	$LiNbO_3$ A_3	FBAR fundamental	FBAR fundamental	FBAR 3rd tone
IC Process		**65 nm CMOS**	Discrete	0.35 μm BiCMOS	Discrete	Discrete
Osc. Freq. (GHz)		**8.6**	12.9	5.46	5	7
Resonator Footprint (mm^2)		**0.016**	0.01	0.034	> 0.1	-
Q_l		**384**	270	300#	300	1350
k_t^2 (%)		**2.2**	1.9	6.67#	4.3	-
FoM_{RES}		**8.4**	5.1	20	12.9	-
dc Power (mW)		**10.2**	20	12.7	-	16.2
PN (dBc/Hz)	1 kHz	**-56**	-70	-64^	-	-
			-73.5	-60	-	-
	100 kHz	**-113**	-111	-117.7	-109.5	-80
			-114.5	-113.8	-104.8	-78.2
	1 MHz	**-135**	-131	-	-	-110
			-134.5	-	-	-108.2
FoM_{Osc} (dB)	100 kHz	**201.6**	200.2	201.4	-	164.8

The values in the shaded cells are referenced to an 8.6 GHz output. # as reported in [120]. ^ value estimated from a plot in [117].

Table 5.3. Comparison to the SoA EM Oscillators

		This work [14]	[105]			[103]	[104]	[102]
Resonator		**$LiNbO_3$**	DRO			µstrip	Active	LC
IC Process		**65 nm CMOS**	GaN	GaAs	SiGe	BJT	Discrete	BiCMOS
Osc. Freq. (GHz)		**8.6**	10.6			10	10	15
Resonator Footprint (mm^2)		**0.016**	-			-	-	-
Q_l		**384**	600			-	1211	-
dc Power (mW)		**10.2**	-			200	500	72
PN (dBc/Hz)	1 kHz	**-56**	-53††	-76††	-90††	-65†	-	-
			-54.8	-77.8	-91.8	-66.3		
	100 kHz	**-113**	-118	-123	-135	-113	-114.4	-102*
			-119.8	-124.8	-136.8	-114.3	-115.7	-106.8
FoM_{Osc} (dB)	100 kHz	**201.6**	-			190	187.4	187

The values in the shaded cells are referenced to an 8.6 GHz output. †† values are estimated from a plot in [105]. † values are estimated from a plot in [103]. *values are estimated from a plot in [102].

Table 5.4. Comparison to the SoA PLLs above 5 GHz

		This work [14]	[121]	[122]	[123]	[124]
Architecture		**RF-MEMS Oscillator**	LC-PLL	LC-ADPLL	LC-ILCM	Digital ILCM
IC Process CMOS		**65 nm**	180 nm	65 nm	65 nm	65 nm
Output Freq. (GHz)		**8.6**	9.75	8.58	6.8	8
Reference Freq. (MHz)		**-**	Using off-shelf signal generators. Not XOs			
			12.5	276.8	106.25	125
IC Footprint (mm^2)		**0.4375**	0.678	0.18	0.25	0.27
dc Power (mW)		**10.2**	24	14.8	2.25	3.25
PN (dBc/Hz)	100 kHz	**-113**	-66.11	-	-111	-109.6
	1 MHz	**-135**	-89.8	-105	-113.5	-115
FoM_{OSC} (dB)	1 MHz	**203.6**	155.8	172	186.6	187.9

A noiseless divide-by-2 circuit can enhance the phase noise by 6 dB. With a noiseless divide-by-8, the noise at 1 kHz offset from a 1.1 GHz output should be ideally around -74 dBc/Hz, better than the measured value by 4.7 dB (extra noise from the 3-stage dividers and oscillator-divider inter-stage circuitry). Table 5.1

shows the noise contribution of the interface circuitry and frequency dividers for the 1.1 GHz output.

The *L*-band measurement setup is identical to the *X*-band setup. The die photo of the oscillator-divider chain is shown in Fig. 5.12 (c) with an active area of 600 x 700 μm. The measured *L*-band phase noise using resonator B is shown in Fig. 5.13. The synthesizer achieves phase noise of -69.4 and -147 dBc/Hz at 1 kHz and 1 MHz offsets, respectively, from a 1.07 GHz output.

Table 5.5. Comparison to the SoA *L*-Band PLLs

		This work	[125]	[126]
Architecture		**RF-MEMS Oscillator**	Ring IL-PLL	Ring ILCM
IC Process CMOS		**65 nm**	130 nm	65 nm
Output Freq. (GHz)		**1.07**	1.1	1.2
Reference Freq. (MHz)		**-**	Using off-shelf signal generators. Not XOs	
			50	120
IC Footprint (mm^2)		**0.42**	0.18	0.06
dc Power (mW)		**12**	13.5	9.5
PN (dBc/Hz)	1 MHz	**-147**	-121	-134.4
FoM_{OSC} (dB)	1MHz	**196.8**	170.5	186.2

5.5 CONCLUSIONS

In comparison to the *X*-band oscillators in Tables 5.2 and 5.3, the figure-of-merit (FoM_{OSC}) of our oscillator surpasses those of the SoA EM and RF-MEMS oscillators above 5 GHz. Moreover, the measured oscillation frequency is the highest reported to date for a MEMS oscillator wire-bonded to CMOS. In

comparison to the SoA X-band PLLs in Table 5.4, the reported 8.6 GHz RF-MEMS oscillator surpasses their phase noise and FoM_{OSC} results.

Table 5.6. Comparison to the SoA *L*-Band RF-MEMS Oscillators

		This work [14]	[129]	[130]	[131]	[132]	[133]	[134]	[135]
Resonator		**$LiNbO_3$**	FBAR	FBAR	AlN-on-Si CMR	GaN CMR	AlN CMR	AlN CMR	AlN SMR
IC Process		**65 nm CMOS**	0.35 μm CMOS	130 nm CMOS	180 nm CMOS	1 μm GaN	0.5 μm CMOS	130 nm CMOS	BiCMOS
Osc. Freq. (GHz)		**8.6**	1.5	2	1	1	1.05	1.16	2
Q_l		**370**	742	-	7100	4250	1450	3700	700
k_t^2 (%)		**2.1**	-	-	-	0.24	1.2	0.99	0.6
FoM_{RES}		**7.7**	-	-	-	10.2	17.4	36.63	4.2
dc Power (mW)		**12**	1.03	0.126	7.2	4.71	3.5	4.2	4.05
Multiple Frequency Outputs		**Yes 8.6, 4.3*, 2.15*, 1.07**	No	No	No	No	No	No	No
PN (dBc/Hz)	1 kHz	**-69.4****	-86	-	-94	-75	-81	-82.3	-73 †††
	1 MHz	**-147****	-147	-149	-150 †	-141	-146	-173.3	-137 †††
FoM_{OSC} (dB)	1 MHz	**196.8**	210.4	224	201.4	194.3	201	228.4	196.9

* There are no output pads for measuring the spectrums of the 4.3 and 2.15 GHz carriers, but the work can be expanded to include output nodes for these two frequencies. ** Phase noise values measured at 1.07 GHz output. † value estimated from a plot in [131]. †† value estimated from a plot in [135].

By tuning the inductive loads (L_1, and L_2) to smaller values, the same oscillator topology can be used to excite higher-order resonances. Moreover, adding a switchable capacitor bank parallel to L_1/ L_2 or using a switchable inductor bank can enable the oscillator to hop among different overtones rather than generate a fixed frequency output. Hence, this approach also allows for a potentially ultra-wideband tunable frequency generation.

In comparison to the SoA *L*-band PLLs in Table 5.5, our synthesizer surpasses their phase noise and FoM_{OSC} results. This proves our claim that a direct frequency synthesizer based on a high *Q* RF-MEMS oscillator and open-loop dividers can be more beneficial than a PLL referenced to a low-frequency stable source.

In comparison to the *L*-band RF-MEMS oscillators [129]-[135] in Table 5.6, our synthesizer with 2 (potentially 4) frequency outputs achieves competitive phase noise results at 1 MHz offset from a 1.1 GHz output. To improve the close-in phase noise for *L*-band and make it more competitive with prior arts, either increasing the resonator Q_l or choosing a lower flicker IC technology for integration (or both) should be considered. A resonator with a Q_l of 4000 at 8.6 GHz would ideally result in a phase noise around -95 dBc/Hz at 1 kHz offset from 1.1 GHz output using the same active circuitry. Such higher Q_l (11 times fold) would also decrease the resonator motional resistance, leading to better phase noise at 1 MHz offset and lower power consumption. The higher *Q* can be potentially achieved by improving the resonator thin-film quality, using metals with lower mechanical losses for electrodes or SiC or sapphire as a substrate to reduce dielectric loss. For our previous discrete version that uses a similar resonator at the *Ku*-band, reported in Chapter 4, increasing the resonator Q_l from 270 to 432 (1.6 times) at 12.9 GHz would surpass the -95 dBc/Hz phase noise level at 1 kHz offset from a 1.1 GHz output. Thus, it is more practical to use a low-flicker transistor technology like SiGe rather than improving the resonator Q_l solely. Moreover, injection-locked dividers can minimize the power consumption and the phase noise of the high-frequency

dividers, despite trading off the form factor. Other topologies for building the core oscillator, such as cross-coupled differential pairs, might be considered to reduce the power consumption further.

CHAPTER 6: SUMMARY AND FUTURE WORK

6.1 SUMMARY

The presented work focuses on the design and implementation of $LiNbO_3$ RF-MEMS oscillators for IoT, 5G and beyond. $LiNbO_3$ resonators characterized by high Q, high k_t^2, and high FoM are crucial for building high-performance acoustic oscillators. $LiNbO_3$ RF-MEMS oscillators can be enabled with lower power consumption, wider tuning ranges, and a higher frequency of oscillation when compared to other RF-MEMS oscillators.

The presented work addresses two main oscillator specifications: enabling wider tuning ranges for IoT, and higher frequency of oscillation for 5G and beyond. Wide tuning ranges were enabled by the oscillators presented in Chapters 2 and 3, while the multi-GHz high Q oscillators were discussed in Chapters 4 and 5.

Chapter 2 presents the first VCMO based on the heterogeneous integration of a high Q $LiNbO_3$ resonator and CMOS. A $LiNbO_3$ resonator array with a series resonance of 171.1 MHz, a Q of 410, and a k_t^2 of 12.7% was adopted, while the TSMC 65 nm RF LP CMOS technology was used to implement the active circuitry. The measured best phase noise performances of the VCMO are -72 and -153

dBc/Hz at 1 kHz and 10 MHz offsets from 178.23 and 175.83 MHz carriers, respectively. The VCMO consumes a dc power of 72 μW while realizing a tuning range of 2.4 MHz (~ 1.4% fractional tuning range).

Chapter 3 presents the first VCMO based on $LiNbO_3$ LOBAR. The proposed VCMO is capable to lock to ten overtones ranging from 300 to 500 MHz. These ten tones are characterized by average *Q*s of 2100, k_t^2 of 1.5%, and FoMs of 31.5. The measured VCMO shows a close-in phase noise of -100 dBc/Hz at 1 kHz offset from a 300 MHz carrier and a noise floor of -153 dBc/Hz while consuming 9 mW.

Chapter 4 presents the first *Ku*-band RF-MEMS oscillator. The oscillator achieves measured phase noise of -70 and -111 dBc/Hz at 1 kHz and 100 kHz offsets from a 12.9 GHz carrier while consuming 20 mW of dc power. The oscillator achieves a FoM_{OSC} of 200 dB at 100 kHz offset. The achieved oscillation frequency is the highest reported to date for a MEMS oscillator.

Chapter 5 presents the first *X*-band RF-MEMS oscillator built using CMOS technology. The oscillator achieves measured phase noise of -56, -113, and -135 dBc/Hz at 1 kHz, 100 kHz, and 1 MHz offsets from an 8.6 GHz output while consuming 10.2 mW of dc power. The oscillator also attains a FoM_{OSC} of 201.6 dB at 100 kHz offset, surpassing the SoA EM and RF-MEMS based oscillators, and *X*-band PLLs. A frequency divider is implemented to produce an *L*-band output from the 8.6 GHz oscillator. Phase noise of -69.4 and -147 dBc/Hz at 1 kHz and 1 MHz

offsets from a 1075 MHz output is reported while consuming 12 mW of dc power. The phase noise performance also surpasses the SoA *L*-band PLLs.

6.2 FUTURE WORK

The work can be extended to study the effect of the $LiNbO_3$ resonator volume on the phase noise, tuning range, and power consumption of microwave oscillators. Smaller resonators are critical for microwave and mm-wave oscillators because of their smaller C_o as previously discussed in Chapters 4 and 5. However, smaller resonators are usually accompanied by larger mechanical losses at resonance, R_m. A parametric study is needed to evaluate the resonator design space for targeting high FoM oscillators.

Moreover, the work can be extended to serve the mm-wave 5G timing needs by enabling ultralow-power low-noise direct RF synthesizers. Scaling up the frequency of oscillation from 13 GHz to 28 GHz will serve the purpose. Open loop frequency division can be enabled to serve lower frequency wireless applications.

The oscillator temperature stability is very critical for wireless communications as previously discussed in Chapter 1. $LiNbO_3$ resonators exhibit a first-order TCF of -60 ppm/˚C, which is insufficient for high-performance timing applications. A passive temperature compensation (TC) technique using a layer of SiO_2 with positive TCF can be applied to the resonator stack. A first-order TCF <0.5 ppm/˚C can be achieved at room temperature after optimization. In addition to the passive TC, active compensation will be required; the resonator can be equipped with a thermistor (as shown in Fig. 6.1) to detect the operating

temperature of the resonator and relay the temperature to a CMOS temperature-to-digital converter that feeds compensation circuitry and a frequency tuning mechanism. Through the combination of active and passive techniques, the temperature stability is expected to be reduced to <1 ppm across industrial temperature ranges.

A 5G system-level study (from antennas to modems) would be beneficial to fully understand the merits of acoustic oscillators in these systems. Longer battery life, higher data rates, lower EVMs and smaller form factor are all envisioned. A quantitative study is needed to prove the above claims.

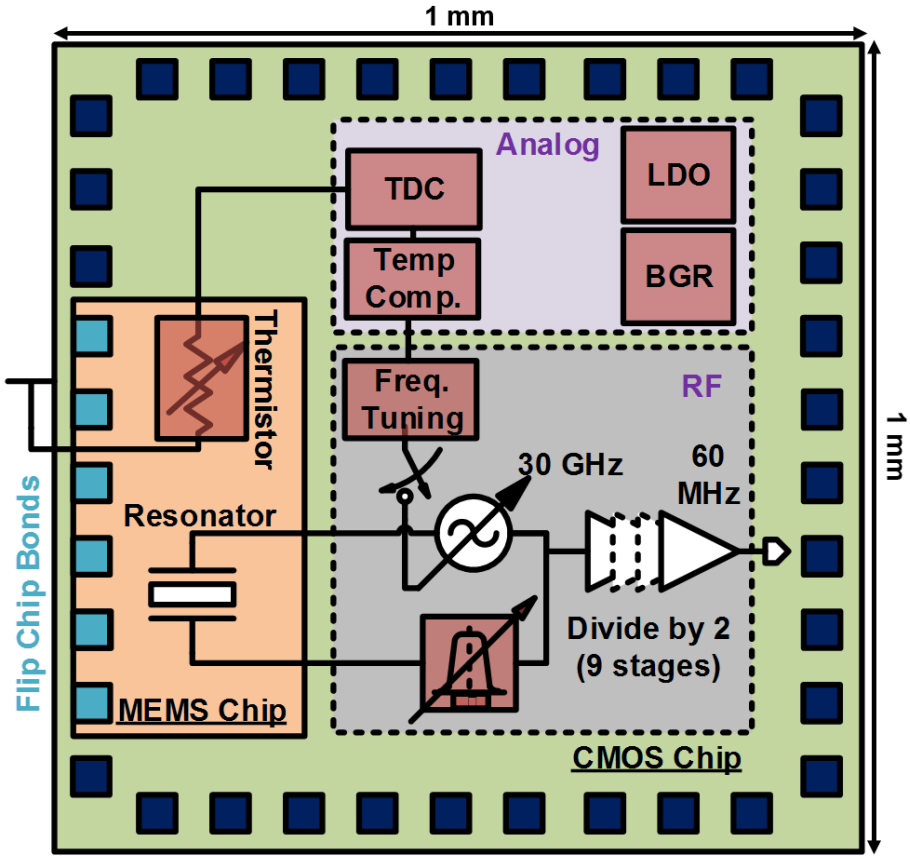

Fig. 6.1. Schematic of the proposed system for future investigation.

REFERENCES

[1] Yole development, “Status of the MEMS Industry,” 2018, [online].

[2] Yole development, “Status of the MEMS Industry,” 2010, [online].

[3] C. T.-C. Nguyen, “iMEMS’01 Short Course: RF MEMS for Wireless Communications” [online].

[4] R. Thirunarayanan, D. Ruffieux, and C. Enz, “Reducing energy dissipation in ULP systems: PLL-free FBAR-based fast startup transmitters,” *IEEE Trans. Microw. Theory Tech*., vol. 63, no. 4, pp. 1110–1117, April 2015.

[5] P.-E. Su, and S. Pamarti, “Fractional-N phase-locked-loop-based frequency synthesis: A tutorial,” *IEEE Trans. Circuits and Systems—II: Express Briefs*, vol. 56, no. 12, pp. 881-885, Dec. 2009.

[6] C.-M. Hsu, M. Z. Straayer, and M. H. Perrott, “A Low-noise wide-BW 3.6-GHz digital fractional-N frequency synthesizer with a noise-shaping time-to-digital converter and quantization noise cancellation,” *IEEE J. Solid-State Circuits*, vol. 43, no. 12, pp. 2776-2786, Dec. 2008.

[7] J. J. McCue, B. Dupaix, L. Duncan, B. Mathieu, S. McDonnell, V. J. Patel, T. Quach, and W. Khalil, “A time-interleaved multimode ΔΣ RF-DAC for direct digital-to-RF synthesis,” *IEEE J. Solid-State Circuits*, vol. 51, no. 5, pp. 1109-1124, May 2016.

[8] A. Jerng and C. G. Sodini, “A wideband ΔΣ digital-RF modulator for high data rate transmitters,” *IEEE J. Solid-State Circuits*, vol. 42, no. 8, pp. 1710–1722, Aug. 2007.

[9] Partridge, H.-C. Lee, P. Hagelin, and V. Menon, “We know that MEMS is replacing quartz. But why? And why now?” *IEEE Joint Euro. Freq. and Time Forum & Int. Freq. Control Symp. (EFTF/IFCS)*, July 2013, pp.1-6.

[10] T.-C. Nguyen, “MEMS technology for timing and frequency control,” *IEEE Trans. Ultrason, Ferroelectr., Freq. Control*, vol. 54, no. 2, pp. 251-269, Feb. 2007.

[11] A. Kourani, and S. Gong, “A tunable low power oscillator based on high *Q* lithium niobate MEMS resonators and 65 nm CMOS,” *IEEE Trans. Microw. Theory Techn.*, vol. 66, no. 12, pp. 5708-5723, Dec. 2018 (IMS 2018 special issue).

[12] A. Kourani, and S. Gong, "The design and analysis of a wideband oscillator exploiting multiple overtones in single lithium niobate MEMS resonator," *IEEE Trans. Ultrason., Ferroelectr., Freq. Control T-UFFC.*, vol. 67, no. 9, pp. 1854-1866, Sept. 2020.

[13] A. Kourani, Y. Yang, and S. Gong "A ku-band oscillator utilizing overtone lithium niobate RF-MEMS resonator for 5G," *IEEE Microw. and Wireless Components Letters MWCL*, vol. 30, no. 7, pp. 681-684, July 2020.

[14] A. Kourani, Y. Yang, and S. Gong, "An L-and-X band dual frequency synthesizer utilizing lithium niobate RF-MEMS and open loop frequency dividers," *IEEE Trans. Ultrason., Ferroelectr., Freq. Control TUFFC*, doi: 10.1109/TUFFC.2020.3048929.

[15] J. H. Kuypers, et al. "Wafer-level chip scale MEMS oscillator for wireless applications," *IEEE Freq. Control Symp*., 2012.

[16] T. H. Lee, and A. Hajimiri, "Oscillator phase noise: A tutorial," *IEEE J. Solid-State Circuits*, vol. 35, no. 3, pp. 326-336, 2000.

[17] U. L. Rhode, *Microwave and Wireless Synthesizers: Theory and Design*, John Wiley and Sons, 1997.

[18] D. B. Leeson, "A simple model of feedback oscillator noise spectrum," *Proc. IEEE*, vol. 54, no. 2, pp. 329–330, Feb. 1966.

[19] G. Piazza, P. Stephanou, and A. Pisano, "Piezoelectric aluminum nitride vibrating contour-mode MEMS resonators," *IEEE J. Microelectromech. Syst.*, vol. 15, no. 6, pp. 1406–1418, Dec. 2006.

[20] E. Vittoz, *Low-power Crystal and MEMS Oscillators. The Experience of Watch Developments*, Springer Integrated Circuits and Systems, 2010.

[21] K. Sundaresan, G. Ho, S. Pourkamali, and F. Ayazi, "Electronically temperature compensated silicon bulk acoustic resonator reference oscillators," *IEEE J. Solid-State Circuits*, vol. 42, no. 6, pp. 1425–1434, June 2007.

[22] Y.-W. Lin, S. Lee, S.-S. Li, Y. Xie, Z. Ren, and C. Nguyen, "Series-resonant VHF micromechanical resonator reference oscillators," *IEEE J. Solid-State Circuits*, vol. 39, no. 12, pp. 2477–2491, Dec. 2004.

[23] T. Naing, T. Rocheleau, Z. Ren, S.-S. Li, and C. Nguyen, "High-*Q* UHF spoke-supported ring resonators," *IEEE J. Microelectromech. Syst.*, vol. 25, no. 1, pp. 11–29, Feb. 2016.

[24] S. Pourkamali, A. Hashimura, R. Abdolvand, G. Ho, A. Erbil, and F. Ayazi, "High-*Q* single-crystal silicon HARPSS capacitive beam resonators with self-aligned sub-100-nm transduction gaps," *IEEE J. Microelectromech. Syst.*, vol. 12, no. 4, pp. 487–496, Aug. 2003.

[25] J. Nilchi, R. Liu, and C. Nguyen, "High Cx/Co 13 nm-capacitive-gap transduced disk resonator," *Proc. IEEE Int. Conf. Micro Electro Mech. Syst. (MEMS)*, 2017.

[26] K. Hashimoto, *RF Bulk Acoustic Wave Filters for Communications*. Norwood, MA, USA: Artech House, 2009.

[27] R. Ruby, "FBAR — from technology development to production," in *Second International Symposium on Acoustic Wave Devices for Future Mobile Communication Systems*, 2004.

[28] R. Ruby, P. Bradley, J. Larson, Y. Oshmyansky, and D. Figueredo, "Ultra-miniature high-filters and duplexers using FBAR technology," *IEEE Int. Solid-State Circuits Conf. (ISSCC) Dig. Tech.*, 2001.

[29] Q.-X. Su, P. Kirby, E. Komuro, M. Imura, Q. Zhang, and R. Whatmore, "Thin-film bulk acoustic resonators and filters using ZnO and lead zirconium-titanate thin films," *IEEE Trans. Microw. Theory Tech.*, vol. 49, no. 4, pp. 769–778, Apr. 2001.

[30] S. Rai, and B. Otis, "A 1 V 600 μW 2.1 GHz quadrature VCO using BAW resonators," *IEEE Int. Solid-State Circuits Conf. (ISSCC) Dig. Tech.*, 2007.

[31] K. Ostman, S. Sipila, I. Uzunov, and N. Tchamov, "Novel VCO architecture using series above-IC FBAR and parallel LC resonance," *IEEE J. Solid-State Circuits*, vol. 41, no. 10, pp. 2248–2256, June 2007.

[32] M. Nagaraju, K. Sankaragomathi, S. Gilbert, B. Otis, and R. Ruby, "A low noise 1.5 GHz VCO with a 3.75% tuning range using coupled FBARs," *Proc. IEEE Ultrason. Symp.*, 2012.

[33] J. Shi, B. Otis, "A sub-100 μW 2 GHz differential Colpitts CMOS/FBAR VCO," *IEEE Custom Integrated Circuits Conf.*, 2011.

[34] T. Kimura, M. Kadota, and Y. Ida, "High *Q* SAW resonator using upper electrodes on grooved-electrodes in $LiTaO_3$," *IEEE MTT-S Int. Microw. Symp. Dig.*, 2010.

[35] K. Hashimoto, *Surface Acoustic Wave Devices in Telecommunications*. Berlin, Germany: Springer-Verlag, 2000.

[36] M. Rinaldi, C. Zuniga, C. Zuo, and G. Piazza, "Super-high-frequency two-port AlN contour-mode resonators for RF applications," *IEEE Trans. Ultrason. Ferroelectr. Freq. Control*, vol. 57, no. 1, pp. 38–45, Jan. 2010.

[37] X. Wu, C. Zuo, M. Zhang, J. Spiegel, and G. Piazza, "A 47 μW 204 MHz AlN contour-mode MEMS based tunable oscillator in 65 nm CMOS," *IEEE Int. Symp. Circuits and Systems*, 2013.

[38] C. Zuo, J. Spiegel, and G. Piazza, "1.5-GHz CMOS voltage-controlled oscillator based on thickness-field-exited piezoelectric AlN contour-mode MEMS resonators," *IEEE Custom Integrated Circuits Conf.*, 2010.

[39] H. Lavasani, W. Pan, B. Harrington, R. Abdolvand, and F. Ayazi, "Electronic temperature compensation of lateral bulk acoustic resonator reference oscillators using enhanced series tuning technique," *IEEE J. Solid-State Circuits*, vol. 47, no.6, pp.1381- 1393, June 2012.

[40] H. Lavasani, W. Pan, B. Harrington, R. Abdolvand, and F. Ayazi, "A 76 dB Ω 1.7 GHz 0.18 mm CMOS tunable TIA using broadband current pre-amplifier for high frequency lateral MEMS oscillator," *IEEE J. Solid-State Circuits,* vol. 46, no. 1, pp. 224- 235, Jan. 2011.

[41] A. Kourani, E. Hegazi, and Y. Ismail, "A 76.8 MHz temperature compensated MEMS reference oscillator for wireless handsets," *J. Microelectronics,* vol. 46, no. 6, pp. 496–505, April 2015.

[42] A. Kourani, E. Hegazi, and Y. Ismail, "Electronic frequency compensation of AlN-on-Si MEMS reference oscillators," *J. Microelectronics,* vol. 54, pp. 73–84, June 2016.

[43] Z. Wu *et al.*, "Piezoelectrically transduced high-*Q* silica microresonators," *Proc. IEEE Int. Conf. Micro Electro Mech. Syst. (MEMS),* Jan. 2013.

[44] A. Ansari and M. Rais-Zadeh, "A temperature-compensated gallium nitride micromechanical resonator," *IEEE Electron Device Lett.,* vol. 35, no. 11, pp. 1127–1129, Nov. 2014.

[45] L. Popa, and D. Weinstein, "L-band Lamb mode resonators in gallium nitride MMIC technology," *Proc. IEEE Int. Freq. Control Symp.,* May 2014.

[46] J. Pulskamp *et al.*, "Piezoelectric PZT MEMS technologies for small-scale robotics and RF applications," *MRS Bull.,* vol. 37, no. 11, pp. 1062 1070, Nov. 2012.

[47] R. Abdolvand, H. M. Lavasani, G. K. Ho, and F. Ayazi, "Thin-film piezoelectric-on-silicon resonators for high frequency reference oscillator applications," *IEEE Trans. Ultrason. Ferroelectr. Freq. Control*, vol. 55, no. 12, pp. 2596–2606, Dec. 2008.

[48] S. S. Bedair, J. S. Pulskamp, R. Rudy, R. Polcawich, R. Cable and L. Griffin, "Boosting MEMS piezoelectric transformer figures of merit via architecture optimization," *IEEE Electron Device Lett.,* vol. 39, no. 3, pp. 428-431, March 2018.

[49] S. Gong and G. Piazza, "Design and analysis of lithium–niobate-based high electromechanical coupling RF MEMS resonators for wideband filtering," *IEEE Trans. Microw. Theory Tech.,* vol. 61, no. 1, pp. 403–414, Jan. 2013.

[50] S. Gong, and G. Piazza, "Figure-of-merit enhancement for laterally vibrating lithium niobate MEMS resonators," *IEEE Trans. Electron Devices*, vol. 60, no. 11, pp. 3888–3894, 2013.

[51] Y-H. Song, R. Lu, and S. Gong, "Analysis and removal of spurious response in SH0 lithium niobate MEMS resonators," *IEEE Trans. Electron Devices*, vol. 63, no. 5, pp. 2066–2073, 2016.

[52] I.E. Kuznetsova, B. Zaitsev, S. Joshi, and I. Borodina, "Investigation of acoustic waves in thin plates of lithium niobate and lithium tantalate," *IEEE Trans. Ultrason. Ferroelectr. Freq. Control*, vol. 48, no. 1, pp. 322–328, 2001.

[53] R. H. Olsson, K. Hattar, S. Homeijer, M. Wiwi, M. Eichenfield, D. Branch, M. Baker, J. Nguyen, B. Clark, T. Bauer, and T. Friedmann, "A high electromechanical coupling coefficient SH0 Lamb wave lithium niobate micromechanical resonator and a method for fabrication," *Sens. Actuators A, Phys.*, vol. 209, pp. 183–190, 2014.

[54] R. H. Olsson, K. Hattar, M. S. Baker, M. Wiwi, J. Nguyen, C. Padilla, S. J. Homeijer, J. R. Wendt, and T. A. Friedmann, "Lamb wave micromechanical resonators formed in thin film plates of lithium niobate," *Proc. Int. Solid-State Sens., Actuators Microsyst. Workshop*, pp. 281–284, Jun. 2014.

[55] R. Wang, S. A. Bhave and K. Bhattacharjee, "Design and fabrication of S_0 Lamb-wave thin-film lithium niobate micromechanical resonators," *IEEE J. Microelectromech. Syst.*, vol. 24, no. 2, pp. 300–308, April 2015.

[56] Y. Yang, A. Gao, and S. Gong, "5 GHz lithium niobate MEMS resonators with high FoM of 153," *Proc. IEEE Int. Conf. Micro Electro Mech. Syst. (MEMS)*, 2017.

[57] G.W. Fang, G. Pillai, M.-H. Li, C.-Y. Liu, and S.-S. Li, "VHF temperature compensated lithium niobate-on-oxide resonator with Q > 3900 for low phase noise oscillators," *Proc. IEEE Int. Conf. Micro Electro Mech. Syst. (MEMS)*, 2018.

[58] S. Gong, Y.-H. Song, T. Manzaneque, R. Lu, Y. Yang, and A. Kourani, "Lithium niobate MEMS devices and subsystems for radio frequency signal processing," *Proc. 60th IEEE Int. Midwest Symp. Circuits Syst.*, 2017.

[59] A. Kourani, Y. Song, B. Arakawa, R. Lu, J. Guan, A. Gao, and S. Gong, "A 150 MHz voltage-controlled oscillator using lithium niobate RF-MEMS oscillators," *IEEE MTT-S Int. Microw. Symp. Dig.*, Jun. 2017, pp. 1307–1310.

[60] A. Kourani, R. Lu, T. Manzaneque, Y. Yang, A. Gao, and S. Gong, "A 175 MHz 72 μW voltage-controlled oscillator with 1.4% tuning range based on lithium niobate MEMS resonator and 65-nm CMOS," *IEEE MTT-S Int. Microw. Symp. Dig.*, 2018.

[61] M.Rinaldi, C. Zuo, J. Spiegel, and G. Piazza "Reconfigurable CMOS oscillator based on multifrequency AlN contour-mode MEMS resonator," *IEEE Trans. Electron Devices*, vol 58, no. 5, pp. 1281–1286, May 2011.

[62] M. Rinaldi, C. Zuniga, B. Duick and G. Piazza, "Use of a single multiplexed CMOS oscillator as direct frequency read-out for an array of eight AlN contour-mode NEMS resonant sensors," *IEEE Conf. Sensors*, Nov. 2010.

[63] C. Zuo, N. Sinha, J. Spiegel, and G. Piazza, "Multi-frequency pierce oscillators based on piezoelectric AlN contour-mode MEMS resonators," *Proc. IEEE Int. Freq. Control Symp.*, May 2008, pp. 402–407.

[64] J. Stegner *et al*., "A multi-frequency MEMS-based RF oscillator covering the range from 11.7 MHz to 1.9 GHz," *IEEE MTT-S Int. Microw. Symp. Dig.*, 2018, pp. 575-578.

[65] C. Zuo, J. Spiegel, and G. Piazza, "Dual-mode resonator and switchless reconfigurable oscillator based on piezoelectric AlN MEMS technology," *IEEE Trans. Electron Devices*, vol 58, no. 10, pp. 3599- 3603, Oct. 2011.

[66] H. Lavasani, R. Abdolvand and F. Ayazi, "Single-resonator dual-frequency AlN-on-Si MEMS oscillators," *IEEE Trans. Ultrason., Ferroelectr., Freq. Control*, vol 62, no. 5, pp. 802- 813, May 2015.

[67] H. Zhang, W. Pang, H. Yu, and E. S. Kim, "High-tone bulk acoustic resonators on sapphire, crystal quartz, fused silica, and silicon substrates," *Journal of Applied Physics*, vol. 99, no. 12, May 2006.

[68] W. Pang, H. Zhang, J. J. Kim, H. Yu, and E. S. Kim, "High-tone bulk acoustic resonator integrated with surface micromachined FBAR filter on a single chip," in *IEEE MTT-S Int. Microw. Symp. Dig.*, Jun. 2005, pp. 2057–2060.

[69] H. Yu *et al*., "HBAR-Based 3.6 GHz oscillator with low power consumption and low phase noise," in *IEEE Trans. Ultrason., Ferroelectr., and Freq. Control*, vol. 56, no. 2, pp. 400-403, Feb. 2009.

[70] N. Chrétien *et al.*, "Double-port AlN/Sapphire high overtone bulk acoustic resonators for the stabilization of radio-frequency oscillators," in *Proc. IEEE Int. Ultrason. Symp. (IUS)*, Oct. 2012, pp. 2210–2213.

[71] B. P. Sorokin *et al.*, "AlN/single crystalline diamond piezoelectric structure as a high overtone bulk acoustic resonator," *Appl. Phys. Lett.*, vol. 102, no. 11, p. 113507, 2013.

[72] N.-K. Kuo *et al*., "Micromachined sapphire GHz lateral overtone bulk acoustic resonators transduced by aluminum nitride," *Proc. IEEE Int. Conf. Micro Electro Mech. Syst. (MEMS)*, Feb. 2012.

[73] S. Gong, N.-K. Kuo, and G. Piazza, "GHz high-*Q* lateral overmoded bulk acoustic-wave resonators using epitaxial SiC thin film," *IEEE J. Microelectromech. Syst.*, vol. 21, no. 2, pp. 253–255, April 2012.

[74] S. Gong, N.-K. Kuo, and G. Piazza, "GHz AlN lateral overmoded bulk acoustic wave resonators with a $f \cdot Q$ of 1.17×1013," in *Proc. Joint Conf. IEEE Int. Freq. Control Eur. Freq. Time Forum (FCS)*, May 2011, pp. 1–5.

[75] M. Ziaei-Moayyed, S. D. Habermehl, D. W. Branch, P. J. Clews, and R. H. Olsson, "Silicon carbide lateral overtone bulk acoustic resonator with ultrahigh quality factor," in *Proc. IEEE 24th Int. Conf. Micro Electro Mech. Syst. (MEMS)*, Jan. 2011, pp. 788–792.

[76] R. Lu, T. Manzaneque, Y. Yang, A. Kourani, and S. Gong, "Lithium niobate lateral overtone resonators for low power frequency-hopping applications," *Proc. IEEE Int. Conf. Micro Electro Mech. Syst. (MEMS)*, 2018.

[77] R. Lu, T. Manzaneque, Y. Yang, J. Zhou, H. Hassanieh, and S. Gong, "RF filters with periodic passbands for sparse Fourier transform-based spectrum sensing," *J. Microelectromech. Syst.*, vol. 27, no. 5, pp. 931-944, Oct. 2018.

[78] A. Kourani, R. Lu, A. Gao, and S. Gong, "A 300-500 MHz tunable oscillator exploiting ten overtones in single lithium niobate resonator," *IEEE Int. Freq. Control Symp. (IFCS)*, April 2019.

[79] H. Hu, J. Yang, L. Gui, and W. Sohler, "Lithium niobate-on-insulator (LNOI): Status and perspectives," in *SPIE Photonics Europe*, 2012.

[80] M. Levy, R. M. Osgood, R. Liu, L. E. Cross, G. S. Cargill, A. Kumar, and H. Bakhru, "Fabrication of single crystal lithium niobate films by crystal ion slicing," *Appl. Phys. Lett.*, vol. 73, pp. 2293–2295, 1998.

[81] M. Kadota and T. Ogami, "5.4 GHz Lamb wave resonator on $LiNbO_3$ thin crystal plate and its application," *Jpn. J. Appl. Phys.*, vol. 50, 2011.

[82] R. Schneider, T. Naing, T. Rocheleau, and C. Nguyen, "Gap reduction-based frequency tuning for AlN capacitive piezoelectric resonators," *Proc. Joint Conf. Eur. Freq. Time Forum IEEE Int. Freq. Control Symp. (EFTF/IFC)*, April 2015.

[83] B. Kim, R. H. Olsson, and K. E. Wojciechowski, "Ovenized and thermally tunable aluminum nitride microresonators," *Proc. IEEE Ultrason. Symp.*, Oct. 2010.

[84] S. Gong and G. Piazza, "Large frequency tuning of lithium niobate laterally vibrating MEMS resonators via electric boundary reconfiguration," *Proc. Int. Solid-State Sens., Actuators Microsyst. Conf. (TRANSDUCERS)*, Jun. 2013.

[85] D. W. Branch, K. E. Wojciechowski, and R. H. Olsson, III, "Elucidating the origin of spurious modes in aluminum nitride microresonators using a 2-D finite-element model," *IEEE Trans. Ultrason. Ferroelectr. Freq. Control*, vol. 61, no. 5, pp. 729–738, May 2014.

[86] D. W. Branch and R. H. Olsson, "Suppressing fine-frequency modes in aluminum nitride microresonators," *Proc. IEEE Ultrason. Symp.*, Sep. 2014, pp. 572–577.

[87] M. Giovannini, S. Yazici, N.-K. Kuo, and G. Piazza, "Apodization technique for spurious mode suppression in AlN contour-mode resonators," *Sens. Actuators A, Phys.*, vol. 206, no. 1, pp. 42–50, Feb. 2014.

[88] H. Zhang, J. Liang, H. Zhang, D. Zhang, X. Zhou, and W. Pang, "Transverse mode spurious resonance suppression in Lamb wave MEMS resonators: Theory, modeling, and experiment," *IEEE Trans. Electron Devices*, vol. 62, no. 9, pp. 3034–3041, Sep. 2015.

[89] Y. H. Song and S. Gong, "Arraying SH0 lithium niobate laterally vibrating resonators for mitigation of higher order spurious modes," *Proc. IEEE Int. Conf. Micro Electro Mech. Syst. (MEMS)*, Jan. 2016.

[90] Y. H. Song and S. Gong, "Elimination of spurious modes in SH0 lithium niobate laterally vibrating resonators," *IEEE Electron Device Lett.*, vol. 36, no. 11, pp. 1198–1201, Nov. 2015.

[91] Y. H. Song and S. Gong, "Spurious mode suppression in SH0 lithium niobate laterally vibrating MEMS resonators," *Proc. IEEE Int. Electron Devices Meeting (IEDM)*, Dec. 2015.

[92] Y. H. Song and S. Gong, "Wideband RF filters using medium-scale integration of lithium niobate laterally vibrating resonators," *IEEE Electron Device Lett.*, vol. 38, no.3, pp. 387–390, March 2017.

[93] Y. H. Song and S. Gong, "Wideband spurious-free lithium niobate RFMEMS filters," *IEEE J. Microelectromech. Syst.*, vol. 26, no.4, pp. 820–828, Aug. 2017.

[94] R. Lu, T. Manzaneque, Y. Yang, and S. Gong, "Exploiting parallelism in resonators for large voltage gain in low power wake up radio front ends," *Proc. IEEE Int. Conf. Micro Electro Mech. Syst. (MEMS)*, 2018.

[95] T. Manzaneque, R. Lu, Y. Yang, and S. Gong, "A high FoM lithium niobate resonant transformer for passive voltage amplification," *Proc. Int. Solid-State Sens., Actuators Microsyst. Conf. (TRANSDUCERS)*, 2017.

[96] W. M. C. Sansen, *Analog Design Essentials*. New York: Springer Verlag, 2006.

[97] E. A. Vittoz, M. G. R. Degrauwe, and S. Bitz, "High performance crystal oscillator circuit: Theory and application," *IEEE J. Solid-State Circuits*, vol. 23, no. 3, pp. 774-783, June 1988.

[98] A. P. S. Khanna, E. Gane, and T. Chong, "A 2 GHz voltage tunable FBAR oscillator," *IEEE MTT-S Int. Microw. Symp. Dig.*, 2003.

[99] H. Ito, H. Lakdawala, A. Ravi, S. Pellerano, R. Ruby, K. Soumyanath, and K. Masu, "A 1.7-GHz 1.5-mW digitally-controlled FBAR oscillator with 0.03-ppb resolution," *IEEE European Solid-State Circuits Conf.*, 2008.

[100] Y. Yang, R. Lu, T. Manzaneque, and S. Gong, "1.7 GHz Y-cut lithium niobate MEMS resonators with FoM of 336 and $f.Q$ of 9.15×10^{12}," in *IEEE MTT-S Int. Microw. Symp. Dig.*, Jun. 2018, pp. 563.566.

[101] Y. Wang, Y. Hong, W. Goh, K. T. C. Chai, and M. Je, "A resonator-adaptable oscillator using varactor-loaded tuned amplifiers," *IEEE Microwave and Wireless Components Letters*, vol. 27, no. 8, pp. 724-726, Aug 2017.

[102] F. Padovan, F. Quadrelli, M. Bassi, M. Tiebout, and A. Bevilacqua, "A quad-core 15GHz BiCMOS VCO with -124 dBc/Hz phase noise at 1MHz offset, -189dBc/Hz FoM, and robust to multimode concurrent oscillations," *IEEE Int.Solid-State Circuits Conf.*, 2018, pp. 376-377.

[103] A. Khanna, E. Topacio, E. Gane, and D. Elad, “Low jitter silicon bipolar based VCOs for applications in high speed optical communication systems,” *IEEE Int.Microw. Symp*, 2001, pp. 1567- 1570.

[104] Y. Lee, J. Lee, and S. Nam, “High-Q active resonators using amplifiers and their applications to low phase-noise free-running and voltage-controlled oscillators,” *IEEE Trans. Microw. Theory and Techn*., vol. 52, no. 11, pp. 2621- 2626, 2004.

[105] P. Rice, R Sloan, M. Moore, A. Barnes, M. Uren, N. Malbert, and N. Labat, “A 10 GHz dielectric resonator oscillator using GaN technology,” *IEEE Int. Microw. Symp*, 2004, pp. 1497- 1500.

[106] M. Hara et al., “Super-high-frequency band filters configured with air-gap-type thin,” *Jpn. J. Appl. Phys*, vol. 49, no. 7, pp. 07HD13.1-07HD13.4, 2010.

[107] G. Chen, and M. Rinaldi, “High-Q X band aluminum nitride combined overtone resonators,” *Joint Conference of the IEEE Int. Freq. Control Symp. and European Freq. and Time Forum (EFTF/IFC)*, 2019, pp. 1-3.

[108] M. Rinaldi, C. Zuniga, and G. Piazza, “5-10 GHz AlN contour-mode nanoelectromechanical resonators,” *IEEE Int. Conf. MEMS*, 2009, pp. 916-919.

[109] M. Park, Z. Hao, D. Kim, A. Clark, R. Dargis, and A. Ansari, “A 10 GHz single-crystalline scandium-doped aluminum nitride Lamb-wave resonator,” *Int. Conf. Solid-State Sensors, Actuators and Microsys. & Eurosensors XXXIII*, 2019, pp. 450- 453.

[110] M. Park, J. Wang, R. Dargis, A. Clark and A. Ansari, “Super high-frequency scandium aluminum nitride crystalline film bulk acoustic resonators,” *IEEE Int. Ultrasonics Symp. (IUS)*, 2019, pp. 1689-1692.

[111] M. Ghatge, G. Walters, T. Nishida, and R. Tabrizian, “High-Q UHF and SHF bulk acoustic wave resonators with ten-nanometer $HF_{0.5}ZR_{0.5}O_2$ ferroelectric transducer,” *Int. Conf. Solid-State Sensors, Actuators and Microsys. & Eurosensors XXXIII*, 2019, pp. 450- 453.

[112] D. Weinstein, S. A. Bhave, “Acoustic resonance in an independent-gate finFET,” *Solid-State Sensors, Actuators and Microsystems Workshop*, pp. 459- 462, 2010.

[113] Y. Yang, R. Lu, T. Manzaneque, and S. Gong, “Towards Ka band acoustic: Lithium niobate asymmetrical mode piezoelectric MEMS resonators,” *IEEE Int. Freq. Cont. Symp*., May 2018, pp.1-5.

[114] Y. Yang, R. Lu, and S. Gong, “Scaling acoustic filters towards 5G,” *2018 IEEE International Electron Devices Meeting (IEDM)*, San Francisco, CA, 2018, pp. 39.6.1-39.6.4.

[115] V. Plessky et al., “Laterally excited bulk wave resonators (XBARs) based on thin lithium niobate platelet for 5 GHz and 13 GHz filters,” *IEEE MTT-S Int. Microw. Symp. (IMS)*, 2019, pp. 512.515.

[116] A. Kourani, Y. Yang, and S. Gong, "An X-Band oscillator utilizing overtone lithium niobate MEMS resonator and 65-nm CMOS," *2020 Joint Conf. IEEE Int. Freq. Control Symp. and Int. Symp. App. of Ferr. (IFCS-ISAF)*, 2020, pp. 1-3.

[117] M. Aissi, E. Tournier, M. Dubois, G. Parat, and R. Plana, "A 5.4 GHz 0.35µm BiCMOS FBAR resonator oscillator in above-IC technology," *IEEE Int. Solid-State Circuits Conf.*, 2006, pp. 1228-1235.

[118] H. Zhang, J. Kim, W. Pang, H. Yu, and E. Kim, "5 GHz low-phase-noise oscillator based on FBAR with low TCF," *Int. Conf. Solid-State Sensors, Actuators and Microsystems*, 2005, pp. 1100- 1101.

[119] M. ElBarkouky, G. Vandersteen, P. Wambacq, and Y. Rolain, "A 7 GHz FBAR overtone–based oscillator," *Euro. Microw. Conf.*, 2009, pp. 318- 321.

[120] E. Tournier, "5.4GHz, 0.35µm BiCMOS FBAR-based single-ended and balanced oscillators in above-IC technology," *MEMS-based Circuits and Systems for Wireless Communication, Springer*, pp. 155-186, 2013.

[121] J. Tsai, C. Hsu and C. Chao, "An X-band 9.75/10.6 GHz low-power phase-locked loop using 0.18-µm CMOS technology," *European Microwave Integrated Circuits Conf. (EuMIC)*, Paris, 2015, pp. 238-241.

[122] H. Yeo, S. Ryu, Y. Lee, S. Son and J. Kim, "A 940 MHz-bandwidth 28.8 µs-period 8.9 GHz chirp frequency synthesizer PLL in 65 nm CMOS for X-band FMCW radar applications," *IEEE Int. Solid-State Circuits Conf. (ISSCC)*, San Francisco, CA, 2016, pp. 238-239.

[123] A. Elkholy, M. Talegaonkar, T. Anand and P. K. Hanumolu, "A 6.75-to-8.25 GHz 2.25 mW 190 fsrms integrated-jitter PVT-insensitive injection-locked clock multiplier using all-digital continuous frequency-tracking loop in 65 nm CMOS," *IEEE Int. Solid-State Circuits Conf. (ISSCC)*, San Francisco, CA, 2015, pp. 1-3.

[124] A. Elkholy, A. Elmallah, M. Elzeftawi, K. Chang and P. K. Hanumolu, "A 6.75-to-8.25 GHz, 250 fsrms-integrated-jitter 3.25 mW rapid on/off PVT-insensitive fractional-N injection-locked clock multiplier in 65 nm CMOS," *IEEE International Solid-State Circuits Conference (ISSCC)*, San Francisco, CA, 2016, pp. 192-193.

[125] R. Wang and F. F. Dai, "A 0.8~1.3 GHz multi-phase injection-locked PLL using capacitive coupled multi-ring oscillator with reference spur suppression," *IEEE Custom Integrated Circuits Conf. (CICC)*, Austin, TX, 2017, pp. 1-4.

[126] S. Choi, S. Yoo, Y. Lim and J. Choi, "A PVT-robust and low-jitter ring-VCO-based injection-locked clock multiplier with a continuous frequency-tracking loop using a replica-delay cell and a dual-edge phase detector," *IEEE Journal of Solid-State Circuits*, vol. 51, no. 8, pp. 1878-1889, Aug. 2016.

[127] Y. Yang, R. Lu, L. Gao, and S. Gong, “10-60-GHz electromechanical resonators using thin-film lithium niobate,” *IEEE Trans. Microw. Theory Tech*., pp. 1–1, Oct. 2020.

[128] B. Razavi, *RF Microelectronics.* Prentice Hall, 2012.

[129] S. Rai, Y. Su, W. Pang, R. Ruby and B. Otis, “A digitally compensated 1.5 GHz CMOS/FBAR frequency reference,” in *IEEE Trans. Ultrason., Ferroelectr., and Freq. Control*, vol. 57, no. 3, pp. 552-561, March 2010.

[130] J. Shi and B. P. Otis, “A sub-100µW 2GHz differential Colpitts CMOS/FBAR VCO,” *IEEE Custom Integrated Circuits Conf.(CICC),* San Jose, CA, 2011, pp. 1-4.

[131] H. M. Lavasani, W. Pan, B. Harrington, R. Abdolvand and F. Ayazi, “A 76dBΩ 1.7GHz 0.18µm CMOS tunable transimpedance amplifier using broadband current pre-amplifier for high frequency lateral micromechanical oscillators,” *IEEE Int. Solid-State Circuits Conf. (ISSCC),* San Francisco, CA, 2010, pp. 318-319.

[132] B. W. Bahr, L. C. Popa and D. Weinstein, “1GHz GaN-MMIC monolithically integrated MEMS-based oscillators,” *IEEE Int. Solid-State Circuits Conf. - (ISSCC)*, San Francisco, CA, 2015, pp. 1-3.

[133] C. Zuo, J. V. Der Spiegel and G. Piazza, “1.05-GHz CMOS oscillator based on lateral-field-excited piezoelectric AlN contour- mode MEMS resonators,” in *IEEE Trans. Ultraso., Ferroelectr., and Freq. Control*, vol. 57, no. 1, pp. 82-87, Jan. 2010.

[134] J. Koo, A. Tazzoli, J. Segovai-Fernandez, G. Piazza and B. Otis, “A −173 dBc/Hz @ 1 MHz offset Colpitts oscillator using AlN contour-mode MEMS resonator,” *IEEE Custom Integrated Circuits Conf.*, San Jose, CA, 2013, pp. 1-4.

[135] F. Vanhelmont, P. Philippe, A. B. M. Jansman, R. F. Milsom, J. J. M. Ruigrok and A. Oruk, “A 2 GHz Reference Oscillator incorporating a Temperature Compensated BAW Resonator,” *IEEE Ultrason. Symp.*, Vancouver, BC, 2006, pp. 333-336.